Experimental Investigation of Quasistatic and Dynamic Fracture Properties of Titanium Alloys

Thesis by
David Deloyd Anderson

In Partial Fulfillment of the Requirements
for the Degree of
Doctor of Philosophy

California Institute of Technology
Pasadena, California

2002

(Submitted January 11, 2002)

Acknowledgments:

I would like to thank my advisors, Dr. Rosakis and Dr. Ravichandran, for their help, support, ideas, and patience with my research and with my doings in general. Life is too complicated to allow exclusive focus on any one thing, even research, and they helped me in managing all.

In addition to Drs. Rosakis and Ravichandran, I would first like to thank those on my thesis committee: Dr. Bhattacharya, Dr. Üstündag, and Dr. Meyers (U.C.S.D.) for their time, comments, and suggestion. These are the people who reviewed my research, listened to my presentation, verbally poked and prodded me, and then with their handshakes and signatures made me a doctor.

My research was funded by the Office of Naval Research by Dr. G. Yoder, Scientific Officer. Little research and training occurs without funding, so for their support I am grateful. I was also assisted by the Charles Lee Powell Foundation and the ARCS (Achievement Rewards for College Scientists—www.arcsfoundation.org) foundation. The latter group not only made it financially palatable to forsake the workforce for a higher education (while "supporting" a family), but they provided many opportunities for me to interact with their members and donors. This provided me with endless motivation to make good on their show of faith in me. I would like to name in particular Betty Whiting, who practically adopted me and my family while we were so far from our kin. She is so thoughtful and generous in so many ways. It has been a thrill to get to know her and this group.

I am indebted to the members of the Rosakis research group: Group research warlord Dr. David Owen, research staff Petros Arakelian and Denise Thobe, and post-docs and fellow students: Dr. Ben Chow, Dr. Demir Coker, Dr. Pradeep Guduru, Georgios Lykotrafitis, Dr. Mikio Oda, Dr. Carl-Ernst Rousseau, Dr. Omprakash Samudrala, Dr. Damir Semenski, Dr. S. Suzuki, Kaiwen Xia, and Dr. Luoyu (Roy) Xu. I dare not attempt a list of friends and associates outside my group, but their contributions are significant and appreciated also. My co-workers are the people who helped determine my quality of life for 40-80 hours a week. They not only provided a knowledge base for research, but also friendship, entertainment, and recreation. They figure prominently into my life's story during my tenure at Caltech.

I must mention my fellow aero student biking friends: Dr. Eric Burcsu, Dr. Piet Moeleker, and Dr. Adam Rasheed. We did a lot of miles together.

Caltech is such a unique environment in which to work and do research. It is a small school so all interactions within the community feel personal. There is also so much talent here and a high level of expectation. I am impressed with Caltech's history and approach to education and science. There hasn't been a time when I walk on campus that I am not amazed that they allowed me to study and work here, so to receive a doctorate from this institution is for the most part unbelievable.

Jon Epstein and Walt Reuter provided me with the stepping stone to get into Caltech. They took me on as an intern at the Idaho National Engineering (and now Environmental) Laboratory when I was a lowly sophomore at Utah State University, put me under their wings, and let me learn how to be an experimentalist. That was my big break.

I am indebted to my parents, who somehow instilled in me the work ethic and other traits that were necessary to get me to this point. They are as supportive as parents can be. My family and my wife's family also provided excellent ground control for such a mission as this.

Finally I'd like to thank my wife Jennelle who has been the most patient and supportive of all. She sacrificed more in the first year than a wife should have to sacrifice in a lifetime. I hope it will prove worthwhile. We have two wonderful kids who also deserve (if not demand) attention: Whitney Jaye and Damian McKay. May my education in fracture mechanics help me fix all the stuff they break.

Abstract

The goal of this work is to investigate the quasistatic and dynamic fracture properties of three titanium alloys: 6Al-4V titanium, 6Al-4V titanium ELI, and Timetal 5111. While standard tests exist for measuring quasistatic fracture toughness, the dynamic investigation requires that several measurement techniques are employed including Coherent Gradient Sensing (CGS), Crack Opening Displacement (COD), and the use of strain gages. The use of these methods with difficult engineering materials in the dynamic loading regime requires methodologies to be advanced beyond that previously required with model materials having properties ideal for experimental measurements techniques.

After a description of each measurement technique is given, stress intensity factor measurements made on 12.7 mm thick pre-cracked 6Al-4V titanium specimens are compared. These specimens were dynamically impacted in three point bend in a drop weight tower. Specimens with and without side-grooves were tested as each measurement technique allows. Side-grooves are useful to increase the degree of plane strain experienced in proximity of the crack tip, allowing plane strain (geometry independent) fracture toughnesses to be obtained from specimens that may be otherwise too thin in cross section. Resulting stress intensity factor-time histories from the different techniques are compared to verify that their results mutually agree.

Advancements in employing CGS, a shearing interferometric technique, are described in more detail. First, the analysis of CGS interferograms is extended to allow experimental fringe data to be fit to very general analytical asymptotic crack tip solution to determine mixed mode stress intensity factors. As formulated in this work, the CGS technique can be used to measure stress intensity factors for non-uniformly propagating dynamic mixed mode cracks moving along arbitrary paths in homogeneous linear elastic isotropic materials. Other advancements are also detailed which improve analysis accuracy, objectivity, and efficiency.

Finally, with the equivalence of the three measurement technique results established, tests were performed on 8–17 mm thick pre-cracked three point bend specimens of the three materials to measure critical stress intensity values for crack initiation. Side-grooves are necessary for the more ductile 6Al-4V titanium ELI and Timetal 5111 materials to obtain plane strain fracture toughness values. It is found that both the 6Al-4V titanium ELI and Timetal 5111 alloys are 50-70% tougher than the 6Al-4V titanium, and for all three materials their initiation toughness does not vary significantly with loading rate over the domain tested.

Contents

List of Figures

List of Tables

Chapter 1

Fracture Mechanics Preliminaries

1.1 Fracture Mechanics

Fracture mechanics is a subset of solid mechanics that deals with the behavior of solid systems containing one or more cracks. Fracture mechanics is a relatively new area of solid mechanics research, with its foundation laid in the early 20th century. Already it has broad application in systems ranging in size from micrometer length scales (thin films, MEMS) up to kilometer length scales (Earthquake fault lines). Some fracture mechanics problems may relate to configuration effects, such as cracks affected by weak bond lines, material anisotropy, or specimen inhomogeneity. These experiments may be performed with “model” materials having properties idealized for the experiment. However, one important job for fracture mechanics is to evaluate the performance of imperfect materials for engineering use. In this case the experimental models and methods must be extended and tailored to suit the material, and not the other way around.

In studying materials containing cracks, a whole hierarchy of models, tools, and techniques exist with differing complexity and generality. The simplest model with sufficient descriptive/predictive power is obviously the best model to use. For engineering materials, model choice must be made carefully and justified.

A brief description of two relevant crack tip models and failure criteria follows. As these concepts are elemental to fracture mechanics, a more complete description can be obtained from any good text on the subject, such as Anderson [5].

1.2 Linear Elastic Fracture Mechanics

When possible, fields about a single crack tip are analyzed using linear elastic fracture mechanics (LEFM) as this is the simplest model. Within LEFM any arbitrary crack tip stress state in a linear elastic isotropic homogeneous material can be decomposed into a unique linear combination of three mutually orthogonal modes: symmetric in-plane (mode I), antisymmetric in-plane (mode II), and out-of-plane (mode III). Modes I and II are schematically depicted in Figure 1.1.

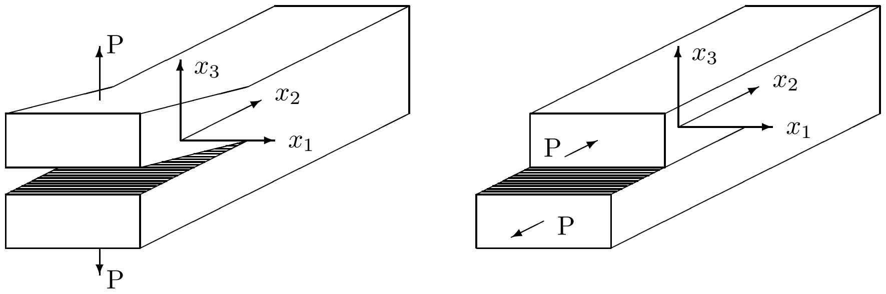

Figure 1.1: Schematic of both in-plane crack modes: mode I (left) and mode II (right).

For each mode, stress-fields satisfying the boundary condition of having stress-free crack faces are asymptotic with unknown coefficients reflecting unspecified far-field boundary conditions (Westergaard [50], Irwin [21], Sneddon [45], and Williams [51]) are of the form:

$$\sigma_{ij} = \left(\frac{K}{\sqrt{2\pi r}}\right) f_{ij}\left(\theta\right) + \sum_{m=0}^{\infty} A_m r^{\frac{m}{2}} g_{ij}^{(m)}(\theta) \tag{1.1}$$

where σ_{ij} is the stress tensor, r and θ coordinates with respect to the usual crack tip coordinate system (Figure 2.3), f_{ij} and $g_{ij}^{(m)}$ are functions of θ, and K and A_m are the coefficients of the singular and higher order terms respectively. f_{ij} is a universal function and holds for all cracks propagating at speeds much slower than the material's shear wave speed, including stationary cracks.

For each mode the leading asymptotic term is singular and thus dominates near the crack tip. Because of this dominance, the leading term's coefficient (or magnitude) can serve as a single parameter description of the stress state at the crack tip. The coefficient K for the leading singular term is called the stress intensity factor, which is usually subscripted to specify mode, i. e., K_I, K_{II} or K_{III}.

1.3 Quasistatic and Dynamic Stress Intensity Factors

Quasistatic crack conditions are obtained when loading is sufficiently slow that stresses throughout the body are in equilibrium and the crack tip is stationary or at most moving very slowly. In dynamics, loading is characterized by stress waves, or the crack tip is moving fast enough to invoke inertial/rate effects in the vicinity of the crack tip, or both. Early examples of dynamic fracture work includes Yoffe [54], Broberg [7], Atkinson and Eshelby [6], Achenbach, [1] [2] [3], Kostrov and Nikitin [27], Freund [13] [14] [15], and Willis [52]. A single excellent source regarding dynamic fracture is Freund [16].

Equation 1.1 holds for all cracks in homogeneous linear elastic isotropic materials regardless of loading rate and crack speed so long as the crack speed is less than the material's Rayleigh wave speed (Freund and Clifton [18]). In particular, the singular term is the same for all such cases, though for higher order terms the angular dependence $g_{ij}^{(m)}(\theta)$ depends on crack conditions. In chapter 3, $g_{ij}^{(1)}(\theta)$ for a non-uniformly propagating dynamic mixed mode crack moving along an arbitrary path is given in the context of CGS measurement technique analysis. For less general crack condition, $g_{ij}^{(1)}(\theta)$ simplifies. Quasistatic stress fields are the limiting case of dynamic fields as rates go to zero.

For dynamic cracks, the stress intensity factor is superscripted with a "d". For a stationary crack, K^d has dependence:

$$K^d = K^d\left(P(t), a(t), t\right) \tag{1.2}$$

where $P(t)$ is generalized load, $a(t)$ is crack length, and t is time. For a moving crack the stress intensity factor also depends on crack tip speed and for mode I can be related to that of a stationary crack by (Freund, [14] [16])

$$K_I^d\left(P(t), a(t), \dot{a}(t)\right) = k(\dot{a}) K_I^d\left(P(t), a(t), 0\right) \tag{1.3}$$

where $k(\dot{a})$ is a universal function of crack tip speed which decreases from 1 to 0 as the crack tip speed increases from 0 to the Rayleigh wave speed.

1.4 Small Scale Yielding

A stress singularity at the crack tip as predicted by LEFM cannot exist in materials with finite strength. Instead the highly stressed material yields and plastically deforms. To first order the size of the plastic zone for mode I is:

$$r_p = \frac{1}{2\,\pi}\left(\frac{K_I^d}{\sigma_{YS}}\right)^2 \tag{1.4}$$

where σ_{YS} is the material yield stress. The actual shape of the plastic zone depends on crack tip triaxiality. Because σ_{YS} is strain-rate dependent, r_p is dependent on crack tip loading rate and propagation speed, with the later effect dominant for growing cracks. Equation 1.4 defines a useful material-dependent length scale for crack tip mechanics.

In materials that are well modeled by LEFM, the plastic zone is small enough to be completely surrounded by an annulus in which stresses are described by the K-field (leading term in the asymptotic expansion). The outer limit of the K-field dominated annulus is due to the increasing relative contributions of higher order asymptotic stress field terms. However since a K-dominated annulus completely bounds the crack tip, K is still a single parameter description of the crack tip stress state in that it describes the entire boundary conditions of the crack tip. This concept that LEFM can still describe crack tip fields in such materials despite crack tip yielding is called small scale yielding (S.S.Y.) (Freund [16], Freund and Rosakis [17]).

1.5 Failure Criterion

With K taken to be a single parameter description of the stress state at the crack tip, it can also be used to describe material fracture properties. By mechanically testing a material, critical values of K can be measured which correspond to that material's state of incipient failure.

Fracture toughness depends on material thickness up to a point, or more specifically on the ratio h/r_p where h is thickness (Irwin [23], Kanninen and Popelar [26]). This is because the failure of an infinitesimal length of crack to first order depends on the degree of local triaxiality, which is a function of its location with respect to free surfaces. Integrating this effect over the entire width of the crack, a thick specimen will have a different overall toughness per unit width than a thin one. As thickness increases, material toughness asymptotically approaches a constant value as free surface effects become negligible.

The effect of thickness on quasistatic mode I initiation toughness K_{Ic} is well understood. Irwin [22] empirically obtained a relationship between fracture toughness and thickness for 7075-T6 and 2024-T4 aluminum:

$$\frac{K_{Ic}}{K_{IC}} = \left[1 + 5.6\,\pi^2\left(\frac{r_p}{h}\right)^2\right]^{1/2} \tag{1.5}$$

where K_{IC} is the asymptotic limit of toughness as thickness increases, r_p is the characteristic plastic zone size (equation 1.4), and h is specimen thickness. This relationship is plotted in Figure 1.2. The horizontal dashed line is the asymptotic limit of toughness as thickness increases (K_{IC}). The circle with adjacent text indicate the error in assuming $K_{Ic} = K_{IC}$ for various values of h/r_p. While other materials exhibit the same qualitative behavior, quantitative results vary and must be obtained experimentally (Jones and Brown [24]).

Regarding thickness effects, little research has been performed with respect to dynamic loading. The increased complexity of the dynamic case is due to the dependence of material properties (and thus r_p) on local strain rate. However an asymptotic limit is still expected with increased thickness as boundary effects become increasingly negligible.

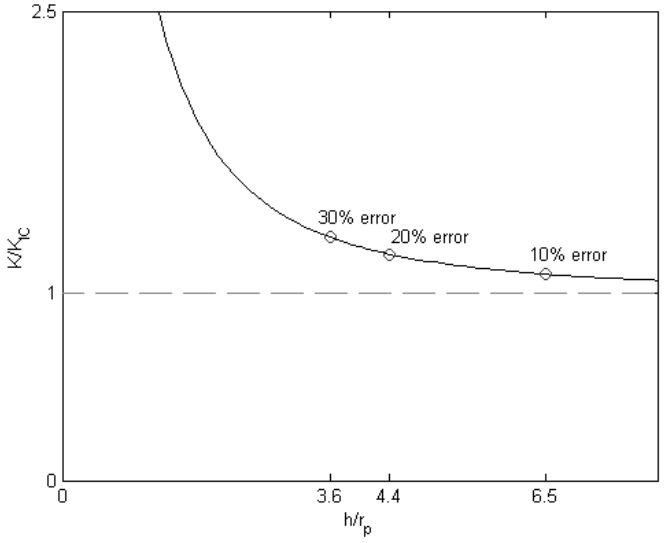

Figure 1.2: Normalized initiation toughness versus specimen thickness for aluminum.

To make material fracture properties independent of geometry, the asymptotic value of toughness, or “plane strain” toughness is used. In addition to being geometry independent, plane strain fracture toughnesses are also conservative compared to toughness for thinner geometries and thus more safe to use.

Ideally plane strain values are obtained by testing thick specimens compared to plastic zone size. Plane strain values can be obtained from thinner specimens by modifying geometry to create plane strain conditions, typically by machining side-grooves. Side-grooves are “V” shaped notches cut in the sides of a specimen centered on the crack and extending the length of the specimen (Figure 1.3). Side-grooves increase the triaxiality at the crack tip by reducing the amount of Poisson contraction about the tip, subjecting the crack tip to more uniformly plane strain like conditions as if the specimen were thicker.

As with other material properties such as ultimate strength, fracture toughness properties are generally dependant on strain rate (Freund [16], Freund, Duffy and Rosakis [19]) and temperature. For a dynamically loaded stationary crack, since K^d describes the magnitude of the singular stress

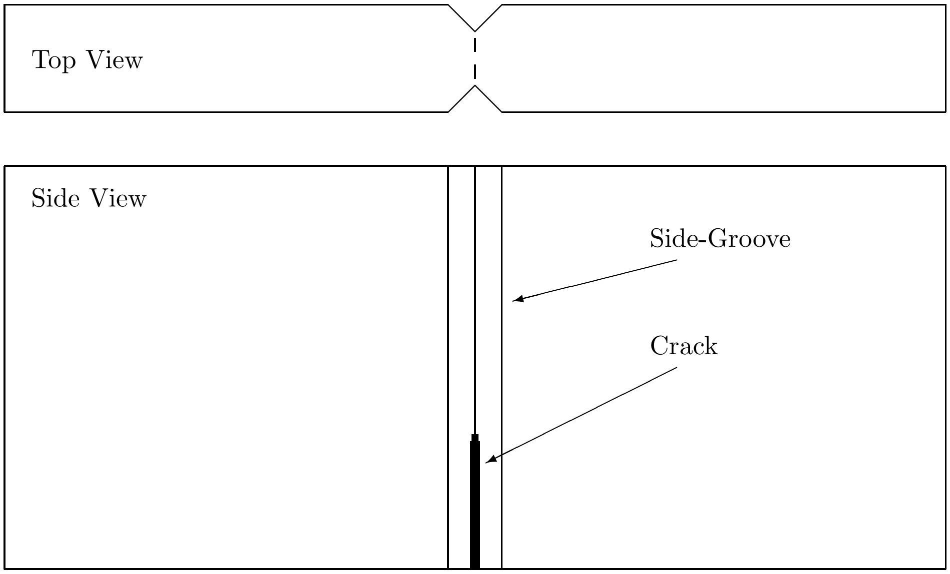

Figure 1.3: Schematic of side-grooves.

field, the time rate of change of K^d describes stress rates and thus strain rates also. Assuming K-dominance and a thick specimen, crack initiation occurs in mode I for example when

$$K_I^d(P(t), a_0) = K_{IC}(\dot{K}_I^d(t)) \text{ at } t = t^\star \tag{1.6}$$

where a_0 is crack length and $t^\star$ is the time of initiation. The left-hand side is the stress intensity applied to the crack tip and depends on geometry and load history. It can be determined analytically or computationally as appropriate. Analytical examples may be found in Freund [16]. The stress intensity factor on the right-hand side is a material property and can only be determined experimentally (Dally and Barker [10]).

For growing cracks, the near tip strain rates are dominated by the rate at which material points move relative to the crack tip singular field, thus the failure criterion for a moving mode I crack is dependent on crack velocity (Freund and Clifton [18]):

$$K_I^d(P(t), a(t), \dot{a}(t)) = K_{ID}(\dot{a}(t)) \text{ for } t > t^\star \tag{1.7}$$

where $\dot{a}$ is the crack tip speed. Again the left-hand side is the applied stress intensity factor. The right-hand side is a property of the material.

The quasistatic failure criterion is the limiting case of the dynamic criteria as rates go to zero.

In the same way material ultimate strengths are usually in terms of normal stresses and not shears, material fracture properties are usually limited to mode I. This is the most commonly observed crack configuration because growing cracks in homogeneous monolithic materials turn during advancement to be locally mode I. However, mixed mode (mode I and mode II) two-parameter characterization may be of interest, for example in cases where loading is not symmetric or for cracks following weak bond lines. In material data sheets if fracture data is reported, it is often only the mode I quasistatic plane strain fracture toughness K_{IC}. This may be appropriate *only* if K_{IC} is a conservative value for design purposes.

1.6 Elastic–Plastic Fracture Mechanics

For more ductile materials the assumption of small scale yielding may not be met, disallowing LEFM analysis. The next level of fracture modeling is elastic-plastic fracture mechanics (EPFM). In EPFM the J integral is given by

$$J = \int_\Gamma \left(w\, dy - T_i \frac{\partial u_i}{\partial x} ds \right) \tag{1.8}$$

and is a measure of energy release rate with respect to crack growth. In the above equation w is strain energy density, T_i are components of the traction vector, and u_i are displacement vector components. The integral is over an arbitrary path Γ counter-clockwise around the crack tip.

Hutchinson [20], and Rice and Rosengren [38] showed that for materials with constitutive behavior approximated by the Ramberg-Osgood equation the near tip stress and strain fields are given by

$$\sigma_{ij} = k_1 \left(\frac{J}{r} \right)^{\frac{1}{n+1}} \tag{1.9}$$

$$\varepsilon_{ij} = k_2 \left(\frac{J}{r} \right)^{\frac{1}{n+1}} \tag{1.10}$$

where k_1 and k_2 are proportionality constants. With these constants found by applying boundary conditions the above are called the HRR singularity. The uniaxial Ramberg-Osgood equation is given by

$$\frac{\varepsilon}{\varepsilon_0} = \frac{\sigma}{\sigma_0} + \alpha \left(\frac{\sigma}{\sigma_0} \right)^n \tag{1.11}$$

where σ_0 and ε_0 are reference stress and strain respectively and n is the strain hardening exponent of the material.

As described later in section 2.3 the HRR singularity can be related to the crack opening profile, which can be experimentally measured to determine J. J can be used as a failure criterion in the same manner as K. Furthermore, while it may seem improper to compare a LEFM crack tip singularity coefficient with the value of a path independent EPFM contour integral, both are related to energy release rates per unit crack growth. For a linear elastic material $J = K_I^2/E$. Studies utilizing EPFM to determine fracture toughness include Costin and Duffy [8], Nakamura *et al* [32], and Owen [33].

1.7 Research Goal

With ductile/advanced materials being used in increasingly demanding applications, a more thorough understanding of their fracture behaviors is essential. Fracture property data may be needed for a range of crack tip conditions including mixed mode and transient loadings. For some materials (such as aluminum) the critical dynamic stress intensity factor K_{IC}^d for some loading rates can be *less* than the quasistatic stress intensity factor K_{IC} generally used to specify a materials fracture toughness. Consequently, for reliable use a material's fracture behavior over the entire envelope of anticipated service conditions should be understood. The accomplishment of this goal for a wide range of engineering materials requires the development of multiple fracture toughness measurement tools, especially those with dynamic measurement capabilities.

Previous work on material dynamic fracture properties is very limited. Most dynamic failure studies have utilized materials with ideal properties, typically polymers. For example, dynamically loaded Homalite-100 fracture properties were studied using the optical method of caustics by Ravi-Chandar and Knauss [37]. Dynamic crack initiation in PMMA was studied by Rittel and Maigre [30], [40], [39] using a novel hybrid analytical/experimental procedure. Transient crack growth in PMMA was examined using CGS by Freund and Rosakis [17]. Ceramic material was tested by Suresh *et al* [46]. Prior work on engineering materials is limited to simple observations. For example, critical crack opening displacements for explosively loaded 1020 hot-rolled steel were obtained by Wilson, Hawley and Duffy [53]. Dynamic crack growth research of polymers using dynamic photoelasticity is described by Dally [9]. Two of the first studies of dynamic crack growth on metals where conducted by Rosakis, Duffy and Freund [42] and Zehnder and Rosakis [55] who examined highly dynamic crack growth in thick plates of AISI 4340 steel using the optical method of caustics in reflection in conjunction with high speed photography. Recently, dynamic initiation and propagation behavior in thin aluminum sheets was studied by Owen *et al* [33]. Small specimens were loaded using a split Hopkinson bar and the stress intensity factor K_I^d was calculated using boundary measurements by assuming quasi-equilibrium. This assumption was validated by dynamic COD measurements from the thinnest sheets.

This work describes the first time that multiple techniques are extended to measure dynamic crack initiation toughnesses of engineering materials. The CGS technique in particular is further developed to be able to obtain dynamic stress intensity factors, higher order asymptotic term coefficients, and other crack information for very general crack conditions in engineering materials. These capabilities far exceed those of other optical methods such as caustics. Furthermore, dynamic fracture experiments using all measurement techniques are conducted on the same material and configurations to allow measurement cross-checking and ultimately to validate each technique's suitability. Finally the three methods are used to successfully measure dynamic crack initiation toughnesses for three titanium alloys over a range of loading rates.

Chapter 2

Four Fracture Toughness Measurement Techniques

2.1 Overview

A variety of techniques can be used for determining stress intensity factors and fracture toughness. In this chapter, four methods are discussed: boundary load measurement, crack opening displacement (COD), strain gage measurements, and Coherent Gradient Sensing (CGS). Of special interest is the dynamic measurement capabilities of the last three techniques. The goal is to expand capability and establish the suitability of these three techniques for measuring dynamic fracture toughnesses of engineering materials as opposed to model materials with properties ideal for experimental measurement. The advantages and limitations of each technique are described. Methodology for employing these three measurement techniques on more difficult materials is proposed. Finally measurement results from experiments utilizing the three dynamic techniques are compared.

Dynamic stress intensity factor measurements made using these techniques have been performed on a triplex annealed commercial grade 6Al-4V titanium alloy. The specimens were fatigue pre-cracked and then loaded dynamically in three point bend in a drop weight tower. Specimens with and without side-grooves were tested as each method allows. Side-grooves are necessary to obtain plane strain fracture toughness values from specimens that are otherwise insufficiently thick. The results obtained from the various techniques compare favorably.

A table comparing the features of the three techniques capable of dynamic measurement is provided in Appendix A.

2.2 Boundary Load Measurement Calculation

Boundary load measurement can be used to calculate the stress intensity factor. This method only works for quasistatic loading in which the stresses throughout the specimen are in equilibrium. In dynamic situations wave loading dominates and no simple relationship between applied load and stress intensity factor at the crack tip exists.

The relationship between applied load and stress intensity factor can be found analytically for simple geometries and computationally otherwise. ASTM [4] standards exist which prescribe specimen geometry, provide the relationship between load and the mode I stress intensity factor, and list criteria to be met for a test result to be considered standard. The applicable ASTM standards are *E399-90(1997) Standard Test Method for Plane Strain Fracture Toughness of Metallic Materials*, and *E647-00 Standard Test Method for Measurement of Fatigue Crack Growth Rates.* The former standard dictates specimen geometries and conditions for measurement validity for fracture toughness tests, while the latter concerns fatiguing pre-cracks with the same geometries. Specimen fatiguing is used to produce a sharp crack from a blunt machined notch. Standard *E647* also addresses side-grooves by standardizing their geometry and indicating that the effective specimen thickness to use in the stress intensity calculations is

$$B_{eff} = \sqrt{B\,B_N} \tag{2.1}$$

where B is the specimen bulk thickness and B_N is the specimen net thickness at the side-grooves.

Two specimen geometries prescribed by the ASTM standards are most commonly used. The first is the three point bend geometry in which the stress intensity factor K_I is given by

$$K_I = \frac{P}{B\sqrt{W}} \frac{3\frac{S}{W}\sqrt{\frac{a}{W}}}{2\left(1+2\frac{a}{W}\right)\left(1-\frac{a}{W}\right)^{3/2}} \left[1.99 - \frac{a}{W}\left(1-\frac{a}{W}\right)\left\{2.15 - 3.93\frac{a}{W} + 2.7\left(\frac{a}{W}\right)^2\right\}\right] \quad (2.2)$$

where P is the applied load and all other variables are from specimen geometry as shown in Figure 2.1.

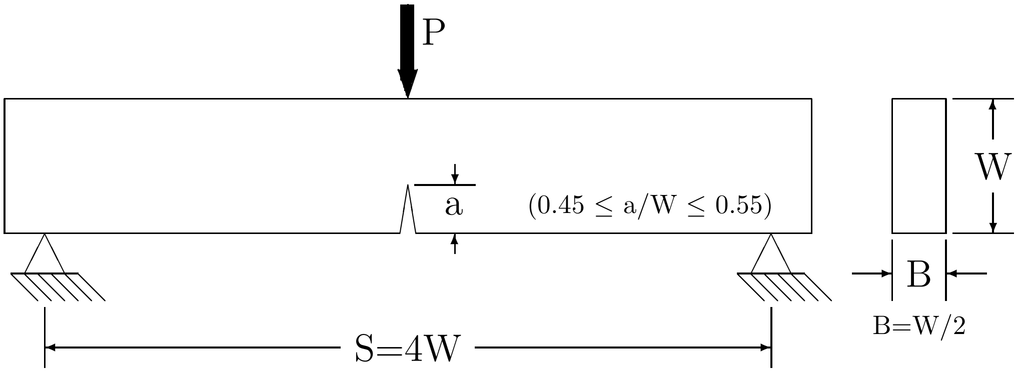

Figure 2.1: Quasistatic three point bend specimen geometry.

The second commonly used geometry is the compact tension or C(T) specimen geometry. For this geometry K_I is given by

$$K_I = \frac{P(2+\frac{a}{W})}{B\sqrt{W}(1-\frac{a}{W})^{3/2}} \left[0.886 + 4.64\frac{a}{W} - 13.32\left(\frac{a}{W}\right)^2 + 14.72\left(\frac{a}{W}\right)^3 - 5.6\left(\frac{a}{W}\right)^4\right] \quad (2.3)$$

which is valid for $\frac{a}{W} \geq 0.2$. C(T) specimen geometry prescribed by ASTM standard *E399* is given in Figure 2.2. *E647* relaxes the thickness requirement given in *E399*, allowing a range of thicknesses $\frac{W}{20} \leq B \leq \frac{W}{4}$.

With both standard geometries, COD and strain gage techniques can be utilized simultaneously without interference, but CGS cannot. CGS requires an unobstructed view of a sizeable area about the crack tip which is not possible with standard C(T) specimens due to the close proximity of the loading grips to the crack tip. The area about the crack tip used by CGS must also be several times larger than the specimen thickness and far from specimen boundaries, which precludes the use of standard bend specimens.

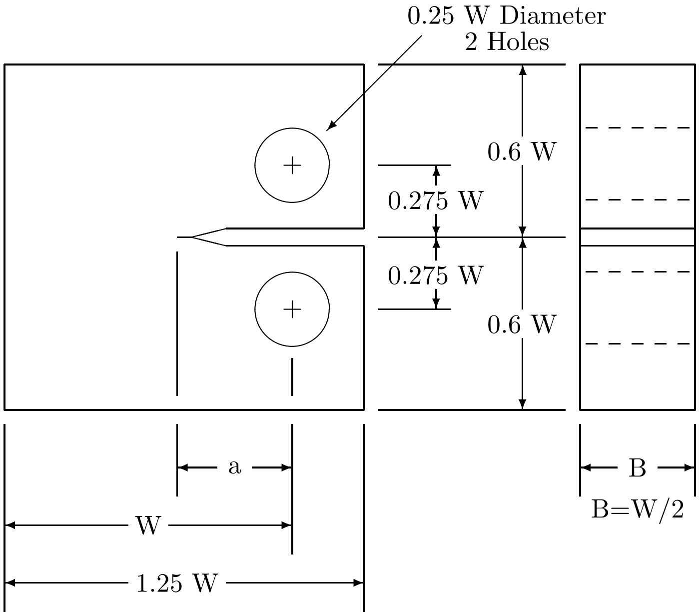

Figure 2.2: Quasistatic compact tension specimen geometry.

2.3 Crack Opening Displacement (COD)

2.3.1 Overview and Governing Equations

Crack Opening Displacement technique involves measuring opening displacements between the crack faces behind the a single crack tip and using theory to relate the opening displacements to the stress intensity factor.

The relationship between crack opening displacement and stress intensity factor used for this work is from Shih [44]. This relationship is obtained using the HRR crack tip solution [20] [38] for power law hardening materials. For power law hardening materials under uniaxial loading, flow stress σ and strain ε is described by a relationship of the form

$$\frac{\sigma}{\sigma_0} = \alpha \left(\frac{\varepsilon}{\varepsilon_0}\right)^n \tag{2.4}$$

where α and n are material constants, the latter called the strain hardening exponent, and σ_0 and ϵ_0 are reference stress and strain respectively.

Employing the standard crack tip coordinate system, (Figure 2.3) the crack opening $\delta(r, t, n)$ is

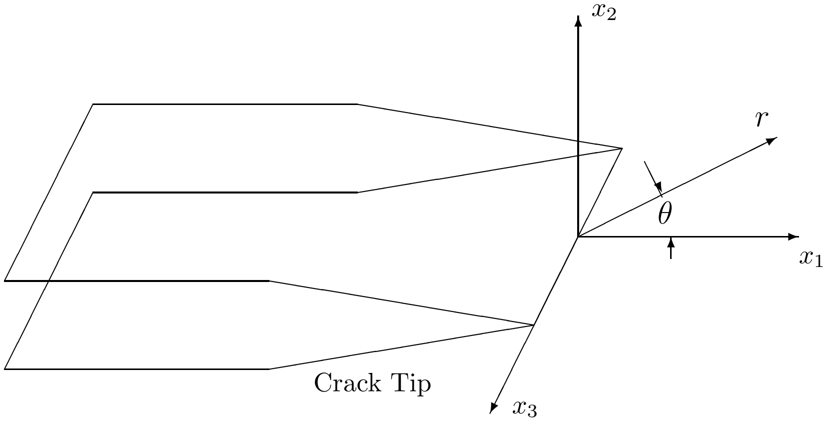

Figure 2.3: Crack tip coordinate system.

given by

$$\delta(r,t,n) = \alpha\varepsilon_0 \left\{ \frac{J(t)}{\alpha\sigma_0\varepsilon_0 I_n} \right\}^{\frac{n}{n+1}} r^{\frac{1}{n+1}} \left[2\tilde{u}_2(\pi,n)\right] \tag{2.5}$$

where I_n is an integration constant and J is the value of the J-integral. The x_1 component of displacement of material points on the crack faces is given by

$$u_1(r,t,n) = \alpha\varepsilon_0 \left\{ \frac{J(t)}{\alpha\sigma_0\varepsilon_0 I_n} \right\}^{\frac{n}{n+1}} r^{\frac{1}{n+1}} \left[2\tilde{u}_1(\pi,n)\right] \ . \tag{2.6}$$

By defining the location of COD measurement δ to be between the points of intersection of the crack faces and radial lines from the crack tip at ±135° (Figure 2.4),

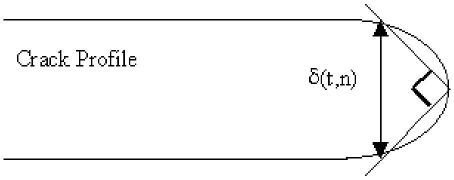

Figure 2.4: Location of crack opening displacement measurement.

$$r - u_1 = \delta/2 \ . \tag{2.7}$$

Equations (2.5-2.7) are satisfied by

$$\delta(t,n) = d_n(n)\frac{J(t)}{\sigma_0} \tag{2.8}$$

where $d_n(n)$ is given by

$$d_n(n) = (\alpha\epsilon_0)^{\frac{1}{n}}\,(\tilde{u}_1(n)+\tilde{u}_2(n))^{\frac{1}{n}}\,\frac{2\tilde{u}_2(n)}{I_n}\,. \tag{2.9}$$

The coefficient $d_n(n)$ is plotted versus strain hardening exponent in Figure 2.5 (plane strain) and Figure 2.6 (plane stress). For linear elastic materials J is related to the stress intensity factor K by

$$J(t) = \frac{K_I^2(t)}{E} \tag{2.10}$$

where E is the material's modulus of elasticity.

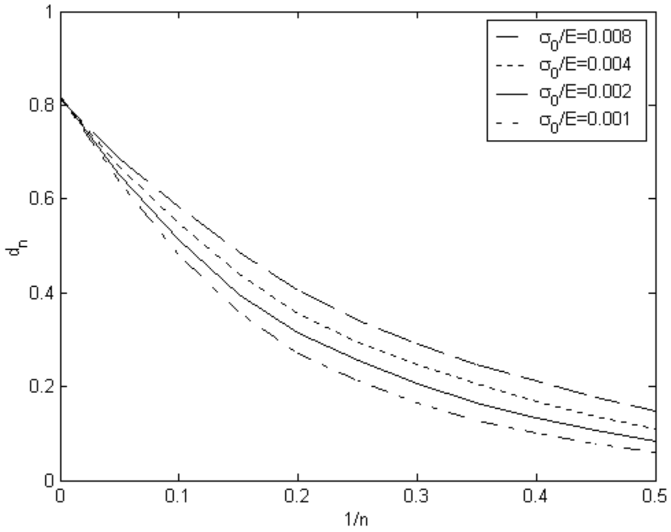

Figure 2.5: d_n versus strain hardening exponent n for plane strain.

Of the three stress intensity factor measurement techniques that can be used dynamically, COD method is most difficult to use. It provides the least amount of information and so requires the most care to get accurate results. However COD measurements can be made on side-grooved specimens, unlike CGS and strain gage measurement techniques, making it invaluable for more ductile materials.

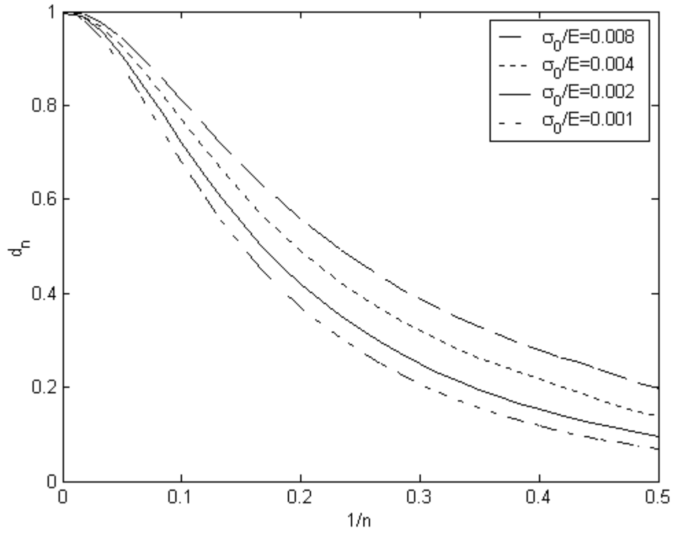

Figure 2.6: d_n versus strain hardening exponent n for plane stress.

The primary difficulty is that given a relationship between COD and K_I^d values, it is very difficult to measure dynamic COD profiles and δ accurately. For quasistatic tests microscope type imaging optics can be located very close to the specimen to obtain highly magnified images of the crack profile. During dynamic tests, optics near the specimen are unlikely to remain undamaged and illumination must be very bright to allow short exposure times. Dynamic measurements are typically made by back-lighting the crack and imaging the light passing through the crack tip with a high speed camera. Because this method records the projection of the crack profile, measured displacements will be conservative. Unless the specimen is very thin, light may never traverse near the crack tip area due to crack roughness and shear lips.

The second difficulty with dynamic measurements is that because the crack tip cannot be imaged, test sequences provide little information, if any, on crack tip location. The determination of initiation time is of paramount importance in determining fracture toughness. Typically in dynamic tests the value of the crack opening δ increases rapidly, and small errors in the time of initiation may lead to large errors in the determination of K_{IC}^d.

2.3.2 Implementation

Given the difficulties of COD method, implementation must be examined on a case by case basis. The procedures outlined in this section are specific to this study but may work with other materials.

For all dynamic COD experiments conducted for this work, no light whatsoever passed through the fatigue pre-crack to the camera prior to initiation. The only location where opening could be observed throughout loading was at the smooth EDM notch from whence the pre-crack was grown by fatigue (Figure 3.11). Since the EDM notch has relatively smooth edges, profiles could be accurately made by back-lighting without risk of significant under-measurement. However, opening measurements made in the EDM notch are at least 2 mm from the crack tip, and not at the location specified in the definition of δ.

The titanium alloys studied in this work behave approximately in a linear elastic perfectly plastic manner (Figure 4.21). By employing this constitutive approximation, the COD analysis is greatly simplified, and opening at the EDM notch can be easily related to δ at the crack tip. Using $n \rightarrow \infty$, the crack opening profile equation (2.5) becomes independent of r, such that the crack faces open in parallel and the opening displacement is equal for all points behind the crack tip. In summary, for the specimens tested, measuring δ at the crack tip at the location of definition (Figure 2.4) is impossible, and so δ must be inferred from opening measurements taken further behind the crack tip at the EDM notch. Assuming elastic perfectly plastic material behavior, crack opening at the EDM notch is equal to δ. Use of this enabling assumption is supported by the experimental results presented later in this chapter.

In all COD measurement experiments, the EDM notch was back-lit with a Spectra-Physics Argon-Krypton-ion laser, model 166-09, operating at a wavelength of $\lambda = 514.5$ nm. A Cordin 330 rotating mirror camera capable of recording 80 images at a rate of up to 2 million frames per second was used to capture images on Kodak TMAX-3200 film. The camera exposes the film by pulsing the laser 80 times with each pulse (exposure) being 8 ns in duration. After being developed, the negatives were scanned to allow digital image analysis. To maximize objectivity the value of δ was taken to be the average of 60-100 individual measurements of EDM opening displacement taken every tenth millimeter starting at the notch tip. As manual estimation of EDM notch edge locations would be subjective, all measurements were performed automatically using Matlab[1] programs. The plane strain value for d_n was used in equation 2.8 to calculate K_I^d.

To determine crack initiation time, the angle between the two EDM edges was measured and plotted versus time. It was assumed that though the crack faces would open in a predominantly parallel manner (which was observed before initiation), after crack initiation the decrease in remaining ligament would result in a jump in rate of hinging and that the angle between the EDM faces would begin to increase rapidly. Initiation time was taken to be when the slope of the EDM angle versus time plot increases. For this work, the initiation time found in this way could be verified by strain gage results from the same test and from measurements from other tests performed at nominally the same conditions. Without this additional information, determining initiation of this material loaded under these conditions measured with this setup would have been very difficult on many of the tests. Representative COD images and associated plots are given in section 2.6.2.

2.4 Strain Gage Measurement

2.4.1 Overview and Governing Equations

Strain gages can be used to measure in-plane surface strain in the vicinity of cracks which can be related to analytic asymptotic stress fields to determine stress intensity factors. This method can be employed for quasistatic or dynamic loading for both initiating and propagating cracks. The primary advantages of strain gages are low cost and simplicity with essentially no special specimen preparation required. Assuming sufficient data acquisition equipment is available, the measurement cost per test is essentially that of the strain gages used. Strain gage measurement setup is also

---

[1] The MathWorks, Inc., 3 Apple Hill Drive, Natick, MA 01760-2098

simple, quick, and relatively fool-proof since the measurement system can be checked for readiness prior to an actual experiment. Strain gages can be used in conjunction with other measurement techniques. Data analysis is quick and uncomplicated.

Strain is easily obtained from resistance strain gages, for example through the use of a standard single arm Wheatstone bridge [12] as shown in Fig 2.7. The resistance strain gage makes one arm of the bridge, with three resistors of the same value filling out the remaining arms. One of the three resistors should be adjustable to allow balancing of the bridge circuit to zero the output prior to testing. Strain is related to the measured bridge output voltage by

$$\varepsilon_g = \frac{4V_o}{GV_i} \tag{2.11}$$

where V_o is the voltage potential across the bridge, G is the gage factor of the strain gage, and V_i is the bridge excitation voltage.

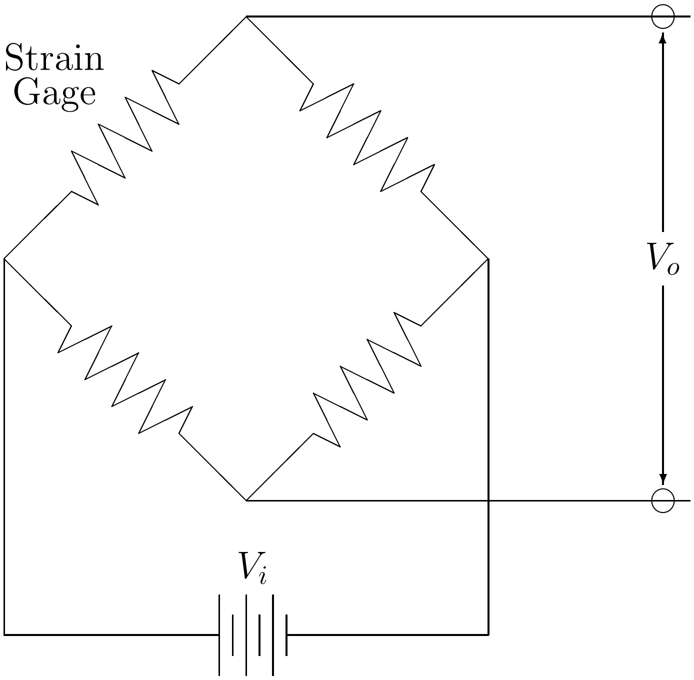

Figure 2.7: Schematic of a Wheatstone bridge used with a resistance strain gage to measure strain.

In the context of the evaluation of near-tip strain fields, field parameters and measured strains are related as follows: For an arbitrary strain gage placement within a region of plane stress (i.e., outside the three-dimensional zone) the measured strain due to quasistatic mode I and mode II stress fields through order r is given by the following (from Dally and Burger [11]):

$$\begin{aligned}
2\mu\varepsilon_{x'x'} &= A_0 r^{-1/2}\left[k\cos\frac{\theta}{2}-\frac{1}{2}\sin\theta\left(\sin\frac{3\theta}{2}\cos 2\alpha-\cos\frac{3\theta}{2}\sin 2\alpha\right)\right]+B_0(k+\cos 2\alpha) \qquad (2.12)\\
&\quad +A_1 r^{1/2}\cos\frac{\theta}{2}\left(k+\sin^2\frac{\theta}{2}\cos 2\alpha-\frac{1}{2}\sin\theta\sin 2\alpha\right)\\
&\quad +B_1 r\left[(k+\cos 2\alpha)\cos\theta-2\sin\theta\sin 2\alpha\right]\\
&\quad +C_0 r^{-1/2}\left[-k\sin\frac{\theta}{2}-\cos 2\alpha\left(\frac{1}{2}\sin\theta\cos\frac{3\theta}{2}+\sin\frac{\theta}{2}\right)\right.\\
&\quad \left.-\sin 2\alpha\left(\frac{1}{2}\sin\theta\sin\frac{3\theta}{2}-\cos\frac{\theta}{2}\right)\right]\\
&\quad +C_1 r^{1/2}\left[k\sin\frac{\theta}{2}+\cos 2\alpha\left(\frac{1}{2}\sin\theta\cos\frac{\theta}{2}+\sin\frac{\theta}{2}\right)+\sin 2\alpha\left(\frac{1}{2}\sin\theta\sin\frac{\theta}{2}+\cos\frac{\theta}{2}\right)\right]\\
&\quad +2D_1 r\left[\sin\theta\,(k+\cos 2\alpha)\right]
\end{aligned}$$

where $k=(1-\nu)/(1+\nu)$, μ and ν are the material's shear modulus and Poisson's ratio respectively, r and θ specify the strain gage location with respect to the crack tip coordinates, α indicates the angle of strain measurement with respect to the crack tangent (Figure 2.8), and $\varepsilon_{x'x'}$ is the strain measured by the gage. Use of the above equations precludes non-planar specimen geometries such as those with side-grooves. In equation (2.12), in-plane stress intensity factors and singular term coefficients are related by

$$A_0 = \frac{K_I}{\sqrt{2\pi}} \qquad (2.13)$$

$$C_0 = \frac{K_{II}}{\sqrt{2\pi}}\,. \qquad (2.14)$$

Using equations (2.12–2.14), stress intensity factors can be obtained from strain gages by any sufficient combination of the following:

1. Eliminating terms by assumption. For example, assumption of a purely mode I field eliminates the terms with coefficients C_0, C_1, and D_1. In addition, the contribution of higher order terms may be negligible in comparison to the leading terms.

2. Eliminating terms by gage orientation. Gage placement and orientation angles can be chosen

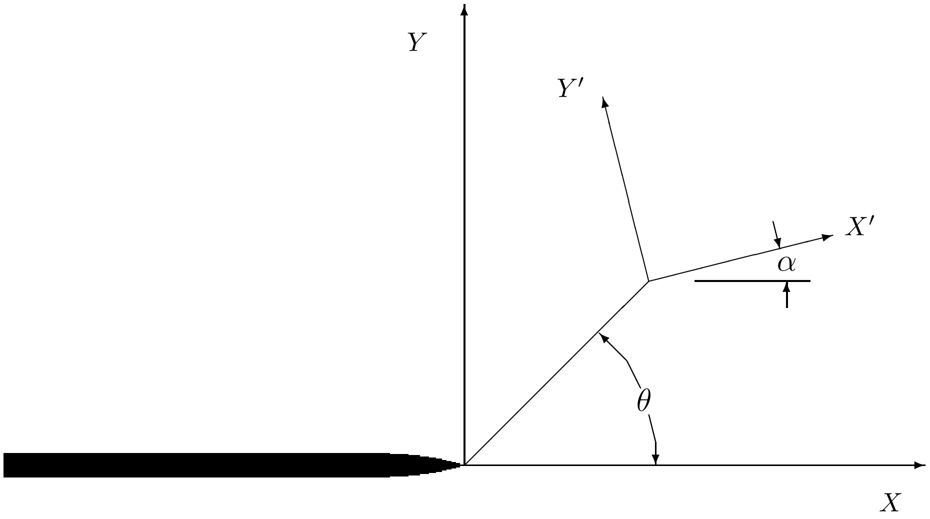

Figure 2.8: Coordinate system for strain gage placement and orientation.

to eliminate up to two terms.

3. Using additional gages. With one gage per remaining unknown coefficient, each positioned to provide unique information, the coefficients can be determined using linear algebra. By using additional gages the system of equations is overdetermined and the coefficients can be obtained by a least-squares fit.

The combination of tactics employed must be guided by the fact that only so many gages can be physically located around the crack tip—each gage must be located beyond extensive crack tip plastic deformation but within the area described by the asymptotic terms used. Stress intensities and speeds of propagating cracks may be measured by locating strain gages ahead of the initial crack tip oriented with respect to anticipated crack tip location. While equation (2.8) is for a stationary quasistatic crack, the singular terms are the same for any crack condition so long as crack speed is much less than the material shear wave speed.

Methodology for measuring K_I^d and T stress with single gages is given in the next two sections. Dally and Burger [11] contributed the former procedure and results, and provide useful examples on using multiple gages, monitoring moving cracks, etc.

2.4.2 Measuring K_I^d with One Strain Gage

For mode I cracks ($C_0 = C_1 = D_1 = 0$) the coefficient of B_0 is zero if the strain gage orientation angle α is chosen such that

$$\cos 2\alpha = -k = -\frac{1-\nu}{1+\nu} \tag{2.15}$$

and the coefficient of the A_1 term is likewise eliminated by choosing strain gage position angle θ so

$$\tan\frac{\theta}{2} = -\cot 2\alpha\ . \tag{2.16}$$

For a single strain gages positioned in this manner, its output will be related to K_I^d by

$$2\mu\varepsilon_{x'x'} = \frac{K_I^d}{\sqrt{2\pi r}}\left[k\cos\frac{\theta}{2} - \frac{1}{2}\sin\theta\left(\sin\frac{3\theta}{2}\cos 2\alpha - \cos\frac{3\theta}{2}\sin 2\alpha\right)\right] + O(r)\ . \tag{2.17}$$

Both angles are functions of Poisson's ratio ν and are tabulated in Table 2.1. The contribution of higher order terms can be detected by comparing values from two gages placed at different radii.

ν	θ (degrees)	α (degrees)
0.250	73.74	63.43
0.300	65.16	61.29
0.333	60.00	60.00
0.400	50.76	57.69
0.500	38.97	54.74

Table 2.1: Strain gage angles to measure K_I^d with single strain gage.

For the simplest case of $\nu = 1/3$, $\alpha = \theta = 60°$ and

$$K_I^d = E\sqrt{\frac{8}{3}\pi r}\,\varepsilon_g \tag{2.18}$$

where $\varepsilon_g = \varepsilon_{x'x'}$ is the strain gage output.

Usually the strain measured by a gage is taken to be the value at an infinitesimal point located at the center of the gage. Since the actual strain field measured does not vary linearly with r, this approximation introduces error for a gage of finite area. By assuming a K_I-field with strain measured by a strain gage positioned as described above, Dally and Burger show that the radius r used in conjunction with the strain gage measurement should not be that to the center of the gage (r_c), but instead $r_c - \Delta r$, with Δr given by

$$\frac{\Delta r}{r_c} = \frac{1}{2}\left\{1 - \left[1 - \left(\frac{L}{2r_c}\right)^2\right]^{1/2}\right\} \tag{2.19}$$

where L is the strain gage's gage length. This function is shown in Figure 2.9. In practice, minimal gage location radius is limited to the maximum of half strain gage size (for which gradient-error must be corrected), three-dimensional zone radius (equal to half the specimen thickness) where plane stress assumptions for equation (2.12) begin to fail, and extent of any anticipated shear lips, which is more of a problem with running cracks. The gage also must be located within the region of dominance associated with the asymptotic terms used, the closer to the crack tip the better. Often the gradient-error correction will be less than the uncertainty in strain gage position. The gradient-error correction depends on gage position and orientation, as well as on the stress terms anticipated to be present—equation (2.19) is for a gage placed with $\alpha = \theta = 60°$ in a pure K_I-field only. The constraints on gage location, however, is the same for all configurations.

2.4.3 Measuring T Stress with One Strain Gage

After the singular terms in the crack tip asymptotic solution, the next lowest order term (r^0) is the T stress, or uniform σ_{11} term which only appears in the mode I asymptotic solution. Motivated by the fact that CGS is insensitive to this term, the same approach as employed for K_I^d is used to determine strain gage angles for isolating the T term and relating it to measured strain. Again pure mode I is assumed and α and θ are chosen to eliminate the coefficients of the K_I term and the C_0 term. These angles are again functions of Poisson's ratio ν and must be found numerically. They are tabulated for different values of ν in Table 2.2.

Noting

$$T = 2B_0 \tag{2.20}$$

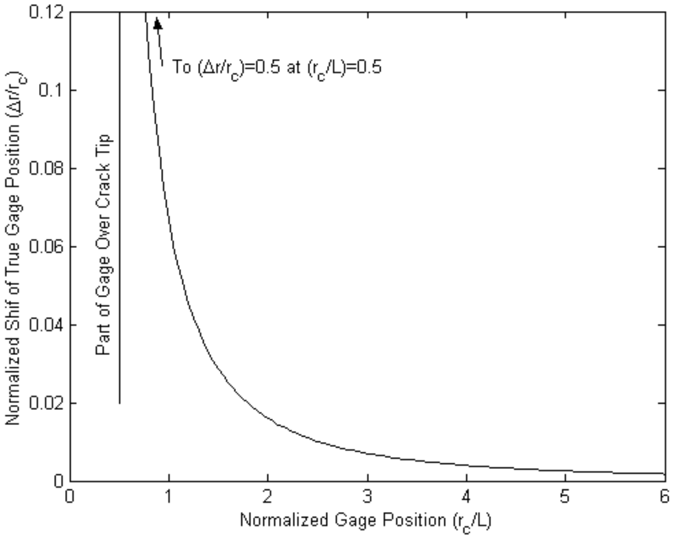

Figure 2.9: Normalized decrease in strain gage location radius versus radius to gage center for eliminating strain gradient error.

ν	θ (degrees)	α (degrees)	$k+\cos 2\alpha$
0.250	101.53	50.77	0.400
0.300	94.41	47.21	0.462
0.333	90	45	0.5
0.400	81.79	40.89	0.572
0.500	70.53	35.26	0.667

Table 2.2: Strain gage angles to measure T-stress with a single strain gage.

the T stress is related to the strain gage measurements by the following:

$$2\mu\varepsilon_{x'x'} = \frac{T}{2}\left(k+\cos 2\alpha\right) + O(r)\ . \tag{2.21}$$

The quantity $k+\cos 2\alpha$ is also tabulated versus ν in Table 2.2. As expected, the value of T is independent of radius r to first order, and the presence of higher order terms can be detected by taking measurements with two gages placed at different radii. By placing the two gages on opposite sides of the specimen, erroneous contributions due to specimen buckling can also be detected and negated by using their average value.

For the simplest case of $\nu = 1/3$, $\alpha = 45°$ and $\theta = 90°$, and the T stress is given by

$$T = 8\mu\varepsilon_{x'x'} \, . \tag{2.22}$$

For this gage orientation and with $\nu = 1/3$, the coefficient of C_0 is also zero, indicating that these measurements are also insensitive to the singular K_{II}-field. For other values of ν, sensitivity is very low.

2.5 Coherent Gradient Sensing (CGS)

2.5.1 CGS Overview

CGS is a full-field optical interferometric method which can measure surface slopes for reflective specimens, and geometric and stress induced optical property changes for transparent specimens (Tippur *et al* [48] [49]). Used with simple specimen geometries (i. e., flat plates), information from CGS interferograms can be compared to that predicted by fracture models, for example LEFM, to extract fracture/field parameters. It is similar to the optical method of caustics (Theocaris [47], Kalthoff [25], Rosakis [41]) in principle but provides full-field measurement. Its sensitivity to *gradients of displacements* makes it ideal for measuring singular fields such as those about a crack tip. Other optical techniques which instead measure *displacements*, such as moiré interferometry (Post [35]), can provide useful fringe patterns only within a small displacement range and thus have limited usefulness in singular fields. CGS is insensitive to vibration and is well suited for high speed photography, making it an ideal measurement technique for dynamic fracture studies. While in principal CGS is applicable to quasistatic fracture measurement, in practice crack tip mechanical fields of reasonably sized ASTM standard C(T) and bend specimens are influenced by load point fields and boundary effects. While such effects have minimal influence very close to the crack tip, they are significant in much of the area measured by CGS, rendering fringe patterns difficult to analyze.

As a full-field measurement technique, CGS supplies the most detailed crack information regarding the near-tip mechanical field of the three dynamic stress intensity factor measurement techniques. With sufficiently sophisticated data analysis, this technique can be used to provide stress intensity factor measurements for any combination of mode I and mode II loading, as well as the coefficients of the higher order terms of the crack tip asymptotic solution used. Given higher order term coefficients, the size of the K dominated field can be examined to determine K-dominance assumption validity. Crack tip position can also be determined from CGS interferograms and used to establish initiation time and calculate crack speed. By analyzing many well timed images from a single test, CGS can measure loading rate, initiation toughness, and propagation toughness.

In practice the implementation of CGS requires extensive specimen preparation. For opaque materials one surface must be made optically flat and highly reflective. In metals this may be accomplished by lapping, polishing, and, if necessary, depositing a thin layer of highly reflective aluminum. The experimental setup is complex. Fringe pattern images must be captured by high speed photography which requires precise timing, accurate triggering, and careful optical alignment.

2.5.2 CGS Setup

CGS can be employed in reflection (Figure 2.10)[2] or transmission (Figure 2.11) configurations. In the reflection configuration a mirror-finished region of interest (optically flat prior to loading) is interrogated by an expanded collimated coherent laser beam. After the laser beam reflects off the deformed specimen surface, it passes through two diffraction gratings which process the beam to yield fringes of constant gradient of out-of-plane displacement. The fringe patterns from the first order diffraction are imaged using a focusing lens, an aperture, and a high speed camera.

In transmission mode the interrogating laser beam passes through a transparent specimen and is influenced by geometric and stress induced optical property changes before being processed by the

---

[2] The beam splitter can be omitted by reflecting the beam off the specimen at an angle sufficient to avoid incoming beam obstruction by the gratings.

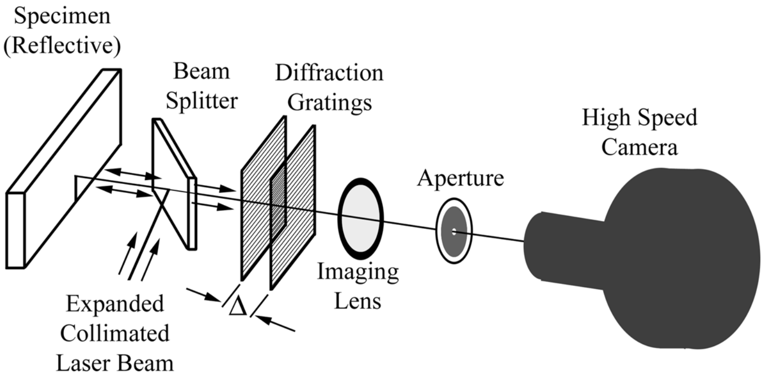

Figure 2.10: Schematic of experiment setup for reflection CGS.

two diffraction gratings. Figure 2.12 shows a transparent PMMA specimen which is to be loaded dynamically in three point bending in a drop weight tower. Also visible are the two diffraction gratings, the imaging lens, and a mirror behind the specimen used to direct the expanded collimated laser beam through the specimen from behind toward the optics and camera.

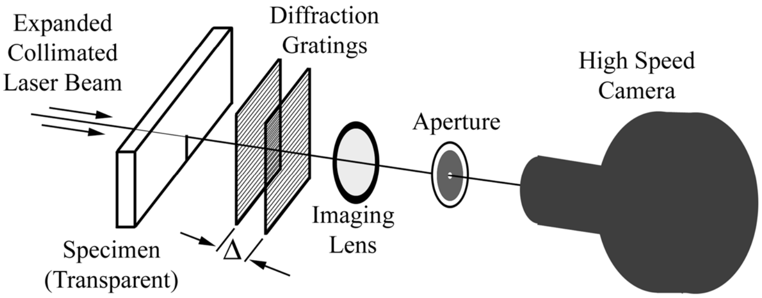

Figure 2.11: Schematic of experiment setup for transmission CGS.

CGS works best on materials that are fairly brittle and maintain a smooth surface during loading.

2.5.3 Implementation

For this work the same high speed camera and illuminating laser were used as for the COD technique. Fast fine grained Kodak TMAX-400 black and white film was used to record the interferograms.

Figure 2.12: Photograph of experiment setup for transmission CGS.

Triggering was accomplished by mounting a strain gage on the specimen at the drop weight impact point. The gage resistance was measured using a Wheatstone bridge whose output at gage impact drives the trigger/timing circuitry.

No CGS tests were conducted on side-grooved specimens as no simple relationship exists between CGS fringe patterns and the crack tip stress field for this geometry. After each test the film was developed and digitized. Using Matlab Graphical User Interfaces (GUIs) developed for this work, the fringe patterns were digitized and fit to mode I and mode II leading and second order asymptotic terms as described in section 3.5.

Chapter 3 provides the governing equations for CGS technique, the asymptotic crack tip solution used and how it is related to the CGS fringes, and how the fringe pattern fitting is performed and the crack tip located. A comparison of stress intensity factors obtained by different choice of asymptotic terms for fitting is also made.

2.6 Experimental Comparison of Measurement Techniques

2.6.1 Material System and Geometries

The material used for all comparisons is a commercially pure 6Al-4V titanium alloy with nominal properties given in Table 2.3.

Ultimate Stress	860 MPa (125 ksi)
Yield Stress	790 MPa (115 ksi)
Young's Modulus	120 GPa (17400 ksi)
Poisson's Ratio	0.32
Tensile Elongation	10%
Reduction of Area	25%
Hardness	R_c=35
Density	4.5 g/cm^3 (0.16 lb/in^3)

Table 2.3: Nominal properties of commercial grade 6Al-4V titanium alloy.

All specimens were cut from titanium plate having a nominal thickness of 0.5 inch. Except for three C(T) specimens used for quasistatic testing, all specimens use three point bend geometry with overall in-plane dimensions of 4 inches by 10 inches. The lower span in all dynamic tests is 230 mm. While some may debate whether initiation toughness depends on instantaneous loading rate $\dot{K}$ at initiation or on some average loading rate over time, use of this tall bend specimen geometry tends to produce dynamic loading rates that are fairly constant rendering this finer point immaterial. The instantaneous loading rate at initiation is reasonably close to the average loading rate. The large in-plane dimensions are also necessary to allow crack tip mechanical fields to develop free of boundary effects, even after initiation and some propagation, which is of particular importance for the CGS technique.

Sharp pre-cracks were produced by first cutting a 1.25 inch notch using wire EDM and then fatiguing 2 mm of crack extension. It was observed that any interruption of fatiguing that involved complete unloading of the specimen made subsequent fatiguing impossible without greatly increased (by about 50%) loads. Such specimens were only acceptable for preliminary tests to establish timing. It appears that any complete unloading allowed the specimen to relocate with respect to the loading fixture, and upon reloading this movement causes some regions of the crack tip to experience stresses higher than those normally used during fatiguing. The resulting plastic flow retards fatigue crack growth.

Side-grooves were cut by plunge EDM in some specimens according to ASTM standard *E647-00*. Side-groove depth is indicated by total thickness reduction by the grooves as a percentage of the specimen's ungrooved thickness.

Side-grooves can be thought of as functioning somewhere between two limits: One, as adding reinforcement to material adjacent to a crack in a specimen with thickness B_N (equation (2.1)), and two, as "pre-machining" shear lips off of a thicker specimen. Ultimately the side grooves' effect is to cause the crack to exist in more of a plane strain condition.

In tests performed on ungrooved specimens of the 6Al-4V Ti used in this chapter, shear lips grew to nearly 100% on quasistatically tested specimens (Figure 4.7). On dynamically tested material the shear lips typically grew to a width of about a third the specimen thickness after 10-15 mm of crack growth (Figure 4.8). For strain gages mounted ahead of the initial crack tip, the shear lips make magnitudes of measurements unreliable though the data is still useful for determining when a moving crack tip passes by.

Prior to dynamic testing, three quasistatic tests were performed on ASTM standard C(T) specimens with nominal thickness of a half-inch and in-plane dimensions $W = 84$ mm and crack length $a = 20$ mm. Two tests on specimens without side-grooves produced quasistatic critical stress intensity values $K_{IC} = 125.1$ and $129.1 MPa\sqrt{m}$ using loading rates of 0.37 and $0.70 MPa\sqrt{m}\, s^{-1}$ respectively. Both failed specimens failed fairly abruptly in displacement control and exhibited minimal shear lips. One specimen with 21.3% side-grooves was tested under the same conditions as the non-side-grooved specimen to obtain a value of $K_{IC} = 93.1 MPa\sqrt{m}$ at a loading rate of $0.80 MPa\sqrt{m}\, s^{-1}$. Only this calculation required the use of the effective thickness B_{eff} defined in equation (2.1). CGS and strain gage techniques as developed do not work with side-grooved specimens, and COD calculations do not depend on specimen thickness. The discrepancy between fracture toughness values for the side-grooved specimen and the two specimens without side-grooves suggest that the latter are not thick enough to produce plane strain initiation values at this loading rate. This is supported by the observation of 100% shear lips.

For the dynamic loading an Instron Dynatup 8100A drop weight tower with a 200 kg tup mass was used.

Data is given from tests using 3 m/s and 9 m/s impact speeds. In all plots, initiation time is indicated by a vertical dashed line. Strain gage and CGS data are obtained simultaneously from the same experiments. COD data from specimens with and without side-grooves are shifted temporally to share initiation time with the strain gage/CGS test of the same impact speed.

2.6.2 Test Results

First, results from experiments using a 3 m/s impact speed are presented.

Stress intensity results are given in Figure 2.13 from three tests using 3 m/s impact speeds. The first test utilized a strain gage and CGS to simultaneously measure the stress intensity factor as a function of time. Overall agreement is good though the initiation value K_{IC}^{d} from the strain gage is 13% less than the same from CGS. The time scale of the “humps” in the strain gage data is about that of the time for Rayleigh waves to transverse the specimen. Two COD tests were run, one on a specimen with side-grooves and the other without. Both COD tests match the CGS data well. The specimen with 22.1% side-grooves initiate more quickly after impact than the two specimens without side-grooves—this is manifest in the plot as a delay of about 60 μs before loading starts compared to the other tests.

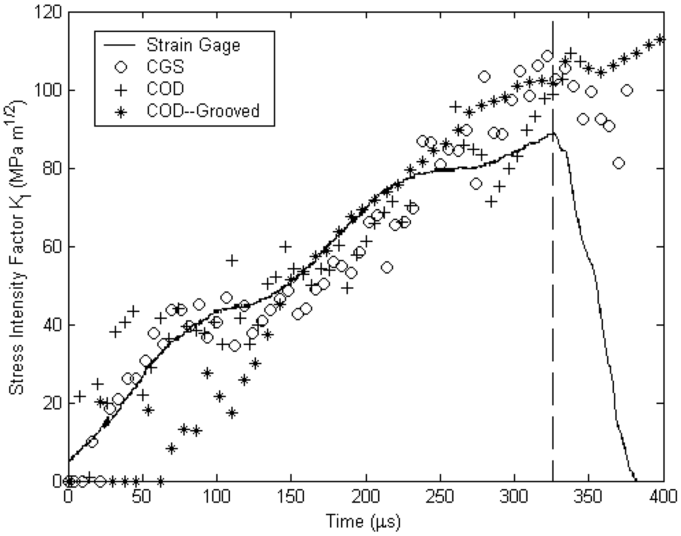

Figure 2.13: Comparison of dynamic stress intensity factors K_I^d versus time as obtained by different measurement methods for 6Al-4V Ti specimens impacted at 3 m/s.

Initiation time for the strain gage trace is taken to be the time at peak strain. CGS provides crack tip location (Figure 2.14) which indicates an initiation time which agrees well with the strain gage initiation time. The noise in crack tip location prior to initiation is typical and is due primarily to imprecision of locating a fixed reference point on the specimen and the limited amount of fringe data during early loading stages. As described in chapter 3, CGS fringe data is used to objectively locate the crack tip within the black caustic zone.

Figure 2.15 shows crack opening angle versus time from the ungrooved specimen. From 150 μs to initiation time the angle is constant as the crack opens. At an initiation time and calculated stress intensity in agreement with the strain gage/CGS results, the crack opening angle begins to increase.

For the side-grooved specimen no distinct change in COD opening angular velocity appears, but the values of K_I^d appear to drop slightly at initiation and then jump afterward as visible in Figure 2.13. This occurs at values consistent with the other two tests. In the absence of the other

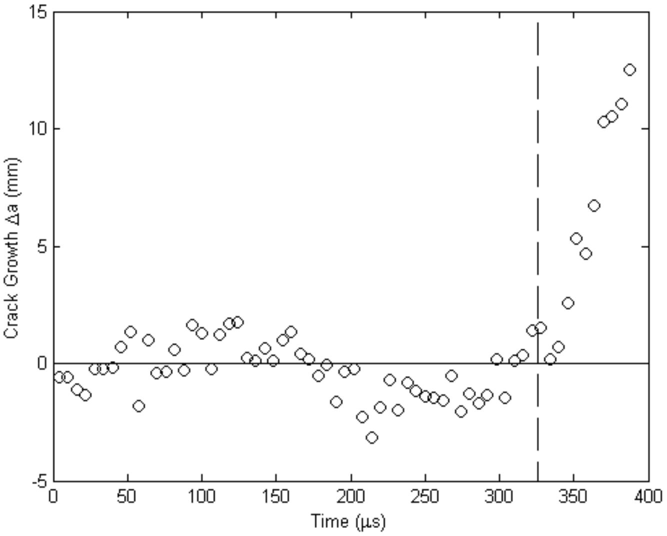

Figure 2.14: Crack tip position versus time as obtained by CGS for a 6Al-4V Ti specimen impacted at 3 m/s.

results it is doubtful that initiation time and thus K_{IC}^{d} could be determined with much confidence.

Figure 2.16 shows a sequence of CGS images at 18, 163, 326, and 388 μs which are at the beginning of loading, midway to initiation, initiation, and post initiation respectively. The crack extends upward from the bottom of each image. The position of the zeroth order fringe is indicated by a "0." The first image shows that the specimen surface has slight curvature prior to loading which is manifest as a wide horizontal dark fringe above the crack tip. The second image looks the most like theoretical fringe patterns from a K_I-field except, unfortunately, the fringe intensities are reversed due to some combination of the initial curvature and wave loading. Instead of calling white fringes black and vice versa, the fringe numbering was chosen as indicated to reconcile best with previous and subsequent images in the test sequence. Temporally local fringe numbering difficulties like this are not unusual. By initiation the fringes look typical, and after initiation the fringe patterns are highly distorted but the rear lobes are analyzable. Typically, the front lobe (ahead of the crack tip) is the most prone to be distortion by loading waves and specimen flex as exemplified in the third and

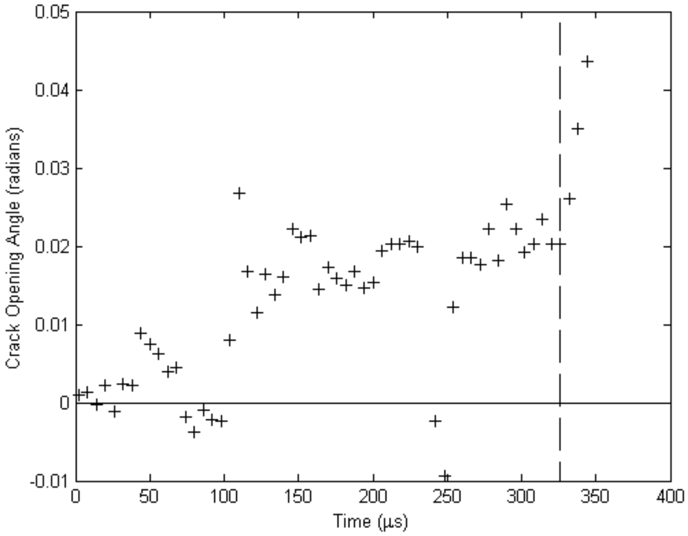

Figure 2.15: Crack/EDM notch opening angle versus time for a 6Al-4V Ti specimen with no side-grooves impacted at 3 m/s.

fourth fringe patterns, and the best data usually comes from the rear lobe. While previously much more problematic, fringe sequences such as these can now be analyzed successfully using approaches described in chapter 3.

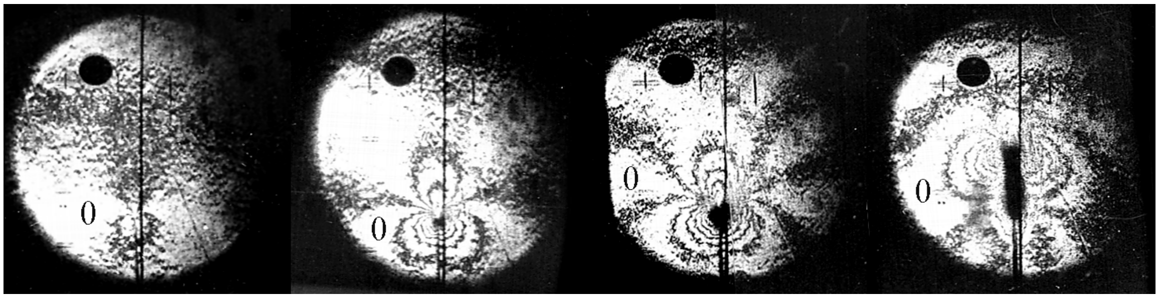

Figure 2.16: CGS fringe patterns at (left to right) 18, 163, 326, and 388 μs for a 6Al-4V Ti specimen impacted at 3 m/s. (Beam diameter = 50 mm)

Figure 2.17 shows COD profiles for a crack at about the same times as the CGS images above, except for the fourth profile which is earlier. The length of the EDM notch initially visible is

12.71 mm, and the crack tip, which cannot be seen, is located about 2 mm above the top of the EDM notch. It is obvious that the notch widens as the crack loads, but little else can be observed without digitizing the profile and post-processing.

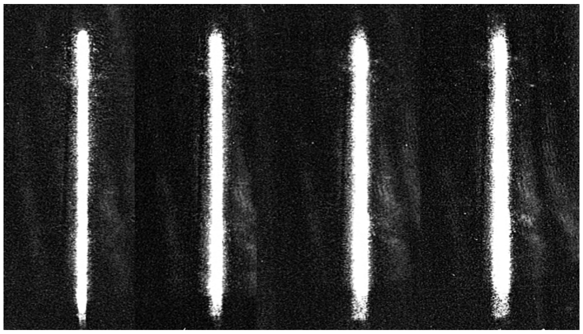

Figure 2.17: COD profiles at (left to right) 20, 164, 326, and 344 μs for a 6Al-4V Ti specimen impacted at 3 m/s. (Initial notch length visible = 12.71 mm)

Four COD profiles for the side-grooved specimen are shown in Figure 2.18, each at the same times as the four CGS fringe patterns. The length of the EDM notch initially visible is 10.57 mm. Again it is apparent that the notch opens measurably from image to image, but further information is not obtainable without digitizing and post-processing.

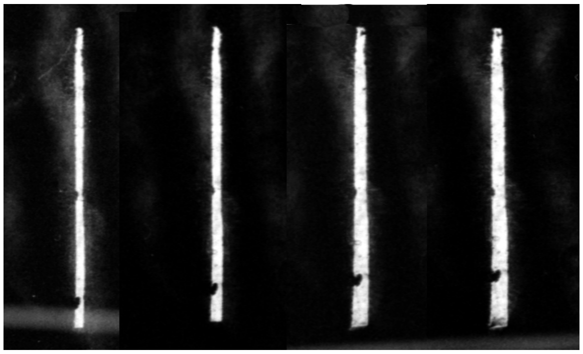

Figure 2.18: COD profiles at (left to right) 22, 166, 326, and 390 μs for a side-grooved 6Al-4V Ti specimen impacted at 3 m/s. (Initial notch length visible = 10.57 mm)

Three similar tests were also conducted using a 9 m/s drop weight impact speed. For the first test, the initiation value K_{IC}^d from the strain gage is 18% higher than the same from CGS. Both COD tests match the CGS data fairly well also. If the COD data for the specimen without side-grooves were offset in time to superimpose the loading portion with the strain gage data, the agreement in initiation toughness would be excellent. This suggests that the identification of initiation time is key to determining the value of K_{IC}^d from COD measurements. Again the side-grooved specimen (23%) initiates more quickly after impact than those specimens without side-grooves.

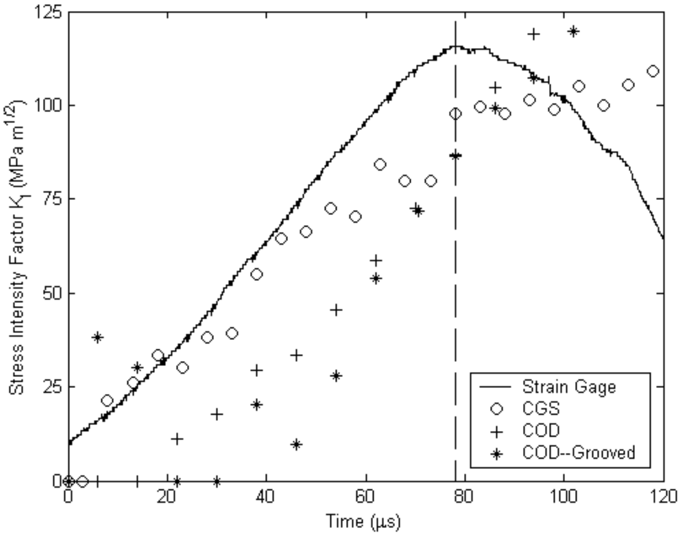

Figure 2.19: Comparison of dynamic stress intensity factors K_I^d versus time as obtained by different measurement methods for 6Al-4V Ti specimens impacted at 9 m/s.

Again, initiation time for the strain gage trace is taken to be the time at peak strain. The CGS measured crack tip location history indicates the same initiation time (Figure 2.20).

For the COD measurements on the ungrooved and grooved specimens, crack initiation was indicated by a jump in crack opening angular velocity (Figure 2.21).

Figure 2.22 shows a sequence of CGS images at 3, 38, 78, and 138 μs which are at the beginning of loading, midway to initiation, initiation, and post initiation respectively. The crack extends upward from the bottom of each image. The position of the zeroth fringe number is indicated by a

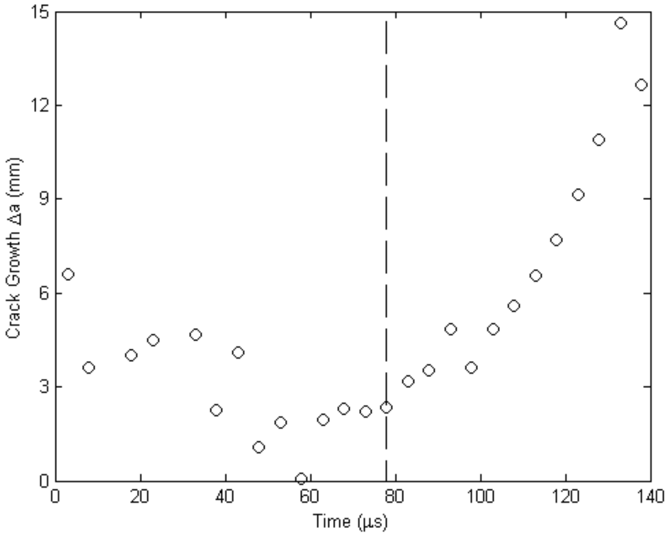

Figure 2.20: Crack tip position versus time as obtained by CGS for a 6Al-4V Ti specimen impacted at 9 m/s.

"0." As with the 3 m/s test, the first image shows that the specimen surface has slight curvature prior to loading. The remaining fringe patterns are affected by this curvature, but are otherwise straightforward to analyze.

Figure 2.23 shows COD profiles for a crack at about the same times as above. The EDM notch initially visible is 10.82 mm long and the crack tip, which cannot be seen, is located about 2 mm above the EDM notch. The same for side-grooved specimen are shown in Figure 2.24, all at the same times as the CGS fringe patterns. For this specimen the amount of EDM notch initially visible is 10.95 mm. Again it is apparent that the notch opens measurably from image to image, but further information is not obtainable without digitizing and post-processing. The fatigue crack is visible in the final image, but no light passes through behind the propagating crack.

The agreement between COD measurements from specimens with and without side-grooves suggests that in this dynamic loading regime the ungrooved specimens are thick enough to produce plane strain fracture toughness values.

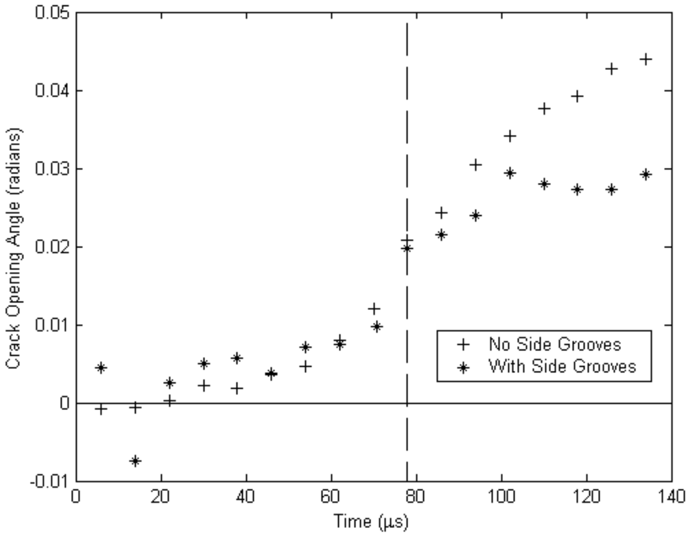

Figure 2.21: Crack/EDM notch opening angle versus time for 6Al-4V Ti specimens with and without side-grooves impacted at 9 m/s.

2.7 Conclusions

As implemented, the three experimental techniques provide comparable values of dynamic stress intensity factors versus time and initiation toughness for 6Al-4V Ti. Due to measurement error and natural variation in real materials, quasistatic fracture toughnesses are sometimes reported without specifying whether the units are $MPa\sqrt{m}$ or $ksi\sqrt{in}$, which ambiguity can introduce an error of almost 10%. Therefore, obtaining dynamic initiation toughness values for an engineering material using three fundamentally different techniques which agree, for the most part, to this level must be considered a success. It would be useful to repeat these tests many times and perform a statistical evaluation of the results. With the few tests results reported here, the toughness discrepancies due to measurement error as opposed to natural material variation is unknown.

CGS as newly employed (described in the next chapter) is somewhat self checking in that the analysis provides information which can be cross checked and compared to the original measurements. Stress fields associated with higher order terms obtained from analysis can be compared with the

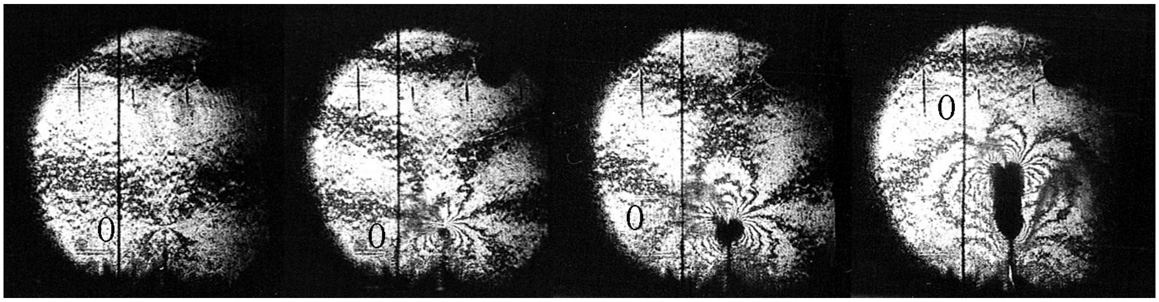

Figure 2.22: CGS fringe patterns at (left to right) 3, 38, 78, and 138 μs for a 6Al-4V Ti specimen impacted at 9 m/s. (Beam diameter = 50 mm)

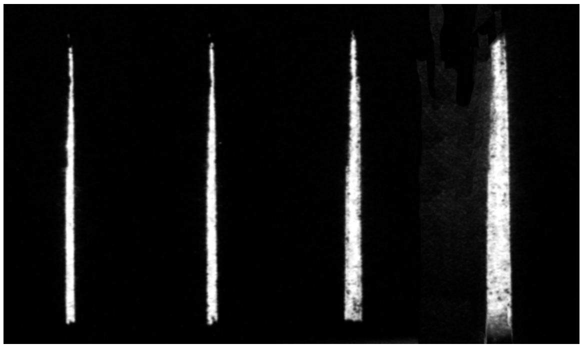

Figure 2.23: COD profiles at (left to right) 6, 38, 78, and 142 μs for a 6Al-4V Ti specimen impacted at 9 m/s. (Initial notch length visible = 10.82 mm)

stress intensity factor to evaluate the validity of the K-dominance assumption. Analysis of many sequential fringe pattern images is performed almost completely objectively, thus the level of noise in measured values is indicative of the amount of random measurement error. The implementation also utilizes a metric of fitting error which describes how well the fringe patterns of the crack tip mechanical field correlate with the LEFM crack tip asymptotic solution terms used. The abundance and correlation of information obtained by CGS helps to build confidence in its measurement results and establish it as the benchmark for evaluation of the other two methods in this case where all three methods can be used.

The strain gage technique proves itself as an easy, inexpensive method to obtain stress intensity

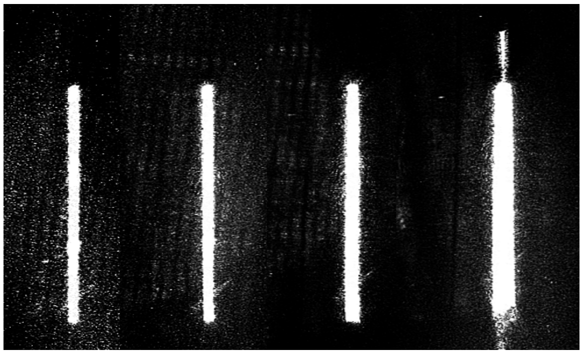

Figure 2.24: COD profiles at (left to right) 6, 38, 78, and 142 μs for a side-grooved 6Al-4V Ti specimen impacted at 9 m/s. (Initial notch length visible = 10.95 mm)

factors. The assumption that strain output is maximum at initiation is supported by CGS results. The fact that results from a single gage measuring strain in the neighborhood of one point correlates so well with CGS results is encouraging.

Finally, comparing results from COD to CGS suggests that the enabling assumptions made for employing COD technique are sufficiently justified. Using opening measurements behind the crack tip in the EDM notch is essential as no light transverses through the fatigue crack until after crack initiation has already occurred. The elastic perfectly plastic material constitutive behavior assumption may contribute a systematic error, but given the uncertainty in d_n (equation 2.8), simplification by this assumption is rational. d_n is only calculated for two-dimensional models, plane stress and plane strain, whereas the effective value for a three-dimensional specimen may be between the two calculated values. A more pressing need for COD technique is a more accurate method of determining initiation time. For this work the opening angular rate suffices due to verification by the other measurement techniques. While strain gages can be used to detect initiation in ungrooved specimens, specimens with side-grooves may require the development of some alternative method.

Chapter 3

Improvements in Implementation of Coherent Gradient Sensing Technique

3.1 History and Overview

Coherent Gradient Sensing technique (CGS) was developed at Caltech by Rosakis and associates [41] as a full-field alternative to the optical method of Caustics. As outlined in section 2.5, CGS technique has many properties which are ideal for many dynamic fracture mechanics applications.

CGS produces fringes which can be related to gradients of $\hat{\sigma}_{11} + \hat{\sigma}_{22}$, in particular for flat plates under plane stress loading. This information can then be compared to predictions by fracture models to extract fracture/field parameters. Usually fringe patterns of crack tip singularities are analyzed within the context of LEFM.

Previously for simplicity, CGS has usually been employed for nominally mode I experiments with fringe data fit to a K_I-field only, though Tippur *et al.* [49] and Prabhu *et al.* [36] for example have added higher order terms, both utilizing the the Williams' expansion [51] for a *static* mixed mode crack:

$$\frac{\partial(\hat{\sigma}_{11}+\hat{\sigma}_{22})}{\partial x_1} = \sum_{N=1}^{\infty}\left(\frac{1}{2}N-1\right) r^{\left(\frac{N}{2}-2\right)}\left[A_N \cos\left(\frac{1}{2}N-2\right)\theta + B_N \cos\left(\frac{1}{2}N-2\right)\theta\right] . \tag{3.1}$$

In the above $A_1 = 2K_I/\sqrt{2\pi}$ and $B_1 = 2K_{II}/\sqrt{2\pi}$ and as indicated the gradient direction is x_1. Freund and Rosakis [17] obtained asymptotic terms through order r^2 for a mode I transient crack growth. This generalization adds several angular terms not found in the static expansion. This result was used with transmission CGS to describe transient failure of PMMA.

Prior to this work, CGS analysis has been employed with capability to analyze fringe patterns with gradients taken in the x_1 or x_2 directions only. This restriction greatly limits CGS application possibilities and may introduce fitting errors. This shortcoming and its simple fix is described in sections 3.5 and 3.6.5.

When utilizing only the leading singular asymptotic term for CGS fringe fitting, the hope is that the CGS fringe data points that are fit lie exclusively in a region whose mechanical field is described by the K-field. Using higher order terms for fitting allows data further from the crack tip to be used in the determination of K.

LEFM asymptotic crack tip solutions are two-dimensional models. In relating fringe patterns to stress fields, CGS also makes a two-dimensional plane stress assumption. These assumptions can be expected to hold well further from the crack tip but fail as the crack tip is approached, inside the "three-dimensional zone." Rosakis and Ravi-Chandar [43] found that the two-dimensional plane stress assumption begins to fail at a radius of half the specimen thickness from the crack tip (Figure 3.5). Thus without modification CGS can only utilize data outside the three-dimensional zone and inside the region of dominance of the asymptotic term(s) used for fitting. Consequently, CGS has been successfully used only with idealized materials usually loaded in pure mode I for cracks up to initiation.

In all cases the fringe data used must result from mechanical fields whose description reasonably lies within the span of the asymptotic terms employed for fitting; otherwise baseless fitting parameters will be obtained. This condition demands first that sufficiently general crack tip solutions are employed for the analysis at hand, and second that the fringe data used for fitting is within the span of dominance of the solution terms used.

The advancements outlined in this chapter are primarily computational in nature and relate specifically to the extension of CGS to experimental studies of dynamic fracture mechanics of more difficult engineering materials. First, the CGS technique is generalized, in part by using a very general analytic asymptotic crack tip solution, to allow measurement of stress intensity factors for non-uniformly propagating dynamic mixed mode cracks moving along arbitrary paths (for example along a curved weak bond line) in homogeneous linear elastic isotropic materials. Enabling analysis of fringe patterns employing arbitrary measurement gradient direction with respect to the crack completes the generalization of the technique. A procedure is also given for rendering fringe pattern data inside the three-dimensional zone usable. Such capability is usually unnecessary for materials with more ideal properties, but for other materials it may be impossible to create analyzable fringes outside the three-dimensional zone.

Second, the development of Matlab-based code and graphical user interfaces (GUIs) is described. This package largely automates the analysis of CGS fringe patterns to obtain objective results including instantaneous crack tip location[1], which are organized and stored automatically. Without such a package, the use of the generalized fitting algorithms would be unwieldy. The GUIs allow the user to easily direct the analysis process, visualize the results, assess the quality of measurements, and verify assumptions. As a result, any reasonable CGS fringe pattern of a crack tip region can be quickly related to complex mathematical crack tip asymptotic fields to determine crack tip stress intensity factors by a person using little more than a computer mouse.

In short the advances in CGS technique described here include generality, objectivity and visual feedback organized for simplicity.

---

[1] Crack tip location is usually obscured within a shadow spot.

Following is a simple derivation of the CGS governing equation for reflection mode. Next the relationship between a general asymptotic LEFM crack tip solution and CGS fringe patterns is developed. Then the fitting process is described. Other implementation advancements are then outlined, including utilizing fringe data inside the three-dimensional zone, objectively locating the crack tip within the dark shadow spot caused by large deformations about the crack tip, and visualizing fit results. Finally a comparison of stress intensity results for different choices of fitting terms on experimental data is made to illustrate the usefulness of the analysis package.

3.2 CGS Governing Equations

Typically the CGS governing equation is derived by computing the light intensity resulting from the superposition of two perturbed light waves, one of which takes the path of zero diffraction order at the first diffraction grating and first diffraction order at the second diffraction grating, and the second wave diffracting in the opposite order. [41] (See Figures 2.10 and 2.11 for CGS setup configurations.)

A physically intuitive way to obtain the governing equation in the reflection case is to begin with Bragg's Law for diffraction intensity maxima:

$$p \sin\theta = n\lambda \tag{3.2}$$

where p is the diffraction grating pitch, θ is diffraction angle, n is diffraction order, and λ is the light wavelength.

Using basic geometry (Figure 3.1) and equation (3.2), the amount of shear accomplished by the two gratings separated by distance Δ is found to be

$$d\hat{x} = \Delta \sin\theta = \frac{\Delta n \lambda}{p} \,. \tag{3.3}$$

Thus the gratings take the laser wavefront from the specimen and produce two copies or images, which are superimposed with an offset of $d\hat{x}$. As shown in the figure, there is no small angle approximation in calculating the shear distance.

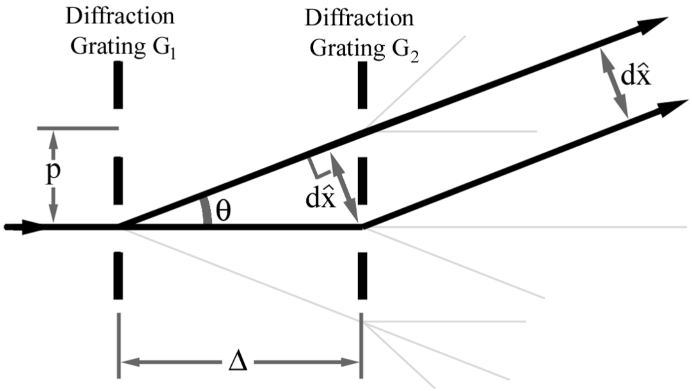

Figure 3.1: Schematic of optical shear produced by a pair of diffraction gratings.

In equation (3.3) n is chosen to be 1 to obtain the brightest possible sheared images, because any effect that can be obtained by changing n can be easily duplicated by changing grating spacing Δ. $n = 1$ is selected by using an imaging lens and aperture positioned to allow only this order of diffracted images to pass into the camera. This is the first diffraction order as viewed downstream of the lens and is composed of the superposition of one beam diffracted (first order) by the first grating and undiffracted by the second plus a second beam that passes through the first grating undiffracted and is diffracted (first order) by the second grating as shown in Figure 3.1.

Next the conditions under which the superposition of the two sheared images produces interference is examined, given that the interrogating beam is coherent. Constructive interference between the superimposed points of the two images occurs when their beam path difference is an integer multiple of the light wavelength. Since the beam is reflected off the specimen, the constructive interference condition is given by

$$2\,du_3 = m\lambda \tag{3.4}$$

where du_3 is the difference in out-of-plane displacement between the two specimen points caused to be superimposed by the shearing, and m is any integer.

Using equations (3.3) and (3.4) the desired result is obtained:

$$\frac{du_3}{d\hat{x}} = \frac{mp}{2\Delta}\,. \tag{3.5}$$

It should be noted that equation (3.5) is from finite differences but approximates a derivative well when du is small (which it generally is) and $d\hat{x}$ is small. Increasing sensitivity by increasing the two gratings' separation Δ compromises the derivative approximation and so must be chosen judiciously. This derivation does makes small angle assumptions (as do the others derivations). In particular the slight angle at which the first diffracted images passes through the second grating is ignored, and in equation (3.4) it is assumed that there is a difference in out-of-plane displacement only and no rotation of the reflecting surface, which in general is a sufficiently accurate approximation. Slight imperfections are mitigated by "nulling" out the fringe pattern by adjusting one grating to eliminate as many fringes as possible (usually all) prior to deforming the specimen.

Customarily axes are chosen with $\underset{\sim}{e}_3$ normal to the undeformed specimen surface, so $u_3 = u_3(x_1, x_2)$ so

$$\frac{\partial u_3}{\partial \hat{x}} \approx \left(\frac{mp}{2\Delta}\right), \qquad m = 0,\ \pm1,\ \pm2, \ldots \tag{3.6}$$

where $\hat{x}$ in the plane of the specimen surface ($\underset{\sim}{e}_1 - \underset{\sim}{e}_2$ plane) and is normal to the lines of the diffraction gratings, which can be placed with any orientation.

Finally, by assuming plane stress,

$$u_3 = -\frac{\nu h}{2E}(\hat{\sigma}_{11} + \hat{\sigma}_{22}) \tag{3.7}$$

where $\hat{\sigma}_{11}$ and $\hat{\sigma}_{22}$ are the thickness averages of stress, and ν and E are Poisson's ratio and Young's modulus of the specimen material respectively, and h is the specimen thickness. Using equations (3.6) and (3.7) the governing equation for reflection CGS is

$$\frac{\partial u_3}{\partial \hat{x}} = -\frac{\nu h}{2E}\frac{\partial(\hat{\sigma}_{11} + \hat{\sigma}_{22})}{\partial \hat{x}} = \left(\frac{mp}{2\Delta}\right), \qquad m = 0,\ \pm1,\ \pm2, \ldots . \tag{3.8}$$

In the interferograms m is called the *fringe order*.

For completeness and without derivation the governing equation for transmission CGS is

$$c_\alpha h \frac{\partial(\hat{\sigma}_{11} + \hat{\sigma}_{22})}{\partial \hat{x}} = \left(\frac{mp}{\Delta}\right), \qquad m = 0,\ \pm1,\ \pm2, \ldots \tag{3.9}$$

where c_α is the material Maxwell constant which is given by

$$c_\alpha = D_1 - \frac{\nu}{E}(n-1)\,. \tag{3.10}$$

Here n is the undeformed material's index of refraction and D_1 is the coefficient of the stress optical law.

As mentioned previously this two-dimensional plane stress assumption is valid for interpreting fringe data taken at least a specimen half-thickness distance from the crack tip. As the crack tip is approached, the stress state transitions from plane stress to plane strain in a complex three-dimensional manner. A procedure to render data inside this three-dimensional zone usable is given in section (3.6.3).

3.3 Crack Tip Asymptotic Equation

Using equation 3.8 or 3.9 as appropriate, CGS provides the fringe numbers (right-hand side) which are equated to the gradients of the chosen leading term(s) of the linear elastic crack tip asymptotic stress field equations (modes I and/or II) to determine their unknown coefficient(s) including the stress intensity factor. By taking advantage of the full field measuring capability of CGS, sufficient fringe data can be taken to determine the unknown coefficient(s) by a least squares fitting process. The use of higher order terms allows data beyond the region of K-dominance to be used for fitting, which not only allows more accurate determination of K but also allows the size of the K-dominated region to be examined. As the leading term of the asymptotic solution is singular, it is expected to dominate near the crack tip, and the value of its coefficient K may serve as a single parameter description of the crack tip stress state. Furthermore, the value of K observed at incipient failure may be taken as a material property, the fracture toughness.

The asymptotic stress fields are obtained by defining potentials for stress and writing the equations of motion in terms of these potentials. After assuming asymptotic expansions for these potentials, a series of differential equations is obtained in which lower asymptotic terms are coupled with higher ones. Due to the coupling, solving the differential equations for successive terms of the potential expansion is increasingly complex. Usually restrictive assumptions, such as constant crack tip velocity, are made to simplify the process by reducing the number of coefficients dependent on time or space. Liu and Rosakis [29] have made no such assumptions other than a monolithic homogeneous isotropic linear elastic material and provide the stress fields through order $r^{1/2}$ for a non-uniformly propagating dynamic crack moving along an arbitrary path under mixed mode conditions. Using these terms of the expansion with CGS in practice seems sufficient to determine K and the size of the K-dominated field given the sensitivity and field of view typically used. Also adding higher order terms in r could cause fitting problems and obfuscate the determination of K.

The mode I and mode II first stress invariants (distinguished by superscripts (I) and (II) respectively) obtained from Liu and Rosakis are

$$\begin{aligned}\frac{\hat{\sigma}_{11}^{(I)}+\hat{\sigma}_{22}^{(I)}}{\mu} &= \frac{K_I^d(t)}{\mu\sqrt{2\pi}}\frac{2(\alpha_l^2-\alpha_s^2)(1+\alpha_s^2)}{D(v)}\cos\frac{\theta_l}{2}r_l^{-1/2}+\frac{4\alpha_s(\alpha_l^2-\alpha_s^2)}{\mu D(v)}Re[A_1] \\ &\quad +Re\left\{\left[-\frac{15(\alpha_l^2-\alpha_s^2)(1+\alpha_s^2)}{2\mu D(v)}A_2+2(\alpha_l^2-\alpha_s^2)f_l+\frac{(\alpha_l^2-\alpha_s^2)(1+\alpha_l^2)}{1-\alpha_l^2}R_l\right]\cos\frac{\theta_l}{2}\right. \\ &\quad +\left[\frac{\alpha_l^2-\alpha_s^2}{4}R_l-\frac{(\alpha_l^2-\alpha_s^2)(1+\alpha_l^2)}{1-\alpha_l^2}S_l\right]\cos\frac{3\theta_l}{2} \\ &\quad \left.+\left[\frac{\alpha_l^2-\alpha_s^2}{8}S_l\right]\cos\frac{7\theta_l}{2}\right\}r_l^{1/2} \\ &\quad +O(r_{l,s})\end{aligned}\tag{3.11}$$

$$\begin{aligned}\frac{\hat{\sigma}_{11}^{(II)}+\hat{\sigma}_{22}^{(II)}}{\mu} &= -\frac{K_{II}^d(t)}{\mu\sqrt{2\pi}}\frac{4\alpha_s(\alpha_l^2-\alpha_s^2)}{D(v)}\sin\frac{\theta_l}{2}r_l^{-1/2} \\ &\quad +Im\left\{\left[-\frac{15\alpha_s(\alpha_l^2-\alpha_s^2)}{\mu D(v)}A_2-2(\alpha_l^2-\alpha_s^2)f_l-\frac{(\alpha_l^2-\alpha_s^2)(1+\alpha_l^2)}{1-\alpha_l^2}R_l\right]\sin\frac{\theta_l}{2}\right. \\ &\quad +\left[\frac{\alpha_l^2-\alpha_s^2}{4}R_l-\frac{(\alpha_l^2-\alpha_s^2)(1+\alpha_l^2)}{1-\alpha_l^2}S_l\right]\sin\frac{3\theta_l}{2} \\ &\quad \left.+\left[\frac{\alpha_l^2-\alpha_s^2}{8}S_l\right]\sin\frac{7\theta_l}{2}\right\}r_l^{1/2} \\ &\quad +O(r_{l,s})\;.\end{aligned}\tag{3.12}$$

In the above equations, the dependence of all variables (except μ, the shear modulus) on time t is omitted for clarity. $K_I^d(t)$ and $K_{II}^d(t)$ are the desired leading term coefficients or stress intensity factors for modes I and II respectively. $A_1(t)$ and $A_2(t)$ are the unknown coefficients of the next terms[2] of the asymptotic expansion. The rest of the terms are defined as follows:

$$r_{l,s} = \left(x_1^2 + (\alpha_{l,s}x_2)^2\right)^{1/2} \tag{3.13}$$

$$\theta_{l,s} = tan^{-1}\left[\frac{\alpha_{l,s}x_2}{x_1}\right] \tag{3.14}$$

$$\alpha_{l,s}(t) = \left(1 - \frac{v^2(t)}{c_{l,s}^2}\right)^{1/2} \tag{3.15}$$

$$D(v) = 4\alpha_l\alpha_s - \left(1+\alpha_s^2\right)^2 \tag{3.16}$$

$$\overset{*}{D}(v) = 4\alpha_l\alpha_s + \left(1+\alpha_s^2\right)^2 \tag{3.17}$$

$$m_l(t) = \frac{1}{2}\left\{(1-\alpha_s^2) - \frac{2(\alpha_l^2-\alpha_s^2)}{1-\alpha_l^2}\right\} \tag{3.18}$$

$$m_s(t) = \frac{1}{2}\left\{1-\alpha_s^2\right\} \tag{3.19}$$

where $v(t)$ is crack tip velocity, $k(t)$ is instantaneous curvature of crack tip trajectory, and c_l and c_s are the material's longitudinal and shear wave speed respectively. Also

$$\begin{aligned} f_l(t) = {} & \left(\frac{(1+\alpha_s^2)m_l}{D(v)} - \frac{1}{8}\right)R_l(t) - \left(\frac{(1+\alpha_s^2)m_l}{D(v)} + \frac{\overset{*}{D}(v)}{D(v)} + \frac{9}{16}\right)S_l(t) \\ & -\frac{2\alpha_s m_s}{D(v)}R_s(t) + \left(\frac{2\alpha_s m_s}{D(v)} + \frac{2\alpha_s(1+\alpha_s^2)}{D(v)}\right)S_s(t) \end{aligned} \tag{3.20}$$

$$\begin{aligned} S_l(t) = {} & \left\{\frac{v^2(1+\alpha_s^2)}{\mu\sqrt{2\pi}D(v)\alpha_l^4c_l^4}K_I^d(t)\dot{v}(t) + \frac{2\alpha_s(1-\alpha_l^2)^2}{\mu\sqrt{2\pi}D(v)\alpha_l^3}K_{II}^d(t)k(t)\right\} \\ & -i\left\{\frac{2v^2\alpha_s}{\mu\sqrt{2\pi}D(v)\alpha_l^4c_l^4}K_{II}^d(t)\dot{v}(t) + \frac{(1-\alpha_s^2)(1-\alpha_l^2)^2}{\mu\sqrt{2\pi}D(v)\alpha_l^3}K_I^d(t)k(t)\right\} \end{aligned} \tag{3.21}$$

$$\begin{aligned} S_s(t) = {} & -\left\{\frac{2v^2\alpha_l}{\mu\sqrt{2\pi}D(v)\alpha_s^4c_s^4}K_I^d(t)\dot{v}(t) + \frac{(1+\alpha_s^2)(1-\alpha_s^2)^2}{\mu\sqrt{2\pi}D(v)\alpha_s^3}K_{II}^d(t)k(t)\right\} \\ & +i\left\{\frac{v^2(1+\alpha_s^2)}{\mu\sqrt{2\pi}D(v)\alpha_s^4c_s^4}K_{II}^d(t)\dot{v}(t) - \frac{2\alpha_l(1-\alpha_s^2)^2}{\mu\sqrt{2\pi}D(v)\alpha_s^3}K_I^d(t)k(t)\right\} \end{aligned} \tag{3.22}$$

---

[2] CGS is insensitive to T stress, or the term of order r^0

$$\begin{aligned} R_l(t) &= -\frac{1}{\mu\sqrt{2\pi}}\left\{\frac{4\sqrt{v}}{\alpha_l^2 c_l^2}\frac{d}{dt}\left[\frac{\sqrt{v}(1+\alpha_s^2)}{D(v)}K_I^d(t)\right] - \frac{v^2(1+\alpha_s^2)}{D(v)\alpha_l^4 c_l^4}K_I^d(t)\dot{v}(t)\right. \\ &\quad \left. - \frac{2\alpha_s(1-\alpha_l^2)(1+3\alpha_l^2)}{D(v)\alpha_l^3}K_{II}^d(t)k(t)\right\} \\ &\quad +i\frac{1}{\mu\sqrt{2\pi}}\left\{\frac{8\sqrt{v}}{\alpha_l^2 c_l^2}\frac{d}{dt}\left[\frac{\sqrt{v}\alpha_s}{D(v)}K_{II}^d(t)\right] - \frac{2v^2\alpha_s}{D(v)\alpha_l^4 c_l^4}K_{II}^d(t)\dot{v}(t)\right. \\ &\quad \left. + \frac{(1+\alpha_s^2)(1-\alpha_l^2)(1+3\alpha_l^2)}{D(v)\alpha_l^3}K_I^d(t)k(t)\right\} \end{aligned} \tag{3.23}$$

$$\begin{aligned} R_s(t) &= \frac{1}{\mu\sqrt{2\pi}}\left\{\frac{8\sqrt{v}}{\alpha_s^2 c_s^2}\frac{d}{dt}\left[\frac{\sqrt{v}\alpha_l}{D(v)}K_I^d(t)\right] - \frac{2v^2\alpha_l}{D(v)\alpha_s^4 c_s^4}K_I^d(t)\dot{v}(t)\right. \\ &\quad \left. - \frac{(1+\alpha_s^2)(1-\alpha_s^2)(1+3\alpha_s^2)}{D(v)\alpha_s^3}K_{II}^d(t)k(t)\right\} \\ &\quad -i\frac{1}{\mu\sqrt{2\pi}}\left\{\frac{4\sqrt{v}}{\alpha_s^2 c_s^2}\frac{d}{dt}\left[\frac{\sqrt{v}(1+\alpha_s^2)}{D(v)}K_{II}^d(t)\right] - \frac{v^2(1+\alpha_s^2)}{D(v)\alpha_s^4 c_s^4}K_{II}^d(t)\dot{v}(t)\right. \\ &\quad \left. + \frac{2\alpha_l(1-\alpha_s^2)(1+3\alpha_s^2)}{D(v)\alpha_s^3}K_I^d(t)k(t)\right\} \end{aligned} \tag{3.24}$$

where $\dot{v}$ is the crack tip acceleration. Note that having crack trajectory curvature $k(t)$ couples K_I^d and K_{II}^d.

The equations (3.20–3.24) are highly dependent on crack tip velocity and acceleration which are very difficult to determine, hence the bracketed quantities $[\ldots]$ in equation (3.11) are replaced with variables η_1, η_2, η_3, and η_4, giving

$$\begin{aligned} \hat{\sigma}_{11}^{(I)} + \hat{\sigma}_{22}^{(I)} &= \frac{K_I^d(t)}{\sqrt{2\pi}}\frac{2(\alpha_l^2-\alpha_s^2)(1+\alpha_s^2)}{D(v)}\cos\frac{\theta_l}{2}r_l^{-1/2} + \frac{4\alpha_s(\alpha_l^2-\alpha_s^2)}{D(v)}Re[A_1] \\ &\quad +Re\left\{\eta_1\cos\frac{\theta_l}{2} + \eta_2\cos\frac{3\theta_l}{2} + \eta_3\cos\frac{7\theta_l}{2}\right\}r_l^{1/2} \\ &\quad +O(r_{l,s}) \end{aligned} \tag{3.25}$$

$$\begin{aligned} \hat{\sigma}_{11}^{(II)} + \hat{\sigma}_{22}^{(II)} &= -\frac{K_{II}^d(t)}{\sqrt{2\pi}}\frac{4\alpha_s(\alpha_l^2-\alpha_s^2)}{D(v)}\sin\frac{\theta_l}{2}r_l^{-1/2} \\ &\quad +Im\left\{\eta_4\sin\frac{\theta_l}{2} + \eta_2\sin\frac{3\theta_l}{2} + \eta_3\sin\frac{7\theta_l}{2}\right\}r_l^{1/2} \\ &\quad +O(r_{l,s})\,. \end{aligned} \tag{3.26}$$

Note that η_1 and η_4 are functions of the unknown asymptotic coefficient $A_2(t)$, but η_2 and η_3 are functions of $v(t)$, $\dot{v}(t)$, $K_I^d(t)$, $K_{II}^d(t)$, $\dot{K}_I^d(t)$, $\dot{K}_{II}^d(t)$, and $k(t)$ only—all local quantities in theory measurable or to be fit.

3.4 Interpretation of CGS Fringe Patterns

Given the asymptotic terms obtained in the previous section, the next step is to determine the stress intensity factors $K_I^d(t)$ and $K_{II}^d(t)$ using CGS. The conventional crack tip axis system is employed (Figure 2.3).

Extending the procedure of Rosakis [41] let

$$Y^d_{\alpha\beta}(r_l,\theta_l,t)=\frac{\partial(\hat{\sigma}^{(\beta)}_{11}+\hat{\sigma}^{(\beta)}_{22})}{\partial x_\alpha}\frac{S_{\alpha\beta}}{F_\beta(v)}\frac{2\sqrt{2\pi}r_l^{3/2}}{(\delta_{\alpha\beta}\cos(3\theta_l/2)+(1-\delta_{\alpha\beta})\sin(3\theta_l/2))} \tag{3.27}$$

where $\hat{\sigma}$ the thickness average of stress, $\beta=1$ for mode I (symmetric deformation) and $\beta=2$ for mode II (asymmetric deformation), α indicates the direction of the spatial derivative, $\delta_{\alpha\beta}$ is the Kronecker delta, α and β have the range $\{1,2\}$, and

$$S_{\alpha\beta} = \begin{cases} -1 & \text{for } \alpha=\beta=1 \\ 1 & \text{for } \alpha=1 \text{ and } \beta=2 \\ -1/\alpha_l & \text{for } \alpha=2 \end{cases} \tag{3.28}$$

$$F_\beta(v) = \begin{cases} \frac{2(1+\alpha_s^2)(\alpha_l^2-\alpha_s^2)}{D(v)} & \text{for } \beta=1 \\ \\ \frac{4\alpha_s(\alpha_l^2-\alpha_s^2)}{D(v)} & \text{for } \beta=2\,. \end{cases} \tag{3.29}$$

It should be noted that $F_\beta \to 2$ as $v\to 0$.

The significance of $Y^d_{\alpha\beta}(r_l,\theta_l,t)$ is that for data inside a region both in plane strain and dominated by K^d_β

$$K^d_\beta(t)=Y^d_{\beta\alpha}(r_l,\theta_l,t)\,. \tag{3.30}$$

Also,

$$Y^d_{\alpha\beta}(r_l,\theta_l,t)=\Big(\frac{mp}{\Delta ch}\Big)\frac{S_{\alpha\beta}}{F_\beta}\frac{2\sqrt{2\pi}r_l^{3/2}}{(\delta_{\alpha\beta}\cos(3\theta_l/2)+(1-\delta_{\alpha\beta})\sin(3\theta_l/2))} \tag{3.31}$$

using the CGS interference condition

$$\frac{\partial(\hat{\sigma}_{11}+\hat{\sigma}_{22})}{\partial x_\alpha}\approx\frac{mp}{\Delta ch} \tag{3.32}$$

where

$$c = \begin{cases} D_1 - \nu/E(n-1) = c_\sigma & \text{for transmission} \\ -\nu/E & \text{for reflection}\,. \end{cases} \tag{3.33}$$

First consider derivatives in the x_1 direction ($\alpha = 1$). The definitions of r_l and θ_l from equations (3.13, 3.14) are substituted into the first stress invariant equations (3.25, 3.26) and then the partial derivative with respect to x_1 is taken:

$$\begin{aligned} \frac{\partial(\hat{\sigma}_{11}^{(I)} + \hat{\sigma}_{22}^{(I)})}{\partial x_1} &= -K_I^d(t)\frac{F_I(v)}{2\sqrt{2\pi}}\frac{\cos\frac{3\theta_l}{2}}{r_l^{3/2}} \\ &+Re\left\{\left[\frac{\eta_1 + 2\eta_2}{2}\right]\cos\frac{\theta_l}{2} + \left[\frac{-\eta_2 + 4\eta_3}{2}\right]\cos\frac{5\theta_l}{2} + \left[-\frac{3\eta_3}{2}\right]\cos\frac{9\theta_l}{2}\right\}\frac{1}{r_l^{1/2}} \\ &+O(1) \end{aligned} \tag{3.34}$$

$$\begin{aligned} \frac{\partial(\hat{\sigma}_{11}^{(II)} + \hat{\sigma}_{22}^{(II)})}{\partial x_1} &= K_{II}^d(t)\frac{F_{II}(v)}{2\sqrt{2\pi}}\frac{\sin\frac{3\theta_l}{2}}{r_l^{3/2}} \\ &+Im\left\{\left[\frac{-\eta_4 + 2\eta_2}{2}\right]\sin\frac{\theta_l}{2} + \left[\frac{-\eta_2 + 4\eta_3}{2}\right]\sin\frac{5\theta_l}{2} + \left[-\frac{3\eta_3}{2}\right]\sin\frac{9\theta_l}{2}\right\}\frac{1}{r_l^{1/2}} \\ &+O(1)\,. \end{aligned} \tag{3.35}$$

For mode I, substituting equation (3.34) into equation (3.27) and noting equation (3.31) produces

$$\begin{aligned} Y_{11}^d(r_l, \theta_l, t) &= K_I^d(t) + \left\{\beta_2^{(I)}\frac{\cos(\theta_l/2)}{\cos(3\theta_l/2)} + \beta_3^{(I)}\frac{\cos(5\theta_l/2)}{\cos(3\theta_l/2)} + \beta_4^{(I)}\frac{\cos(9\theta_l/2)}{\cos(3\theta_l/2)}\right\} r_l \\ &+O(r^{3/2}) \\ &= \left(\frac{mp}{\Delta ch}\right)\frac{-1}{F_I(v)}\frac{2\sqrt{2\pi}r_l^{3/2}}{\cos(3\theta_l/2)} \end{aligned} \tag{3.36}$$

where

$$\begin{aligned}
\beta_2^{(I)} &= -\frac{2\sqrt{2\pi}}{F_I(v)} Re\left[\frac{\eta_1 + 2\eta_2}{2}\right] \qquad (3.37)\\
&= \frac{15\sqrt{2\pi}}{4} Re[A_2(t)] - \frac{2\sqrt{2\pi}\mu}{F_I(v)}(\alpha_l^2 - \alpha_s^2)\left[\frac{3+\alpha_l^2}{4(1-\alpha_l^2)} Re[R_l(t)] - \frac{1+\alpha_l^2}{1-\alpha_l^2} Re[S_l(t)] + Re[f_l(t)]\right]
\end{aligned}$$

$$\beta_3^{(I)} = -\frac{2\sqrt{2\pi}}{F_I(v)} Re\left[\frac{-\eta_2 + 4\eta_3}{2}\right] = \frac{\sqrt{2\pi}\mu}{2F_I(v)}(\alpha_l^2 - \alpha_s^2)\left[\frac{1}{2} Re[R_l(t)] - \frac{3+\alpha_l^2}{1-\alpha_l^2} Re[S_l(t)]\right] \qquad (3.38)$$

$$\beta_4^{(I)} = -\frac{2\sqrt{2\pi}}{F_I(v)} Re\left[-\frac{3\eta_3}{2}\right] = \frac{3\sqrt{2\pi}\mu}{8F_I(v)}(\alpha_l^2 - \alpha_s^2) Re[S_l(t)]\,. \qquad (3.39)$$

Similarly using equation (3.35) with equation (3.27) for mode II gives

$$\begin{aligned}
Y_{21}^d(r_l, \theta_l, t) &= K_{II}^d(t) + \left\{\beta_2^{(II)} \frac{\sin(\theta_l/2)}{\sin(3\theta_l/2)} + \beta_3^{(II)} \frac{\sin(5\theta_l/2)}{\sin(3\theta_l/2)} + \beta_4^{(II)} \frac{\sin(9\theta_l/2)}{\sin(3\theta_l/2)}\right\} r_l \qquad (3.40)\\
&\quad + O(r^{3/2})\\
&= \left(\frac{mp}{\Delta ch}\right) \frac{1}{F_{II}(v)} \frac{2\sqrt{2\pi} r_l^{3/2}}{\sin(3\theta_l/2)}
\end{aligned}$$

where

$$\begin{aligned}
\beta_2^{(II)} &= \frac{2\sqrt{2\pi}}{F_{II}(v)} Im\left[\frac{-\eta_4 + 2\eta_2}{2}\right] \qquad (3.41)\\
&= \frac{15\sqrt{2\pi}}{4} Im[A_2(t)]\\
&\quad + \frac{2\sqrt{2\pi}\mu}{F_{II}(v)}(\alpha_l^2 - \alpha_s^2)\left[\frac{3+\alpha_l^2}{4(1-\alpha_l^2)} Im[R_l(t)] - \frac{1+\alpha_l^2}{1-\alpha_l^2} Im[S_l(t)] + Im[f_l(t)]\right]
\end{aligned}$$

$$\begin{aligned}
\beta_3^{(II)} &= \frac{2\sqrt{2\pi}}{F_{II}(v)} Im\left[\frac{-\eta_2 + 4\eta_3}{2}\right] \qquad (3.42)\\
&= -\frac{\sqrt{2\pi}\mu}{2F_{II}(v)}(\alpha_l^2 - \alpha_s^2)\left[\frac{1}{2} Im[R_l(t)] - \frac{3+\alpha_l^2}{1-\alpha_l^2} Im[S_l(t)]\right]
\end{aligned}$$

$$\beta_4^{(II)} = \frac{2\sqrt{2\pi}}{F_{II}(v)} Im\left[-\frac{3\eta_3}{2}\right] = -\frac{3\sqrt{2\pi}\mu}{8F_{II}(v)}(\alpha_l^2 - \alpha_s^2) Im[S_l(t)]\,. \qquad (3.43)$$

All β are functions of time. $\beta_2^{(I)}$ and $\beta_2^{(II)}$ are functions of the real and imaginary part of unknown asymptotic coefficient $A_2(t)$. However β_3 and β_4 are functions of $v(t)$, $\dot{v}(t)$, $K_I^d(t)$,$\dot{K}_I^d(t)$,

$K^d_{II}(t)$,$\dot{K}^d_{II}(t)$, and $k(t)$ only—again locally determined quantities[3]. Due to measurement error it seems best to treat all β as variables for fitting and then check for consistency later if desired. In some cases β equations simplify greatly. For example, for a stationary crack ($v = 0$), $S_l = S_s = R_l = R_s = f_l = 0$ leaving $\beta_2 = 15\sqrt{2\pi}A_2/4$ and $\beta_3 = \beta_4 = 0$.

Now partial derivatives in the x_2 direction ($\alpha = 2$) are considered.

$$\begin{aligned}\frac{\partial(\hat{\sigma}^{(I)}_{11} + \hat{\sigma}^{(I)}_{22})}{\partial x_2} &= -\alpha_l K^d_I(t)\frac{F_I(v)}{2\sqrt{2\pi}}\frac{\sin\frac{3\theta_l}{2}}{r_l^{3/2}} \\ &+\alpha_l Re\left\{\left[\frac{\eta_1 - 2\eta_2}{2}\right]\sin\frac{\theta_l}{2} + \left[-\frac{\eta_2 + 4\eta_3}{2}\right]\sin\frac{5\theta_l}{2} + \left[-\frac{3\eta_3}{2}\right]\sin\frac{9\theta_l}{2}\right\}\frac{1}{r_l^{1/2}} \\ &+O(1)\end{aligned} \tag{3.44}$$

$$\begin{aligned}\frac{\partial(\hat{\sigma}^{(II)}_{11} + \hat{\sigma}^{(II)}_{22})}{\partial x_2} &= -\alpha_l K^d_{II}(t)\frac{F_{II}(v)}{2\sqrt{2\pi}}\frac{\cos\frac{3\theta_l}{2}}{r_l^{3/2}} \\ &+\alpha_l Im\left\{\left[\frac{\eta_4 + 2\eta_2}{2}\right]\cos\frac{\theta_l}{2} + \left[\frac{\eta_2 + 4\eta_3}{2}\right]\cos\frac{5\theta_l}{2} + \left[\frac{3\eta_3}{2}\right]\cos\frac{9\theta_l}{2}\right\}\frac{\alpha_l}{r_l^{1/2}} \\ &+O(1)\ .\end{aligned} \tag{3.45}$$

Substituting equation (3.44) into equation (3.27) gives the desired result for mode I:

$$\begin{aligned}Y^d_{12}(r_l, \theta_l, t) &= K^d_I(t) + \left\{\gamma^{(I)}_2\frac{\sin(\theta_l/2)}{\sin(3\theta_l/2)} + \gamma^{(I)}_3\frac{\sin(5\theta_l/2)}{\sin(3\theta_l/2)} + \gamma^{(I)}_4\frac{\sin(9\theta_l/2)}{\sin(3\theta_l/2)}\right\} r_l \\ &+O(r^{3/2}) \\ &= \left(\frac{mp}{\Delta ch}\right)\frac{-1}{\alpha_l F_I(v)}\frac{2\sqrt{2\pi}r_l^{3/2}}{\sin(3\theta_l/2)}\end{aligned} \tag{3.46}$$

---

[3] The unknown asymptotic coefficients depend on far field boundary conditions.

where

$$\begin{aligned}\gamma_2^{(I)} &= -\frac{2\sqrt{2\pi}}{F_I(v)}Re\left[\frac{\eta_1-2\eta_2}{2}\right] = \beta_2^{(I)} + 4\beta_3^{(I)} + \frac{16}{3}\beta_4^{(I)} \\ &= \frac{15\sqrt{2\pi}}{4}Re[A_2(t)] - \frac{2\sqrt{2\pi}\mu}{F_I(v)}(\alpha_l^2-\alpha_s^2)\left[\frac{1+3\alpha_l^2}{4(1-\alpha_l^2)}Re[R_l(t)] + \frac{1+\alpha_l^2}{1-\alpha_l^2}Re[S_l(t)] + Re[f_l(t)]\right]\end{aligned} \tag{3.47}$$

$$\begin{aligned}\gamma_3^{(I)} &= -\frac{2\sqrt{2\pi}}{F_I(v)}Re\left[-\frac{\eta_2+4\eta_3}{2}\right] = \frac{\sqrt{2\pi}\mu}{2F_I(v)}(\alpha_l^2-\alpha_s^2)\left[\frac{1}{2}Re[R_l(t)] - \frac{3+\alpha_l^2}{1-\alpha_l^2}Re[S_l(t)]\right] \\ &= \beta_3^{(I)} + \frac{8}{3}\beta_4^{(I)}\end{aligned} \tag{3.48}$$

$$\gamma_4^{(I)} = -\frac{2\sqrt{2\pi}}{F_I(v)}Re\left[-\frac{3\eta_3}{2}\right] = \frac{3\sqrt{2\pi}\mu}{8F_I(v)}(\alpha_l^2-\alpha_s^2)Re[S_l(t)] = \beta_4^{(I)} \tag{3.49}$$

and for mode II:

$$\begin{aligned}Y_{22}^d(r_l,\theta_l,t) &= K_{II}^d(t) + \left\{\gamma_2^{(II)}\frac{\cos(\theta_l/2)}{\cos(3\theta_l/2)} + \gamma_3^{(II)}\frac{\cos(5\theta_l/2)}{\cos(3\theta_l/2)} + \gamma_4^{(II)}\frac{\cos(9\theta_l/2)}{\cos(3\theta_l/2)}\right\}r_l \\ &\quad +O(r^{3/2}) \\ &= \left(\frac{mp}{\Delta ch}\right)\frac{-1}{\alpha_l F_{II}(v)}\frac{2\sqrt{2\pi}r_l^{3/2}}{\cos(3\theta_l/2)}\end{aligned} \tag{3.50}$$

where

$$\begin{aligned}
\gamma_2^{(II)} &= -\frac{2\sqrt{2\pi}}{F_{II}(v)} Im\left[\frac{\eta_4 + 2\eta_2}{2}\right] \\
&= \beta_2^{(II)} + 4\beta_3^{(II)} + \frac{16}{3}\beta_4^{(II)} \\
&= \frac{15\sqrt{2\pi}}{4} Im[A_2(t)] \\
&\quad + \frac{2\sqrt{2\pi}\mu}{F_{II}(v)}(\alpha_l^2 - \alpha_s^2)\left[\frac{1+3\alpha_l^2}{4(1-\alpha_l^2)} Im[R_l(t)] + \frac{1+\alpha_l^2}{1-\alpha_l^2} Im[S_l(t)] + Im[f_l(t)]\right]
\end{aligned} \tag{3.51}$$

$$\begin{aligned}
\gamma_3^{(II)} &= -\frac{2\sqrt{2\pi}}{F_{II}(v)} Im\left[\frac{\eta_2 + 4\eta_3}{2}\right] \\
&= -\frac{\sqrt{2\pi}\mu}{2F_{II}(v)}(\alpha_l^2 - \alpha_s^2)\left[\frac{1}{2} Im[R_l(t)] - \frac{1+3\alpha_l^2}{1-\alpha_l^2} Im[S_l(t)]\right] \\
&= \beta_3^{(II)} + \frac{8}{3}\beta_4^{(II)}
\end{aligned} \tag{3.52}$$

$$\gamma_4^{(II)} = -\frac{2\sqrt{2\pi}}{F_{II}(v)} Im\left[\frac{3\eta_3}{2}\right] = -\frac{3\sqrt{2\pi}\mu}{8F_{II}(v)}(\alpha_l^2 - \alpha_s^2) Im[S_l(t)] = \beta_4^{(II)}\,. \tag{3.53}$$

Revisiting equations (3.25, 3.26),

$$Re\,[\eta_1] = -\frac{F_I(v)}{\sqrt{2\pi}}\left[\beta_2^{(I)} + 2\beta_3^{(I)} + \frac{8}{3}\beta_4^{(I)}\right] \tag{3.54}$$

$$Re\,[\eta_2] = \frac{F_I(v)}{\sqrt{2\pi}}\left[\beta_3^{(I)} + \frac{4}{3}\beta_4^{(I)}\right] \tag{3.55}$$

$$Re\,[\eta_3] = \frac{F_I(v)}{3\sqrt{2\pi}}\beta_4^{(I)} \tag{3.56}$$

$$Im\,[\eta_4] = -\frac{F_{II}(v)}{\sqrt{2\pi}}\left[\beta_2^{(II)} + 2\beta_3^{(II)} + \frac{8}{3}\beta_4^{(II)}\right] \tag{3.57}$$

$$Im\,[\eta_2] = -\frac{F_{II}(v)}{\sqrt{2\pi}}\left[\beta_3^{(II)} + \frac{4}{3}\beta_4^{(II)}\right] \tag{3.58}$$

$$Im\,[\eta_3] = -\frac{F_{II}(v)}{3\sqrt{2\pi}}\beta_4^{(II)}\,. \tag{3.59}$$

3.5 Fitting Data

The goal is to determine $K_I^d(t)$ and $K_{II}^d(t)$ from analysis of CGS fringe patterns under conditions for which higher order terms cannot be neglected. Specifically it is desirable to determine fundamental fracture parameters for any loading history and crack trajectory as measured using arbitrary grating orientation. Arbitrary grating orientation is especially essential for cases where crack orientation changes with time, i. e., for curving or branching cracks. Otherwise adding this degree of freedom minimizes fitting error in cases where the gradients are not precisely in the $\underset{\sim}{e}_1$ or $\underset{\sim}{e}_2$ direction with respect to the crack due to misalignment or slight material anisotropy. The usual crack tip coordinates (Figure 2.3) are employed with the origin located at the crack tip and $\underset{\sim}{e}_1$ and $\underset{\sim}{e}_2$ tangential and normal to the crack plane respectively. The direction of the CGS measurement gradient is in the $\underset{\sim}{\hat{e}}$ direction which lies in the specimen surface plane. Let ϕ be the angle of $\underset{\sim}{\hat{e}}$ with respect to the crack tip coordinates. Using the chain rule,

$$\begin{aligned}
\frac{\partial(\hat{\sigma}_{11}+\hat{\sigma}_{22})}{\partial \hat{x}} &= \frac{\partial(\hat{\sigma}_{11}+\hat{\sigma}_{22})}{\partial x_1}\frac{\partial x_1}{\partial \hat{x}} + \frac{\partial(\hat{\sigma}_{11}+\hat{\sigma}_{22})}{\partial x_2}\frac{\partial x_2}{\partial \hat{x}} \\
&= \cos\phi\left[\frac{\partial(\hat{\sigma}^{(I)}_{11}+\hat{\sigma}^{(I)}_{22})}{\partial x_1} + \frac{\partial(\hat{\sigma}^{(II)}_{11}+\hat{\sigma}^{(II)}_{22})}{\partial x_1}\right] \\
&\quad + \sin\phi\left[\frac{\partial(\hat{\sigma}^{(I)}_{11}+\hat{\sigma}^{(I)}_{22})}{\partial x_2} + \frac{\partial(\hat{\sigma}^{(II)}_{11}+\hat{\sigma}^{(II)}_{22})}{\partial x_2}\right] \\
&= \frac{mp}{\Delta ch}\,.
\end{aligned} \tag{3.60}$$

Now the stress derivatives given in equations (3.34, 3.35, 3.44, and 3.45) are used to obtain the following:

$$\begin{aligned}
\frac{mp}{\Delta ch} &= -K^d_I \frac{F_I(v)}{2\sqrt{2\pi}\, r_l^{3/2}}\left[\cos\phi\cos\frac{3\theta_l}{2} + \alpha_l\sin\phi\sin\frac{3\theta_l}{2}\right] \\
&+ \frac{1}{2\sqrt{r_l}}\left\{Re[\eta_1]\left[\cos\phi\cos\frac{\theta_l}{2} + \alpha_l\sin\phi\sin\frac{\theta_l}{2}\right]\right. \\
&+ Re[\eta_2]\left[\cos\phi\left(2\cos\frac{\theta_l}{2} - \cos\frac{5\theta_l}{2}\right) - \alpha_l\sin\phi\left(2\sin\frac{\theta_l}{2} + \sin\frac{5\theta_l}{2}\right)\right] \\
&+ \left. Re[\eta_3]\left[\cos\phi\left(4\cos\frac{5\theta_l}{2} - 3\cos\frac{9\theta_l}{2}\right) - \alpha_l\sin\phi\left(4\sin\frac{5\theta_l}{2} + 3\sin\frac{9\theta_l}{2}\right)\right]\right\} \\
&+ K^d_{II}\frac{F_{II}(v)}{2\sqrt{2\pi}\, r_l^{3/2}}\left[\cos\phi\sin\frac{3\theta_l}{2} - \alpha_l\sin\phi\cos\frac{3\theta_l}{2}\right] \\
&+ \frac{1}{2\sqrt{r_l}}\left\{Im[\eta_4]\left[-\cos\phi\sin\frac{\theta_l}{2} + \alpha_l\sin\phi\cos\frac{\theta_l}{2}\right]\right. \\
&+ Im[\eta_2]\left[\cos\phi\left(2\sin\frac{\theta_l}{2} - \sin\frac{5\theta_l}{2}\right) + \alpha_l\sin\phi\left(2\cos\frac{\theta_l}{2} + \cos\frac{5\theta_l}{2}\right)\right] \\
&+ \left. Im[\eta_3]\left[\cos\phi\left(4\sin\frac{5\theta_l}{2} - 3\sin\frac{9\theta_l}{2}\right) + \alpha_l\sin\phi\left(4\cos\frac{5\theta_l}{2} + 3\cos\frac{9\theta_l}{2}\right)\right]\right\}\,.
\end{aligned} \tag{3.61}$$

A least-squares fitting method is utilized to obtain the unknowns from CGS data points. $\underset{\sim}{x} = \hat{\underset{\sim}{L}}\underset{\sim}{b}$ is the least squares solution for $\underset{\sim}{A}\underset{\sim}{x} = \underset{\sim}{b}$ where $\hat{\underset{\sim}{L}} = (\underset{\sim}{A}^T\underset{\sim}{A})^{-1}\underset{\sim}{A}^T$. In this case the components of $\underset{\sim}{A}$ are $a_{ij} = f_j(r_{li}, \theta_{li})$, $\underset{\sim}{x} = [K^d_I, Re[\eta_1], Re[\eta_2], Re[\eta_3], K^d_{II}, Im[\eta_4], Im[\eta_2], Im[\eta_3]]^T$, and $b_i = (m_i\, p)/(\Delta\, c\, h)$. The subscript i with r_l and θ_l refer to the values of r_l and θ_l for data point i. The functions $f_j(r_{li},\theta_{li})$ are given by the following:

$$f_1(r_{li},\theta_{li}) = -\frac{F_I(v)}{2\sqrt{2\pi}\,r_{li}^{3/2}}\left[\cos\phi\cos\frac{3\theta_{li}}{2}+\alpha_l\sin\phi\sin\frac{3\theta_{li}}{2}\right] \tag{3.62}$$

$$f_2(r_{li},\theta_{li}) = \frac{1}{2\sqrt{r_{li}}}\left[\cos\phi\cos\frac{\theta_{li}}{2}+\alpha_l\sin\phi\sin\frac{\theta_{li}}{2}\right] \tag{3.63}$$

$$f_3(r_{li},\theta_{li}) = \frac{1}{2\sqrt{r_{li}}}\left[\cos\phi\left(2\cos\frac{\theta_{li}}{2}-\cos\frac{5\theta_{li}}{2}\right)-\alpha_l\sin\phi\left(2\sin\frac{\theta_{li}}{2}+\sin\frac{5\theta_{li}}{2}\right)\right] \tag{3.64}$$

$$f_4(r_{li},\theta_{li}) = \frac{1}{2\sqrt{r_{li}}}\left[\cos\phi\left(4\cos\frac{5\theta_{li}}{2}-3\cos\frac{9\theta_{li}}{2}\right)-\alpha_l\sin\phi\left(4\sin\frac{5\theta_{li}}{2}+3\sin\frac{9\theta_{li}}{2}\right)\right] \tag{3.65}$$

$$f_5(r_{li},\theta_{li}) = \frac{F_{II}(v)}{2\sqrt{2\pi}\,r_{li}^{3/2}}\left[\cos\phi\sin\frac{3\theta_{li}}{2}-\alpha_l\sin\phi\cos\frac{3\theta_{li}}{2}\right] \tag{3.66}$$

$$f_6(r_{li},\theta_{li}) = \frac{1}{2\sqrt{r_{li}}}\left[-\cos\phi\sin\frac{\theta_{li}}{2}+\alpha_l\sin\phi\cos\frac{\theta_{li}}{2}\right] \tag{3.67}$$

$$f_7(r_{li},\theta_{li}) = \frac{1}{2\sqrt{r_{li}}}\left[\cos\phi\left(2\sin\frac{\theta_{li}}{2}-\sin\frac{5\theta_{li}}{2}\right)+\alpha_l\sin\phi\left(2\cos\frac{\theta_{li}}{2}+\cos\frac{5\theta_{li}}{2}\right)\right] \tag{3.68}$$

$$f_8(r_{li},\theta_{li}) = \frac{1}{2\sqrt{r_{li}}}\left[\cos\phi\left(4\sin\frac{5\theta_{li}}{2}-3\sin\frac{9\theta_{li}}{2}\right)+\alpha_l\sin\phi\left(4\cos\frac{5\theta_{li}}{2}+3\cos\frac{9\theta_{li}}{2}\right)\right] \tag{3.69}$$

3.6 Implementation in Matlab

3.6.1 Matlab Implementation Overview

Matlab is a very functional language for creating analysis packages. Its most useful features are its ability to work with images, plots, and matrices with syntax allowing modular construction and relatively easy debugging, and its facilities for creating custom graphical user interfaces (GUIs). By creating GUIs, one can organize input and operations in a way that greatly simplifies use and obscures unnecessary details.

Matlab GUIs were created to facilitate analysis of CGS fringe patterns using the equations described in the previous section. Without such organization, implementation would be daunting at best, if not highly prone to error. The ability to use more general equations with arbitrary gradient direction as outlined above is a significant though complex improvement. The additions incorporated into a Matlab package described in this section allow analysis of any crack propagating along any path at any rate under any in-plane loading history to be successfully analyzed so long as the material fracture is described by LEFM. A complete package of tools has been assembled in Matlab with GUIs developed to add insight, ease of use, and minimize measurement subjectivity. A description of the analysis process and package features follows, including digitizing CGS fringe patterns, choosing terms for fitting, using data inside the three-dimensional zone, evaluating and optimizing fit, objectively locating the crack tip, and visualizing and interpreting the results.

3.6.2 Digitizing the CGS Fringe Patterns

The first step for CGS analysis is to digitize the fringe patterns. While this is conceptually the simplest step, it is at present the most time consuming. The objective is to systematically digitize the CGS fringe pattern to provide an array of data containing fringe number versus coordinates from the fringe patterns to be fit to analytic fields. While algorithms may be developed for automatically digitizing ideal fringe patterns, in practice one often must contend with superposition of a variety of sources of out-of-plane displacements including loading waves, release waves, and specimen flexing. Other difficulties include the presence of scratches (especially with reflection CGS), fiducial marks, and the variation of CGS fringe density with angle and radius.

The presence of superimposed stress waves and imperfections in specimen flatness can make the determination of fringe numbers difficult at times. Insight can be gained by first printing the entire sequence of fringe patterns and then tracking the individual fringes from images to image, numbering accordingly[4]. Sometimes fringe numbering schemes developed by progressing forward from the start of the image sequence will not agree with those obtained by working backwards from the end of the sequence. These situations must be dealt with as rationally as possible. For the pathological intermediate fringe patterns, the difference in K_α^d from adopting one numbering scheme verses the other is generally less than 10%. Fringe numbering can also be further guided by information gained during data analysis and may be corrected as needed during this stage.

Systematically digitizing fringe pattern images and organizing relevant data requires the designation of several features and properties. Figure 3.2 shows the Matlab GUI created for digitizing fringe patterns and Figure 3.3 is a fringe pattern image which is set up for digitizing and should be referenced for the procedure description throughout the rest of this section. This image shows a crack which is dynamically running upward along a weak bond between PMMA plates. The bond line starts at the bottom and then curves to the right along a sinusoidal trajectory, so the crack tip conditions are mixed mode. The diameter of the interrogating beam is 50 mm. The image of the circular beam is distorted from round by the high speed camera (Cordin 330 rotating mirror type, capable of recording 80 images at up to 2 million frames per second. See Figure 3.4). The vertical black line is also due to the camera (streak line) which in this case coincides with the direction of shear accomplished by the two diffraction gratings. Prior to digitizing the following must be established: First the location of the crack tip must be estimated and specified. Its true position is obscured inside a dark shadow spot. In the figure the shadow spot is where all the radial lines converge. Second, scaling must be established using fiducial marks scribed on the specimen within the field of view. In the figure they are faintly seen to the left of the streak line, with a 1/4 inch diameter dot at the top of the streak line for backup. Third, the direction of the shearing must be provided (dashed blue line extending above the crack tip), as well as an estimate of the tangent to the crack plane at the crack tip (solid blue line). Fourth, the direction of the axis of the "front" lobe (the green-yellow dashed lines to the right of the crack tip[5]) must be indicated since only the

---

[4] The light region far from the crack tip is $m = 0$, and fringe numbers increase as one moves toward the crack tip.

[5] If the wrong lobe is identified as the "front" lobe, this can be fixed later. Most of the time the front lobe is the

absolute value of the fringe number is requested when digitizing, and this direction is needed to choose the correct sign later for fitting. Finally, a fixed point on the specimen must be indicated so that changes in crack tip position from image to image can be calculated. In the figure the top intersection of fiducial marks was used.

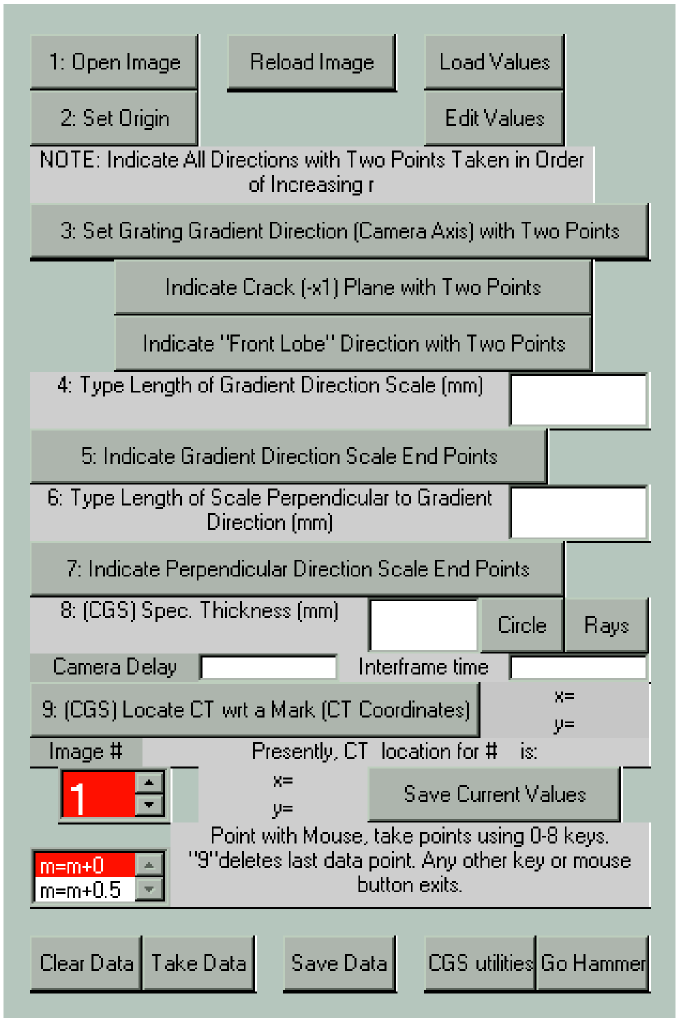

NOTE: Indicate All Directions with Two Points Taken in Order of Increasing r

Point with Mouse, take points using 0-8 keys. "9"deletes last data point. Any other key or mouse button exits.

Figure 3.2: Matlab GUI for digitizing CGS fringe patterns.

With the above information provided, the Matlab program then can draw in markings to assist systematic digitizing. The extent of the three-dimensional zone is indicated (the green oval, which should have the same shape and orientation as the image of the beam). Since CGS produces three

---

one most directly ahead of the crack tip.

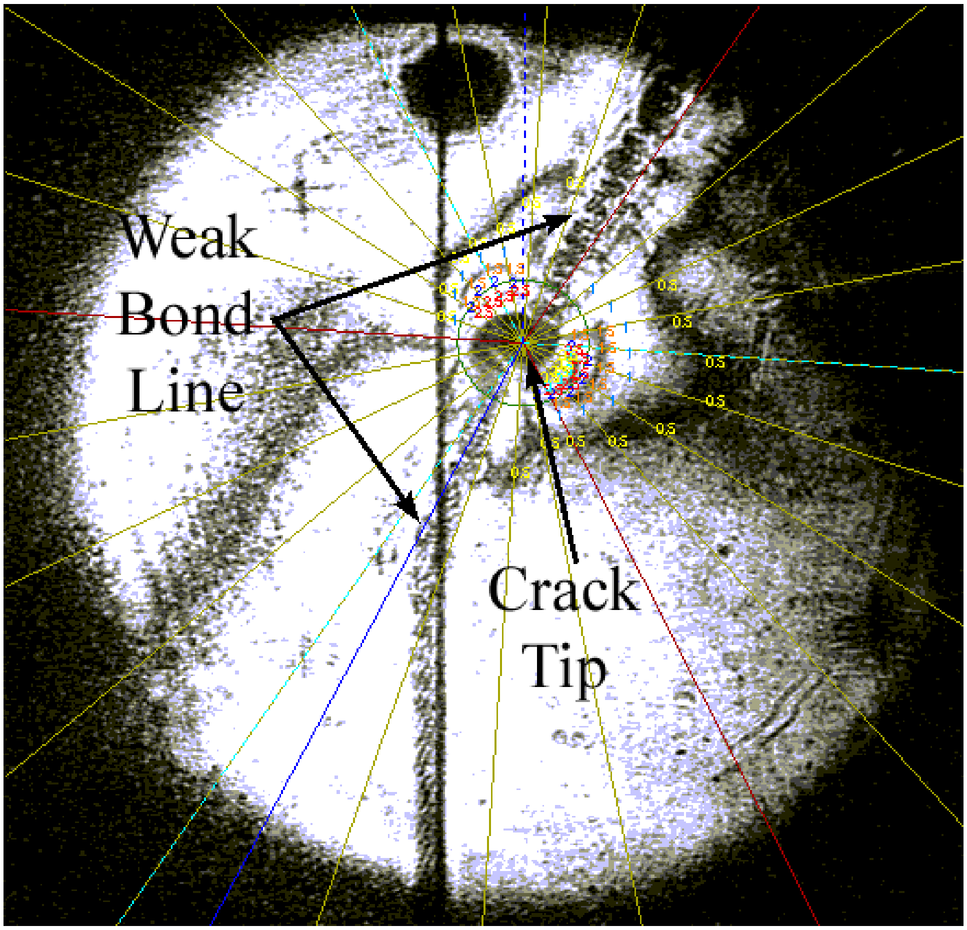

Figure 3.3: CGS fringe pattern image set up for digitizing. (Beam diameter = 50 mm)

lobes each 120° wide (if dominated by leading terms), lobe bisectors (green-yellow dashed radial lines) and lobe separators (red radial lines) are added. Finally radial lines every fifteen degrees are added (yellow lines). Digitizing is systematically performed by manually indicating the intersections of fringes (light and dark, to provide as much data as possible for fitting) with the radial lines and assigning to each intersection the appropriate fringe number. Matlab has a useful *zoom* feature that allows higher density fringes near the crack tip to be accurately digitized. For each intersection point digitized, the coordinates and fringe number are stored. Each digitized point is also indicated on the image by fringe number as shown in the figure. It is best to digitize the entire fringe pattern to provide the most complete data set. During subsequent fitting routines, the (r, θ, m) data is

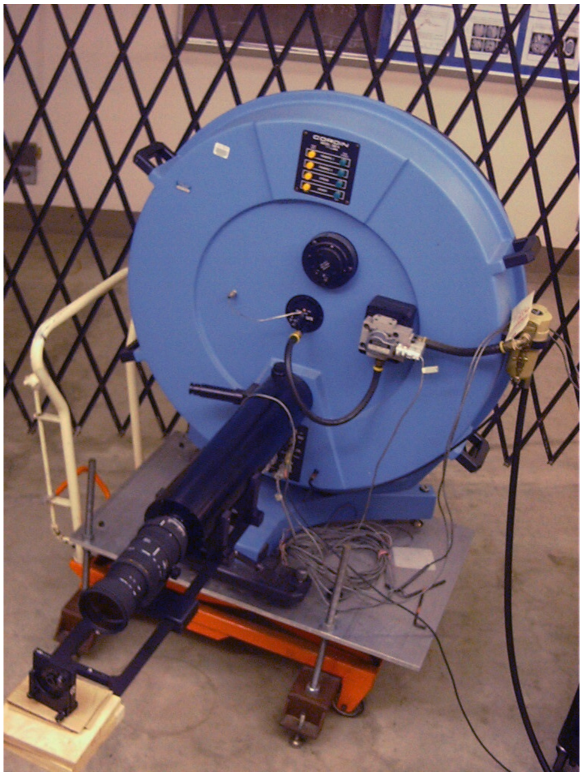

Figure 3.4: Cordin 330 rotating mirror high speed camera.

restricted as required. All information provided to enable digitizing and locate the crack tip is stored by image number.

Regarding error analysis, it is assumed that errors in digitizing the fringes are random in nature and will tend to be self-mitigated by the fitting process. Shearing direction is not difficult to accurately establish, especially when in the same direction as the camera streak line. Estimates of crack tip location and crack tangent are sufficient at this stage, with final values determined systematically and objectively prior to fitting. The exact orientation of other vectors are not essential for fitting. The only sources of systematic error is scaling, which is usually set for one image and used for the entire sequence. Also the indication of the specimen fixed point figures directly into errors regarding changes in crack tip location.

On a final note, the interferogram in Figure 3.3 was more difficult to analyze than typical, with fringe numbers needing to be carefully selected as guided by previous and subsequent images. Once digitized, the subsequent analysis is relatively easy. Reasonable values of mixed mode stress intensity factors were obtained for the entire image sequence from this experiment.

3.6.3 Utilizing Fringe Data Inside the Three-Dimensional Zone

Fringe data inside the three-dimensional zone can be successfully fit so long as the material fracture is well described by LEFM. To do so it must be recognized that the fringe numbers assigned when digitizing experimental fringe patterns are the result of three-dimensional stress fields (m_{3D}). The analytic asymptotic solutions and method of interpreting the CGS fringe patterns are two-dimensional and thus require fringe numbers from plane stress fields (m_{2D}). Therefore, to use fringe data from inside the three-dimensional zone, one needs to convert digitized three-dimensional fringe numbers to effective two-dimensional fringe numbers and then fit in the usual manner. This is easily done once a *conversion factor* is found:

$$f(r,\theta) = \frac{m_{2D}(r,\theta)}{m_{3D}(r,\theta)}\,. \tag{3.70}$$

Figure 3.5 from Rosakis and Ravi-Chandar [43] shows normalized pointwise values of K_I using two-dimensional analysis verses normalized radius r/h as measured using CGS. This plot is essentially the inverse of $f(r,\theta)$ versus r/h. The data is from Martensitic 4340 steel sheets with thicknesses of 6.35, 9.53, and 12.7 mm. As shown the conversion factor $f(r,\theta)$ experimentally is unity outside a radius of a specimen half-thickness and needs to only be determined and applied inside this circle. As $r \to 0$, f goes to infinity due to the singular asymptotic solution, so data very close to the crack tip should not be used. $m_{3D}(r,\theta)$ must be obtained by finite element method or by experiment. This function is bounded at the crack tip and depends on crack conditions such as mode mixity (ratio of modes I and II) and crack velocity. $m_{2D}(r,\theta)$ is obtained from equation (3.61) for the same values of K_I^d and K_{II}^d with all other coefficients set to zero. Fortunately, leading singular terms are the same in all asymptotic expansions regardless of crack path, velocity, etc., so long as the crack

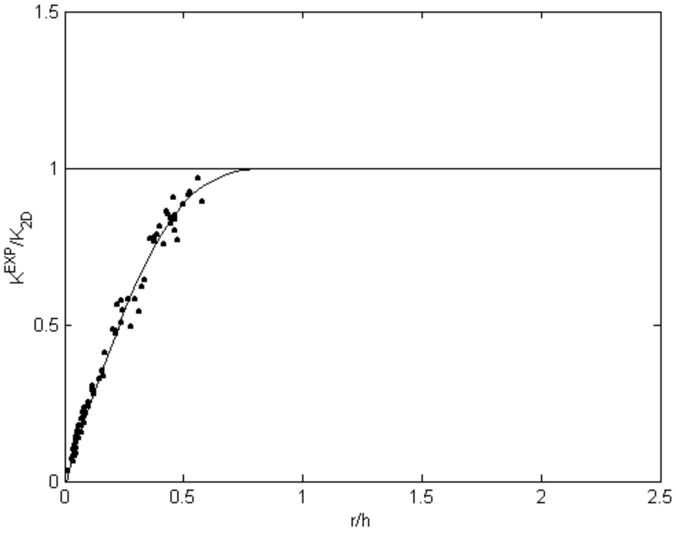

Figure 3.5: Normalized K_I using two-dimensional assumptions versus normalized radius.

speed is much lower than the material shear wave speed. Obviously higher order terms will have little consequence this close to the crack tip for a material described by LEFM.

The simplest case is to model a stationary crack under pure mode I loading. This pure mode I stationary crack case has been implemented and used successfully[6] with calculation details described in Appendix B.

Fringe conversion may be performed for more general situations with some additional complexity. One would need to calculate $f(r, \theta)$ for the same boundary conditions as the actual crack is experiencing, i. e., $m_{2D}(r, \theta)$ would require the same mode mixity, and $m_{3D}(r, \theta)$ would have to be computed for the same mixity and crack conditions. Since the actual mixity is unknown but is to be measured from the fringe data, one would need to develop an iterative or searching process to determine the mixity such that the conversion factor for this mixity produces converted data that, when fit, yields stress intensities with the same mixity. For a given crack condition, m_{3D} can be obtained by superimposing pure mode I and mode II values weighted according to the mixity. m_{2D}

---

[6] One can directly compare fits over data inside the three-dimensional zone with fits over data outside the three-dimensional zone in situations where data in both regions is available.

is easily obtained for any mixity by equation (3.61).

Using data inside the three-dimensional zone is useful because higher order terms in the asymptotic field are negligible and with some materials it is difficult if not impossible to get useful fringe patterns outside the three-dimensional zone. In addition to providing calculation details for mode I conversion factors, Appendix B also proposes a method of using second partial derivatives of out-of-plane displacement to determine K_I^d. This technique eliminates the need of knowing absolute fringe numbers and utilizes data very close to the crack tip.

3.6.4 Fitting CGS Fringe Data with Asymptotic Terms

Figure 3.6 shows the Matlab GUI for fringe data analysis. It has provisions for loading data sets, selecting terms for fitting, performing fits and "searches" (section 3.6.5), plotting and storing results, and correcting fringe numbers. Prior to each fitting, digitized fringe data must be filtered. For a given uncertainty in locating each fringe data point (due to digitizing error, superimposed waves, or specimen imperfections), the data near the centerlines of the three fringe lobes (green-yellow dashed lines in Figure 3.3 for example) will contribute far less error to least squares fitting than data from near the boundaries between the lobes (solid red lines). The space between the lobes coincide with where the denominator of equation (3.27) goes to zero. Consequently, it makes mathematical sense that use of points near these zeros should be avoided. Also data taken near the crack faces is often not useful because the analytic asymptotic solution assumes a mathematically sharp crack. Sometimes the fringe patterns don't reflect this and may confound the fit.

Finally data inside $r/h = 0.5$ is filtered out unless it will be used with three-dimensional zone fringe number conversion. The three-dimensional zone cutoff may be lowered in cases where the benefits of having more data for fitting outweigh the decrease in fitting accuracy and rigor. The closer the data is to the crack tip, the more conservative its contribution to K^d will be.

If sufficient data exists, the utility of the conversion factor with data inside the three-dimensional zone can be assessed. This is done by performing a fit over data only inside the three-dimensional

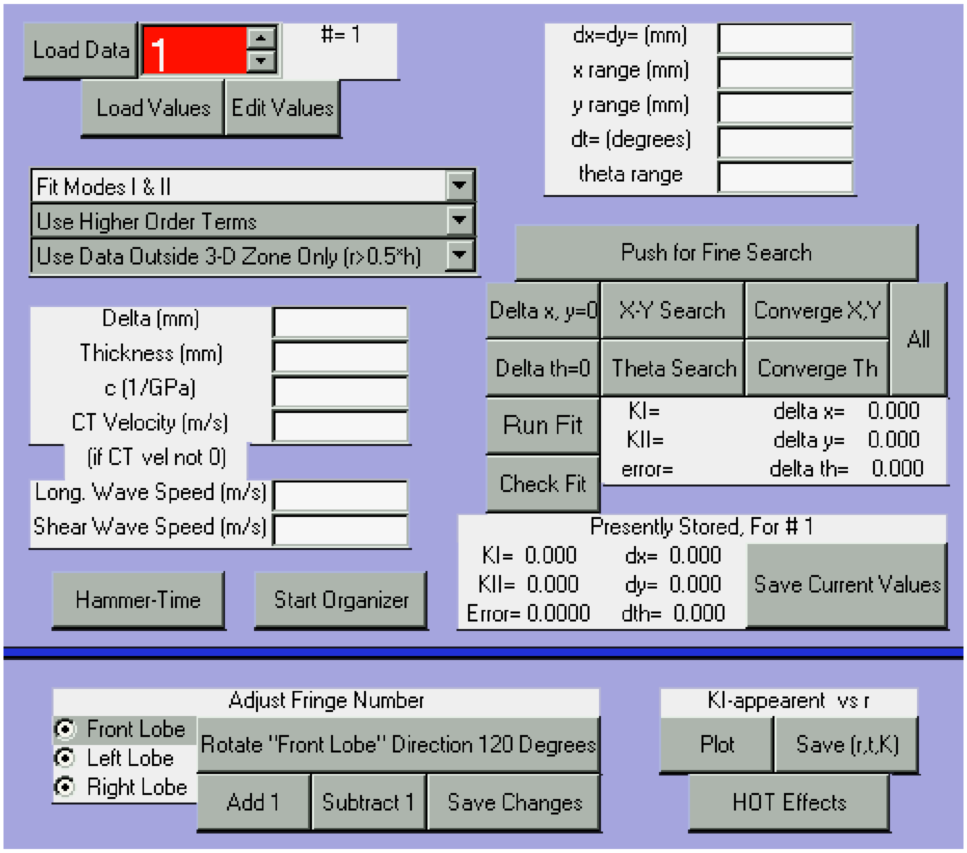

1

#= 1

Fit Modes I & II

Use Higher Order Terms

Use Data Outside 3-D Zone Only (r>0.5*h)

KI= delta x= 0.000
KII= delta y= 0.000
error= delta th= 0.000

Presently Stored, For # 1
KI= 0.000 dx= 0.000
KII= 0.000 dy= 0.000
Error= 0.0000 dth= 0.000

Figure 3.6: Matlab GUI for fringe data analysis.

zone using the conversion factor. Then a fit is performed over data only outside the three-dimensional zone in the usual manner. The stress intensity factors obtained by both fits should match if the material is well modeled by LEFM.

Fitting is performed by using equations of section 3.5[7], keeping only those components associated with the desired fitting terms. In general it is best to use all the mode I and II terms provided as this will provide insight into the size of the K-dominated region and how well the analytical model describes the experiment. For example, some fit coefficients should be zero for some conditions, as mentioned in section 3.5. Fewer terms can be used to enforce certain conditions (pure mode I, for example) or to reduce computational time, though in practice this is usually not necessary. The

---

[7] In Matlab, only the $\underset{\sim}{A}$ matrix and $\underset{\sim}{x}$ vector must be assembled as Matlab has a built in function to find the least-squares solution—see “help slash” in Matlab.

number of fitting terms may need to be reduced in cases where insufficient data exists, especially when there is little variation in r over the data set. In fits performed exclusively inside the three-dimensional zone, only the leading term(s) should be used as the conversion factor is constructed assuming K-dominance.

3.6.5 Evaluating and Optimizing Fit and Locating Crack Tip

As mentioned in section 3.6.2, crack tip location and crack tangent at the tip can only be visually estimated. With fitting procedures available, different crack tip locations can be considered by offsetting the fringe data coordinates, filtering the data, and then fitting. In order to decide which assumed crack tip location is optimal, a measure of fitting error is needed. Given an error metric, the assumed crack tip location that has the lowest error can be objectively and repeatably chosen as the crack tip location. The same can be done with crack tip tangent. While the crack tip location chosen by this approach may not coincide with the actual crack tip[8] due to blunting, tunneling, etc. its objectivity makes it ideal for determining crack velocities. Furthermore, by minimizing an error it is ensured that the crack tip stress fields are optimally fit to analytic asymptotic fields as desired.

The error metric used is given by

$$E = \frac{1}{N}\left(\sum_{n=1}^{N}\left(m_n(\underset{\sim}{x}) - \hat{m}_n(\underset{\sim}{x})\right)^2\right)^{1/2} \tag{3.71}$$

where m_n is the fringe number for the n^{th} point as specified during digitizing, $\hat{m}_n$ is the fringe number calculated from the fit at the same location using equation (3.61), and N is the total number of data points. This error is the RMS error in fringe number divided by the total number of data points. This definition allows meaningful comparison of fits over different data point sets.

The least troublesome method of locating the crack tip is by systematically "searching" over a gridded region known to contain the crack tip, which is easily done given the modular nature of programming in Matlab. At each grid intersection, data is filtered prior to fitting, after which the fit

---

[8] With crack tip tunneling and roughness, a single precise 2D location for the crack tip will not exist anyway.

values and error are stored. Problems can occur if large search areas and small data sets are used, especially of all data from one lobe is filtered out. The next section describes useful diagnostic plots that allow easy detection of such irregularities.

One can also examine error values, error trends, and other data to check fringe numbering and crack tip stress field model applicability in general. In many cases error will also increase at the moment of crack initiation.

3.6.6 Visualizing and Interpreting Results

The analysis of data is greatly facilitated by several plots that can be produced in Matlab and summoned via GUI. This section contains sample plots and describe their use. All plots provided in this section are from a test on commercial grade 6Al-4V titanium nominally loaded in mode I in a drop weight tower. All mode I and II fitting terms were used on data outside the three-dimensional zone only.

After searching for the crack tip location with minimum error, a surface plot of error versus position (Figure 3.7) can be created. Ideally the location of minimum error lies in the center of a bowl-shaped concavity. This plot can help indicate whether the crack tip search area is too big or too small. K_I^d, K_{II}^d, and $K_{eff}^d = \sqrt{(K_I^d)^2 + (K_{II}^d)^2}$ can also be plotted versus position —usually they do not vary too much with position which increases confidence in stress intensity factor objectivity (also Figure 3.7). The location $(0, 0)$ is where the crack tip was guessed to be located during digitizing, with the white "o" indicating the crack tip location which minimizes fit error. Any unusual offset between the two can be due to a lack of data/filtering problem or incorrect fringe numbering. The former problem occurs when the search area is big enough that perhaps an entire lobe of data is filtered out, leaving a small subset that can be fit with very little error by the many terms. This is fixed by reducing the search area. The latter problem can be fixed by adding or subtracting an integer to all the fringe numbers from the incorrectly numbered lobe(s). The crack tip with minimal error will tend toward fringe lobes that have fringe numbers too high. The line running leftward from the crack tip indicates the crack tangent that also minimizes error.

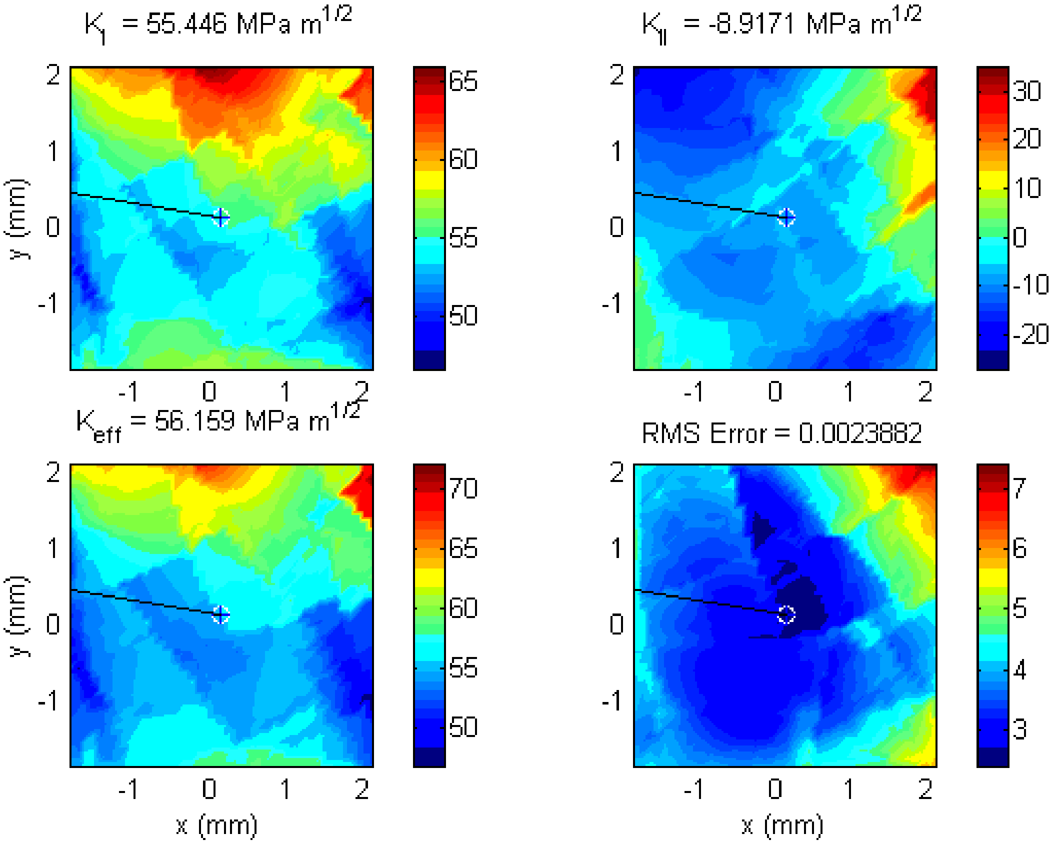

Figure 3.7: Surface plots of CGS K^d and error versus prospective crack tip location.

Figure 3.8 is similar to Figure 3.7 but shows error and K^d verses angle between the assumed crack tip tangent and the shearing direction. Angle with minimal error can be influenced greatly by allowing or disallowing mode II terms in the fit.

Fringes from the fit can also be superimposed on the original data to check for agreement. In Figure 3.9, the lines are of integer and half integer fringes obtained from the fit, and the labeled dots are of the digitized data that passed filtering and were used in the fit. The circle diameter is equal to the specimen thickness and denotes the three-dimensional zone boundary. The error for this fit is 0.0024. Fit values can be calculated no matter how pathological the data. By comparing the fringe patterns from the fit to the experimental fringe patterns, it is readily apparent if there are

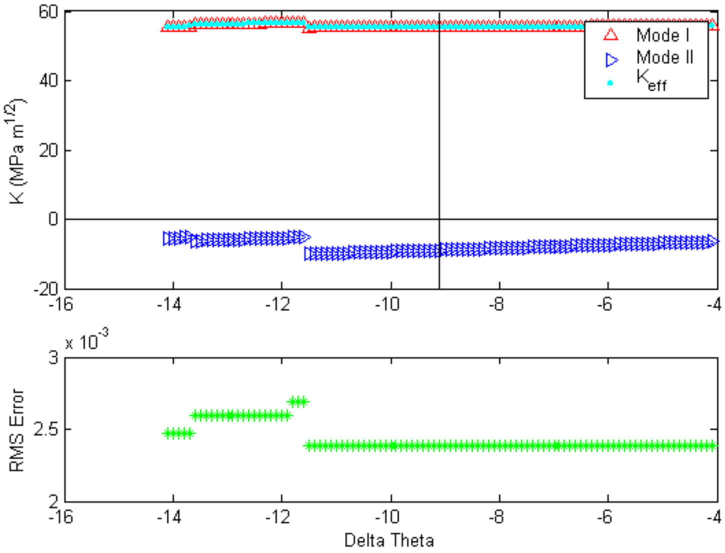

Figure 3.8: Plots of CGS K^d and error versus prospective crack tip angle.

significant errors. It should be noted that for the outer fringes the distance from the fringe to the data point of the same fringe number may be relatively large, but the error these points contribute to the error calculation may still be small due to the singular nature of the crack tip fields.

The region of K-dominance can be visualized by surface plotting the ratio of the stress fields associated with the most general fit normalized by the stress fields associated with the K term only, as done in Figure 3.10. This figure shows stress field from all term fit normalized by K_I^d-field (top left), K_{II}^d-field (middle left), and both K_I^d and K_{II}^d, multiplied by 100%. Also shown are the actual data points used (red dots) and the three-dimensional zone (black dashed circle). The white contour lines are every 25%. In this case it appears that K_I^d sufficiently describes the crack tip stress state, with disparity only near the crack faces. Plots of the stress field contribution of each of the fitted coefficients (bottom of Figure 3.10) are also useful in evaluating the fit as in many cases (symmetric loading with straight crack, stationary crack, constant crack velocity, etc.) some of the terms should contribute nothing.

Finally after digitizing many images in a series, plots of K^d, error, crack tip position, etc., versus

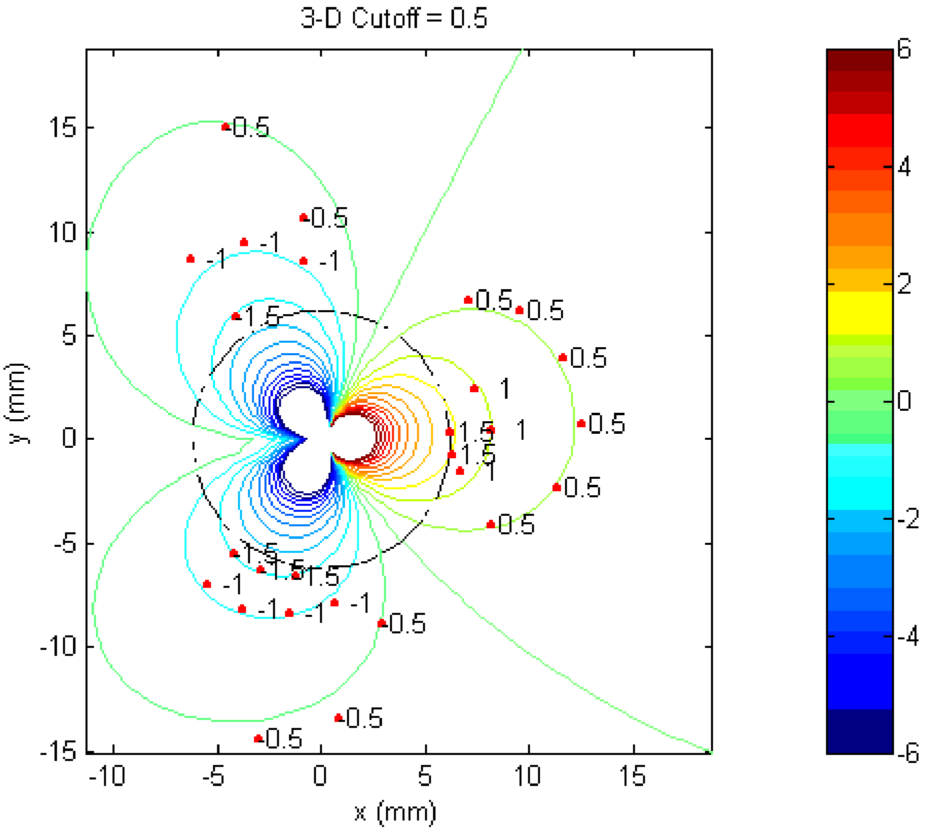

Figure 3.9: Plot comparing CGS fit to digitized data.

image number or elapsed time can be made to determine initiation, critical fracture toughness, crack tip velocity, and so forth. Abnormal jumps in any of these plots can be indicative of fringe numbering error or other anomalies.

3.6.7 Comments

Once the tedious interferogram digitizing is accomplished, the Matlab GUIs allow one to rapidly process the data and see results and plots that aid interpretation. Once methodology is established for a given experiment fringe sequence, one GUI can be used that allows the user to point out the data sets from all the images of a test, select the terms for fitting and crack tip searching parameters to use, then start the program and walk away until all the data is analyzed and results organized.

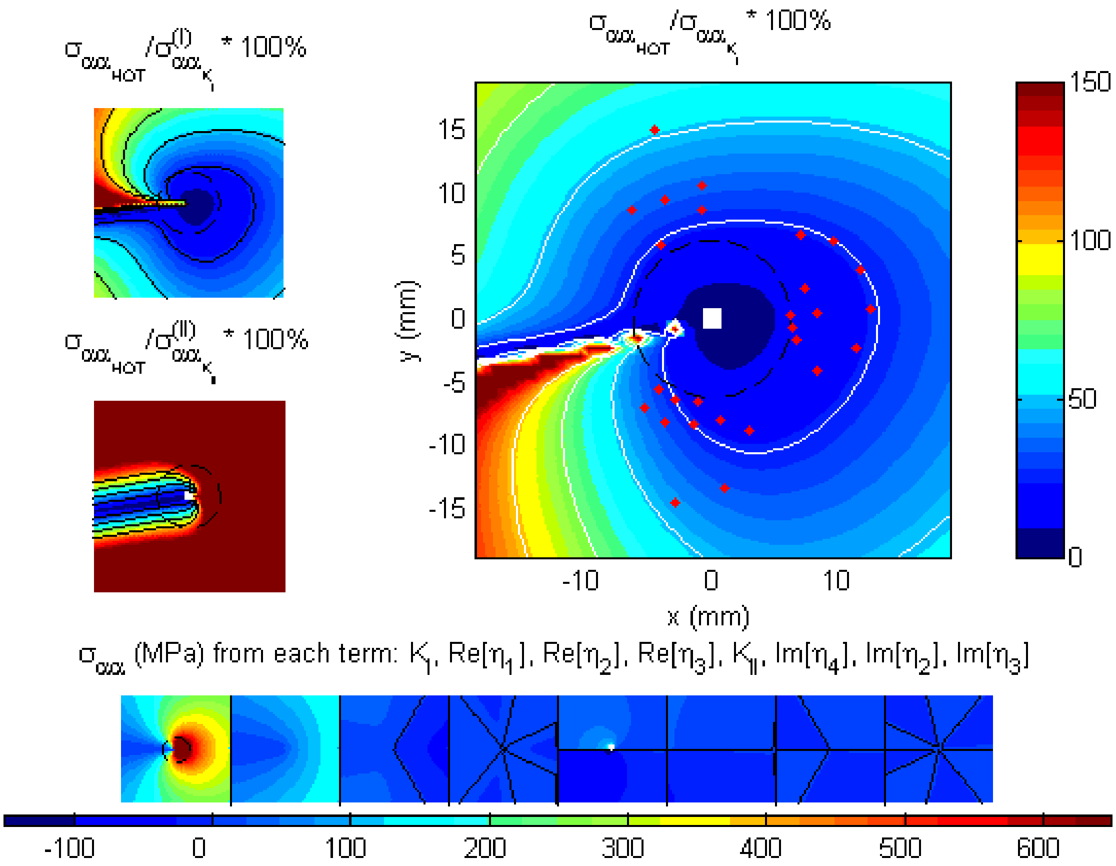

Figure 3.10: Plot indicating extent of K-dominated field and stress field contribution by term.

The very complicated governing equations, nested iterations, and data structures are hidden behind novice-friendly GUIs.

No matter how simple the GUIs make analysis appear, it must be kept in mind that analyzing these fringe patterns is somewhat of an art and must be done carefully. Practical difficulties can arise, especially in choosing fringe numbers in the presence of loading waves or specimen flexing. The fitting algorithms will return values no matter how poorly the fitting terms are chosen, so it must be verified that the terms used for fitting span the actual material mechanical behavior. Finally the iterative schemes to determine crack tip location work well in general but can be overwhelmed. This is sometimes due to erroneous fringe numbering but can be caused by other things such as lack of sufficient data points. The plots are useful first to be critical of the analysis and then to understand the material behavior.

3.7 A Comparison of Results Obtained by Different Fits

3.7.1 Overview and Experiment Details

The consequences from choice of fitting terms on final results depends on the stress fields being fitted. Obviously if the crack tip is racing along curved paths under mixed mode loading, the full span of all the terms is necessary to hope to capture the essence of the crack tip stress field. In simpler situations such as a stationary crack loaded in pure mode I, it would be expected that fewer terms should suffice in which case the fitting mathematics should return coefficients near zero for inactive degrees of freedom if used. However, with real fringe patterns from real experiments, it may be of interest to observe what actually happens on a case by case basis.

In this section fitting results are presented from a drop weight tower test of a commercial grade 6Al-4V titanium alloy. A pre-cracked plate with nominal thickness of 0.5 inch is impacted at 9 m/s in three point bend. Lower span is 9 inches. The overall in-plane dimensions of the plate specimen are 10 inches by 4 inches. The crack consists of fatigue crack extending 2 millimeters ahead of a 1.25 inch notch created by wire EDM. The crack is centered below the load point to obtain nominal mode I loading (Figure 3.11). The distance between the two diffraction gratings, Δ, is 30 mm.

All fits were performed using full searches, i. e., crack tip position and tangent were searched in turn until both converged. Comparison is made between a fit using K_I^d, K_{II}^d, and higher order terms over data outside the three-dimensional zone, a fit of the K_I^d term only applied to data outside the three-dimensional zone, and the K_I^d term fit only to data inside the three-dimensional zone making use of the conversion factor discussed in section 3.6.3. Interframe time for the image sequence is 5 μs. All elapsed times are from camera trigger, or when the specimen is first impacted by the drop weight tower tup.

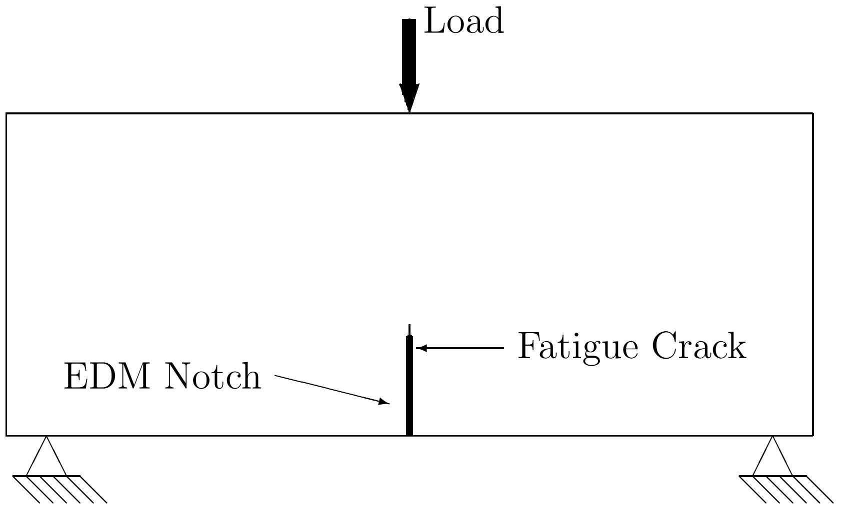

Figure 3.11: Loading configuration for mode I drop weight tower test.

3.7.2 Comparison of Stress Intensity Values

A plot of K_I^d verses time from the three fits is given in Figure 3.12. This comparison has three noteworthy features. First, at initiation (dashed vertical line) as chosen, all three fits provide values of K_I^d which are in close agreement.

Second, up to initiation the fits over data inside the three-dimensional zone using the conversion factor agree very well to the full all-term fit. After initiation it diverges, as should be expected considering that the conversion factor as used is valid for stationary cracks only.

Third, the K_I^d fit outside the three-dimensional zone does not agree well with the full fit until initiation, after which agreement is excellent. Since the full fit does not indicate the presence of significant mode II components in the crack tip field (Figure 3.13), this disparity must be due to the contribution of higher order terms. Figure 3.14 shows the fringe pattern image at 90 μs, just before initiation, when the disagreement between the full term fit and leading term fit is maximum.

3.7.3 Comparison of Fit Error

The fit errors verses time for the three fitting term/data selections are plotted in Figure 3.15. As expected, the most general fit produces the least fitting error. Often the error for the fit over data

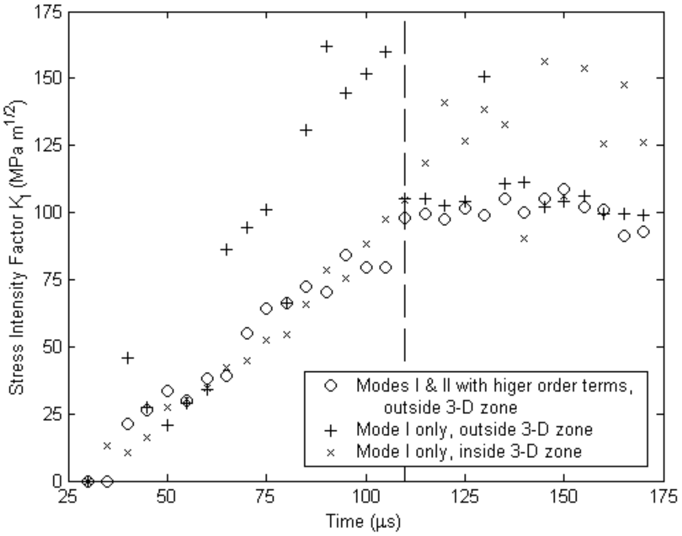

Figure 3.12: K_I^d versus time from three different fitting term / data set combinations.

inside the three-dimensional zone will jump up at initiation, but in this particular experiment it does not.

Error can be influenced greatly by the number of data points fit, even though error is normalized to be per point. An extreme example would be that of a few random data points fit without error by many terms.

3.7.4 Comparison of Crack Tip Locations

Finally crack tip location for each fit is taken to be the location estimated during digitizing refined by the change in crack tip location found during crack tip searching. Crack position versus time for the three fits is given in Figure 3.16. The crack tip data is not as smooth as hoped for from an objective location method. Part of this location noise is due to error introduced in indicating the fixed reference point during digitizing. The more precise the fixed point, the more difficult it is to see due to the optical grating shear and adjacent fringes. A second source of error prior to initiation is that early in the loading there is very little fringe data available for fitting.

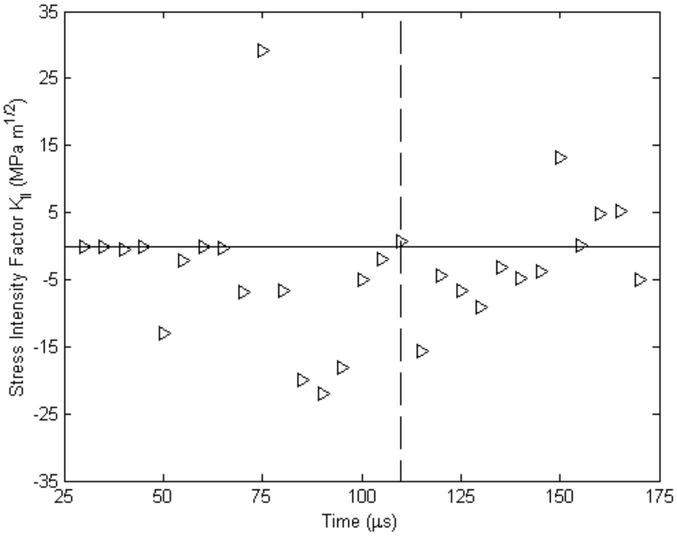

Figure 3.13: K_{II}^{d} versus time from all-term fit.

The apparent location of the crack tip can also move forward prior to initiation due to crack tip blunting, which is the forward motion of the crack tip stress fields as yielding occurs at the crack tip.

In any case, the crack tip location data is helpful for determining initiation and sufficient to estimate crack velocities. The crack tip searches/error minimizations are primarily intended to determine fit coefficients objectively.

3.7.5 Comments

The above plots are just a few items for consideration and comparison. Other items of possible interest may include coefficients of higher order terms, corrections of digitizer-indicated crack tip location found by crack tip searches in both directions normal and tangent to the crack plane, as well as changes of crack plane angle. All this data can be useful for checking fringe numbers and other procedural operations, for choosing and justifying fitting terms and search procedures, and finally for understanding the crack mechanics observed. Interpretation is somewhat of an art form

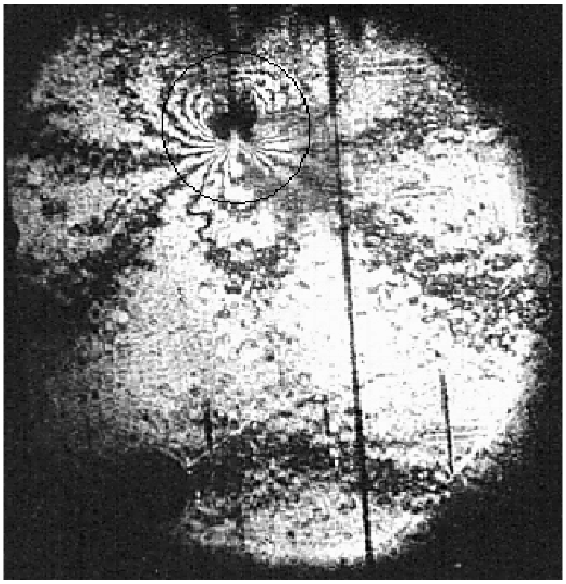

Figure 3.14: CGS fringe pattern at 90 μs after impact. (Beam diameter = 50 mm)

requiring understanding of both theory and implementation particulars, such as how the error is defined, how the searches work, and how data is filtered.

3.8 Conclusions

CGS technique can provide a great deal of information about dynamic crack tip mechanical fields. Measurement of stress intensity factors for non-uniformly propagating dynamic mixed mode cracks moving along arbitrary paths in homogeneous linear elastic isotropic materials can be obtained by utilizing more general crack tip solutions. The tools described in this chapter such as methods for using data inside the three-dimensional zone, an error metric and its use to objectify crack tip location and tangent, and various plots for result visualization make this method much more suitable for engineering materials. Finally Matlab GUIs take all of the complexity above and allow it to be hidden behind simple user interfaces.

For the experiment analyzed in this chapter, data from inside the three-dimensional zone was successfully used to determine stress intensity factors up through crack initiation. The analysis of

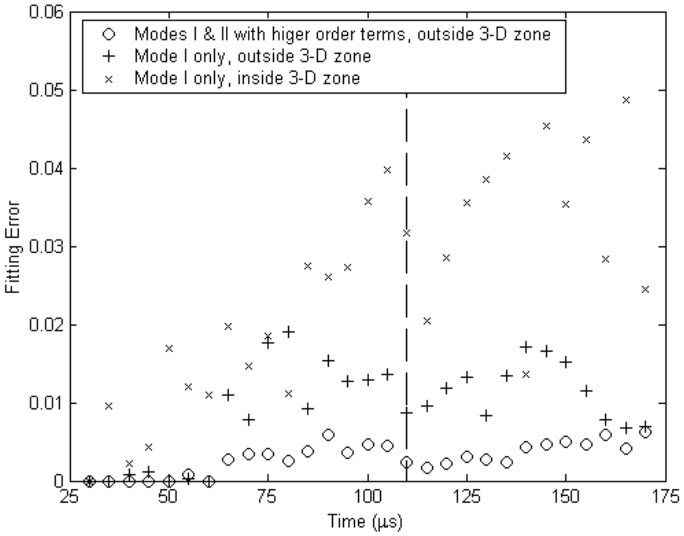

Figure 3.15: Fitting error versus time from three different fitting term / data set combinations.

fringe data from outside the three-dimensional zone required the use of higher order terms.

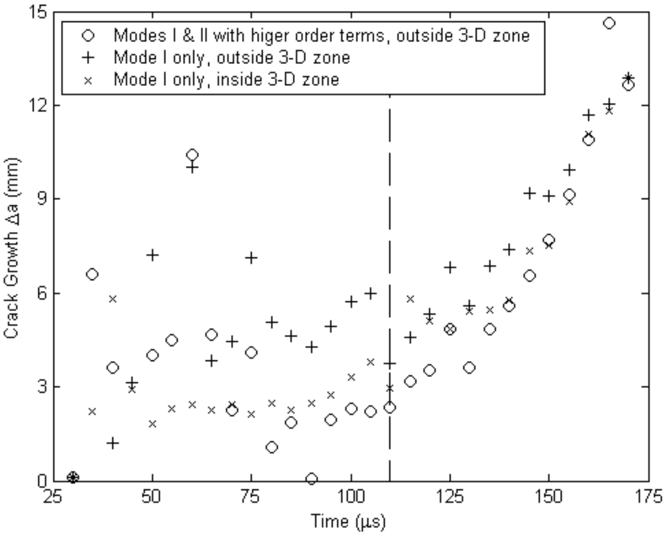

Figure 3.16: Change in crack tip position versus time from three different fitting term / data set combinations.

Chapter 4

Dynamic Crack Initiation Toughness in Titanium Alloys

4.1 Introduction

Titanium alloys are being increasingly used in aerospace and other applications where high strength, low weight, and reliability are of paramount importance. In such applications complete material fracture properties are vital for three reasons. First, a greater certainty in material fracture properties allow the material to be more efficiently utilized, saving material weight and cost. Second, the material fracture properties determine the maximum allowable flaw size for some duration of safe operation. This dictates the level of quality control required during fabrication and the frequency and resolution of maintenance inspections. Third, in such dynamic applications limited quasistatic understanding of material fracture behavior may not be sufficient. For some materials at some dynamic loading rates the dynamic fracture toughness may be *lower* than the quasistatic fracture toughness.

Three titanium alloys are tested to determine quasistatic and dynamic crack initiation toughness.

The three alloys are a commercial grade 6Al-4V Titanium alloy, 6Al-4V Ti ELI, and Timetal 5111. Chemical composition of the materials tested is given in Table 4.1, and nominal mechanical properties can be found in Table 4.2.

Constituent	6Al-4V Ti	6Al-4V Ti ELI	Timetal 5111
Aluminum	6.225	5.80	4.5-5.5
Vanadium	3.875	3.96	0.6-1.4
Tin	-	-	0.6-1.4
Zirconium	-	-	0.6-1.4
Molybdenum	-	-	0.6-1.4
Nitrogen	0.013	0.015	0-0.03
Oxygen	0.19	0.073	0-0.11
Carbon	0.018	-	0-0.08
Hydrogen	0.0081	-	0-0.015
Iron	0.16	0.034	0-0.25
Yttrium	0.001	$<$ 59 ppm	-
Silicon	-	-	0.06-0.14
Titanium	Balance	Balance	Balance

Table 4.1: Chemical makeup of titanium alloys tested.

Property	6Al-4V Ti	6Al-4V Ti ELI	Timetal 5111
Hardness (Rockwell C)	34	25	28
Ultimate Tensile Strength (MPa)	900	860	850
Yield Strength (MPa)	830	790	745
% Elongation in 2”	10%	10%	13%
% Reduction of Area Bar	25%	25%	28.5%
Modulus of Elasticity—Tension (GPa)	114	114	107-114
Modulus of Elasticity—Torsion (GPa)	42	42	-
Poisson Ratio	0.32	0.32	0.32
Beta Transus (°C)	1000	990	980
Annealing Temperature (°C)	700-830	700-830	-
Forging Temperature (°C)	950	950	-

Table 4.2: Nominal mechanical properties of 6Al-4V Ti, 6Al-4V Ti ELI, and Timetal 5111.

The 6Al-4V Ti is very versatile and probably the most widely used titanium alloy. 6Al-4V Ti ELI has nominally the same composition with the exceptions of lower interstitial oxygen and iron content. This small change lowers strength marginally, but greatly increases fracture toughness. ELI has very good corrosion resistance which adds oceanic and bio-engineering utility. The third alloy is a product of Titanium Metals Corporation designated Timetal 5111 (Ti-5Al-1Sn-1Zr-1V-.8Mo).

As described by Timetal,

> Timetal 5111 (pronounced 5 triple 1) is a near alpha titanium alloy of intermediate strength. This alloy has been designed for high toughness, good weldability, stress-corrosion cracking resistance, and room temperature creep resistance. Timetal 5111 is ideally suited for applications in marine environments where toughness and corrosion resistance are essential. The alloy has been produced on a commercial scale. Forging and machining characteristics of Timetal 5111 are very similar to Timetal 6-4. Timetal 5111 was developed jointly with the Navy, and has been selected as the material of choice for a submarine application. Timetal 5111 is included in the ASTM standards as ASTM Grade 32.

4.2 Experimental Setup

4.2.1 Quasistatic Setup

Quasistatic tests were performed on C(T) type specimens as described in section 2.2. For this technique, only the applied load must be recorded. Table 4.3 gives specimen nominal dimensions. Some specimens were side-grooved. Variation in dimensions was caused by specimen material availability constraints.

Material	a (mm)	W (mm)	B (mm)
6Al-4V Ti	20-21	84	12.3
6Al-4V Ti ELI	11.4-12.0	77	11.0-12.7
Timetal 5111	17-19	84	15-17

Table 4.3: Nominal dimensions of C(T) specimens for quasistatic fracture toughness testing.

4.2.2 Dynamic Test Setups

Dynamic tests were performed on three point bend specimens with measurement techniques from chapter 2 employed as appropriate to each material. For the more ductile 6Al-4V Ti ELI and

Timetal 5111, the COD technique was used, all on 25% side-grooved specimens save one ungrooved ELI specimen. Due to specimen material availability constraints the ELI specimens were held in large steel grips to allow a long 340 mm lower span to be used. Otherwise the lower span would be limited by the specimens' 125 mm length. With such a short span, the specimens elastically compress, buckle, and fly out of the drop weight tower instead of fracturing into two as desired. The grips are shown holding a broken specimen in Figure 4.1. Two strain gages, each oriented to measure K_I^d, are visible about one-third of the way up from the specimen bottom adjacent to the break. Such gages could help determine crack initiation time, but otherwise contributed no useful measurements due to the specimen side-grooves.

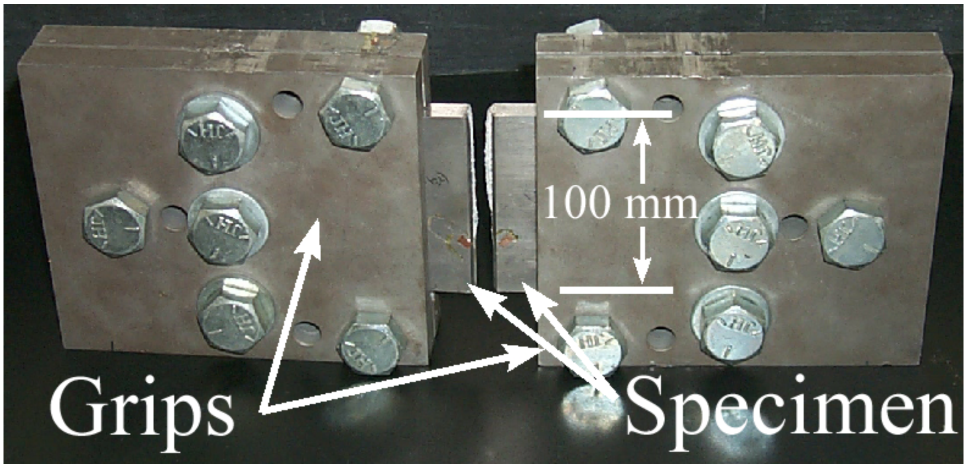

Figure 4.1: Grips used to hold small 6Al-4V Ti ELI specimens for dynamic bend testing.

The 6Al-4V Ti toughness was measured by all techniques using both side-grooved and ungrooved specimens.

Nominal specimen dimensions for the three materials are given in Table 4.4. Again, dimensional variations are due to specimen material availability constraints.

Material	a (mm)	W (mm)	B (mm)
6Al-4V Ti	34	100	12.5
6Al-4V Ti ELI	28	93	8-11
Timetal 5111	34	101	15

Table 4.4: Nominal dimensions of three point bend specimens for dynamic fracture toughness testing.

4.3 Experimental Observations and Results

4.3.1 Overview

Due to the limits in what can be learned from the COD measurement technique, comparisons between the materials' behavior can only be made for initiation toughness, quasistatic K_I-displacement data, and fracture surface appearance. The CGS results for the 6Al-4V Ti provide additional information for propagating cracks in this material which is presented following the comparisons.

4.3.2 Initiation Toughness

Initiation toughness versus loading rate for each of the three materials is given in Figures 4.2–4.4. Because strain gage data is taken simultaneously with the optical methods and the results agree well for specimens without side-grooves, this data is not included in the plots.

For the 6Al-4V Ti (Figure 4.2) under dynamic loading, no significant difference in initiation values were observed between specimens with and without side-grooves, while under quasistatic loading, values for ungrooved specimens are higher (125.1 and 129.1 $MPa\sqrt{m}$) than that from a specimen with side-grooves (91.3 $MPa\sqrt{m}$). The disparity in quasistatic values indicates the presence of thickness effects. Assuming that the side-grooved specimen provides a plane strain toughness value, the value from the specimens without side-grooves is about 35% high. The value of h/r_p for the two specimens without side-grooves is about 5.8, indicating that the thickness effect in this titanium alloy tested quasistatically is more pronounced than in the aluminum tested by Irwin (equation 1.5, Figure 1.2). The toughness for aluminum with the same value of h/r_p is about 12% above its plane strain toughness.

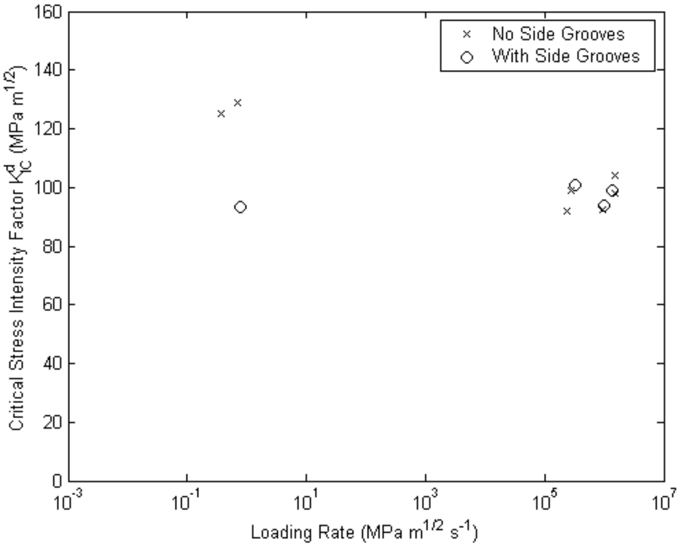

Figure 4.2: Initiation toughness versus loading rate for 6Al-4V Ti.

Because yield stress increases with strain rate, the characteristic plastic zone size r_p at crack initiation decreases with loading rate (though it increases with K_{IC}^{d}). Thus for the dynamic specimens the ratio h/r_p is larger, which accounts for the similar initiation values for specimens with and without side-grooves.

In both loading regimes the side-grooved specimens' fracture surfaces have no shear lips as expected. In the ungrooved geometries the quasistatically tested specimen quickly transitions from the shear lip free fatigue crack to 100% shear lips, while the dynamic fracture surfaces transition to less than 25% shear lips. This is consistent with the dynamic fracture being more in a state of plane strain than the quasistatic tests on the same material with same thickness. Photographs of typical fracture surfaces can be found in section 4.3.4.

For the 6Al-4V Ti ELI (Figure 4.3) the ratio h/r_p is about 2.1 for quasistatic loading thus the disparity between initiation toughness values from specimens with and without side-grooves is expected to be significant. In aluminum, quasistatic toughness for the same ratio of h/r_p is 73% higher than its plane strain toughness. With the 6Al-4V Ti ELI for both quasistatic and dynamic regimes the initiation toughness values from specimens without side-grooves is about 20% higher than values from specimens with side-grooves. The increase in h/r_p ratio for dynamic loading is insufficient to reduce the thickness effect, and the fracture surfaces of ungrooved specimens tested quasistatically and dynamically are macroscopically indistinguishable. Thus unlike the 6Al-4V Ti, the 6Al-4V Ti ELI shows a less pronounced thickness effect compared to aluminum.

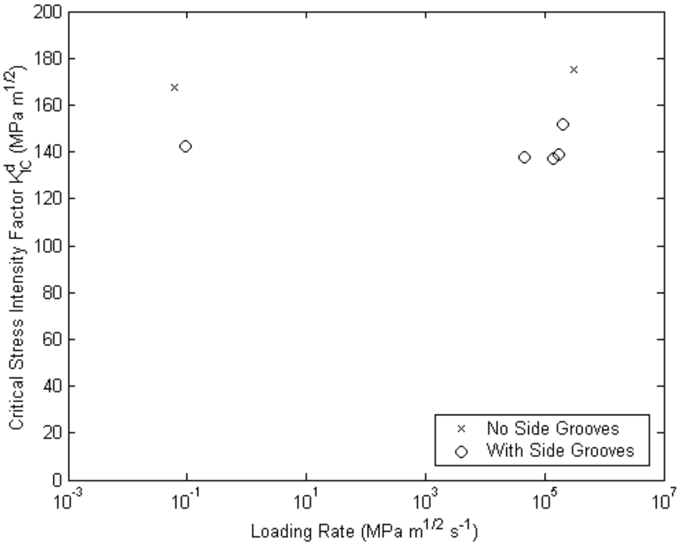

Figure 4.3: Initiation toughness versus loading rate for 6Al-4V Ti ELI.

For the Timetal 5111 (Figure 4.4) the ratio h/r_p is about 2.5. Only one specimen without side-grooves was tested, quasistatically. Despite 100% shear lips this specimen provided an initiation toughness in line with those from side-grooved specimens, thus no thickness effect in this material was observed. The grooved specimens have slight curvature in the fracture surface.

For the following comparisons, the results from the side-grooved specimens are assumed to be plane strain values, as well as results from the ungrooved dynamic 6Al-4V Ti tests and the single ungrooved Timetal 5111 quasistatic test. Figure 4.5 shows these initiation toughnesses versus loading rate for comparison between materials.

Using average plane strain values for the data obtained, the 6Al-4V Ti ELI is 53% tougher than

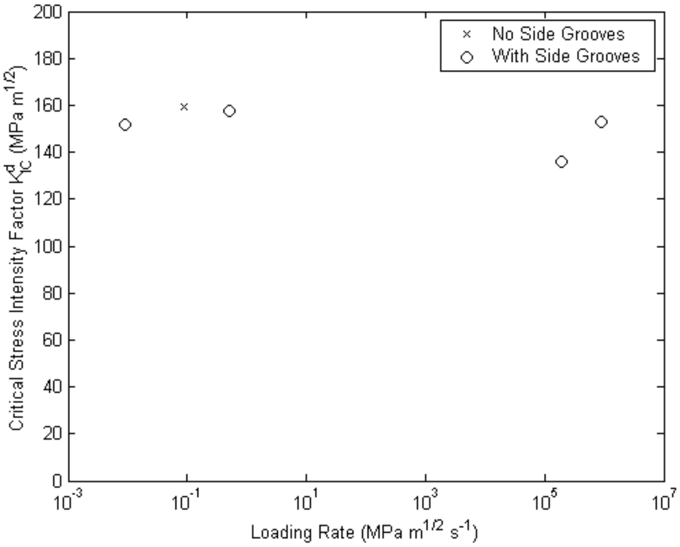

Figure 4.4: Initiation toughness versus loading rate for Timetal 5111.

the 6Al-4V Ti under quasistatic conditions and 45% tougher under dynamic loading. Comparing Timetal 5111 to 6Al-4V Ti, it is 66% and 48% tougher under quasistatic and dynamic loading respectively. The dynamic values are good for the loading rates covered by these tests. In general, fracture toughness is a function of loading rate. Dynamic toughness is influenced by inertial/rate effects (toughening) and thermal effects (softening) from plastic work heat dissipation at the crack tip. As loading rate increases, material inertia dominates and toughness increases. At lower loading rates the two effects are in competition, and in some cases thermal effects can be more influential, causing fracture toughness to drop significantly below quasistatic toughness values—a potentially dangerous situation. For these limited data sets, no indication of large deviation from quasistatic values is apparent though the possibility of such behavior at other loading rates is not ruled out. In comparing the average of dynamic results with quasistatic values, using plane strain values only, the 6Al-4V Ti dynamic toughness is 4.6% higher than the quasistatic value, with 6Al-4V Ti ELI down a mere 0.7% and Timetal 5111 6.6% lower. To complete the rate effect picture, more tests should be performed with an effort made to fill in the gap between the quasistatic tests and drop weight

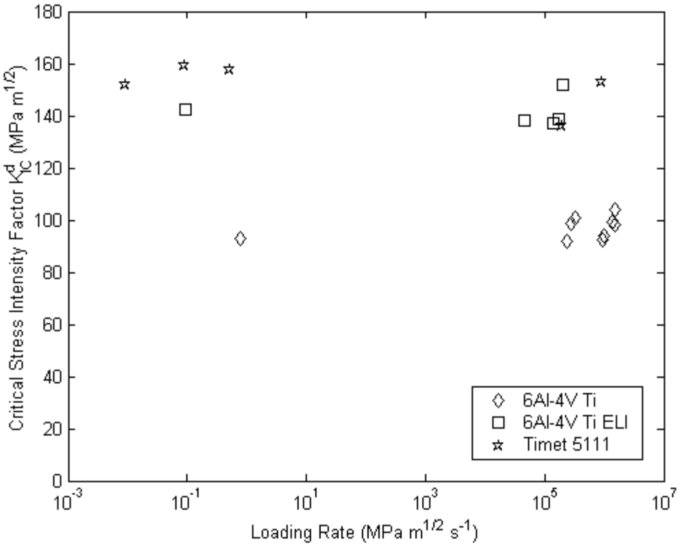

Figure 4.5: Plane strain initiation toughness versus loading rate for 6Al-4V Ti, 6Al-4V Ti ELI, and Timetal 5111.

dynamic tests, as well as at even higher loading rates.

4.3.3 Quasistatic Load-Displacement Data

For the quasistatic tests, stress intensity versus global displacement of the loading crosshead can be plotted as shown in Figure 4.6. This plot shows results for side-grooved specimens, one of each material. The specimens are not of the identical geometry (see Table 4.3) but the same test fixtures are used. Maximum loads for the three tests are 60 kN for the 6Al-4V Ti, 82 kN for the 6Al-4V Ti ELI, and 147 kN for the Timetal 5111. At the high loads for the Timetal 5111 the loading pins deformed a total of perhaps a millimeter, accounting for at least some if not all of the nonlinearity of its trace at higher values of K_I. Any displacement contribution due to load frame compliance would be linear and decrease the slope of all traces uniformly. The total side-groove depths for each specimen plotted is 21.3% for the 6Al-4V Ti, 51% for the 6Al-4V Ti ELI, and 25.5% for the Timetal 5111. All failed in flat fracture as expected.

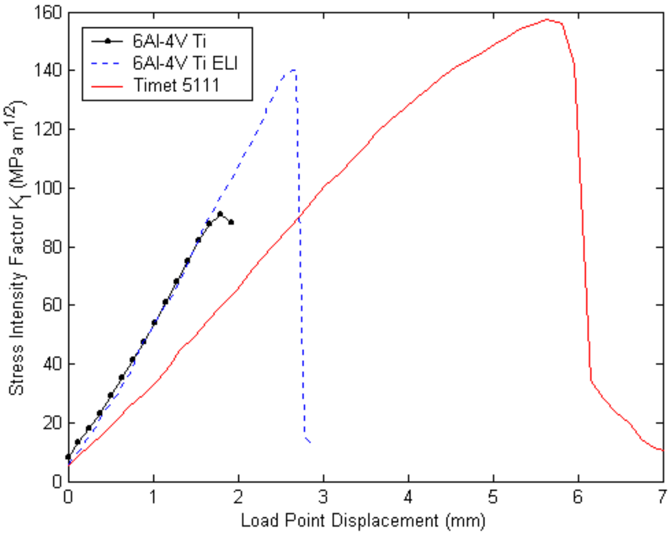

Figure 4.6: Quasistatic stress intensity K_I versus load point displacement for side-grooved 6Al-4V Ti, 6Al-4V Ti ELI, and Timetal 5111 specimens.

The plot shows that the 6Al-4V Ti and 6Al-4V Ti ELI materials have identical slopes but the latter material fails at a stress intensity 56% higher than the former. The Timetal 5111 is 72% tougher than the 6Al-4V Ti, and its trace has a different slope than the other two alloys. The same slopes are observed in all tests. Since all three materials have nominally the same elastic properties, the reason for the different slopes must be due to differences in plastic behavior as the plastic zone develops at the crack tip.

Energy is proportional to area under the K_I-displacement line. Thus the plot shows that there is sizeable difference between the amount of energy that the materials can withstand before crack initiation. The 6Al-4V Ti ELI and Timetal 5111 have area about twice and six times the area compared to that under the 6Al-4V Ti trace.

4.3.4 Examination of Fracture Surfaces

The images in this section are of the entire fracture surfaces of several representative specimens. The images were taken with a 35 mm camera under lighting such that flat fracture is light gray, while shear lips are angled away from the light source when possible and appear darker. In all images the EDM notch is on right and appears smooth and generally dark. Adjacent to the EDM notch the fatigue crack is visible.

Figures 4.7-4.9 show fracture surfaces of three 6Al-4V Ti specimens. The first two images are of specimens without side-grooves, the former loaded quasistatically and the latter dynamically. The fracture surface from the quasistatic test shows a progression to nearly 100% side-grooves within about a specimen thickness distance from the fatigue crack. Dynamically loaded, the material develops much smaller shear lips. In this case the shear lip on the bottom edge is nearly non-existent. The third image shows the fracture surface of a dynamically loaded side-grooved specimen. The fracture is completely flat. In all cases the fracture surfaces have a relatively smooth "satin" appearance.

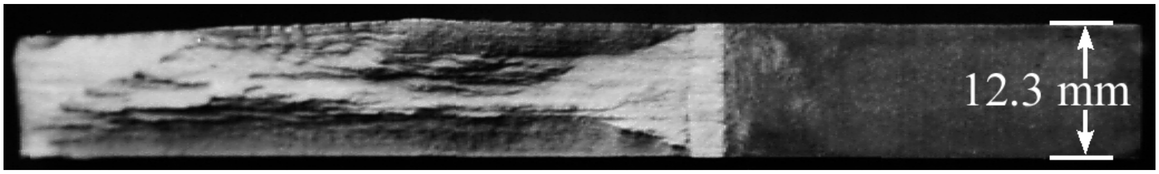

Figure 4.7: Fracture surface of 6Al-4V Ti specimen loaded quasistatically.

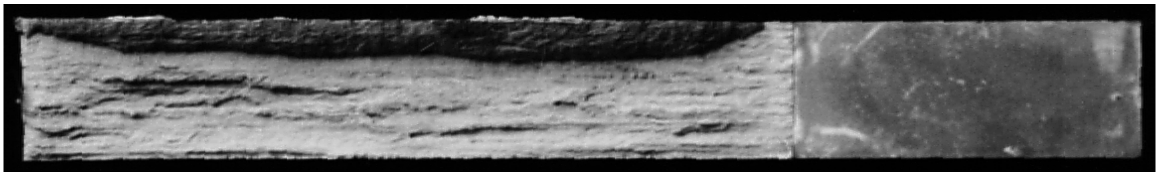

Figure 4.8: Fracture surface of 6Al-4V Ti specimen loaded dynamically.

Figures 4.10 and 4.11 show fracture surfaces of two 6Al-4V Ti ELI specimens. Both were dynamically loaded, with the latter having side-grooves. The former specimen quickly develops nearly

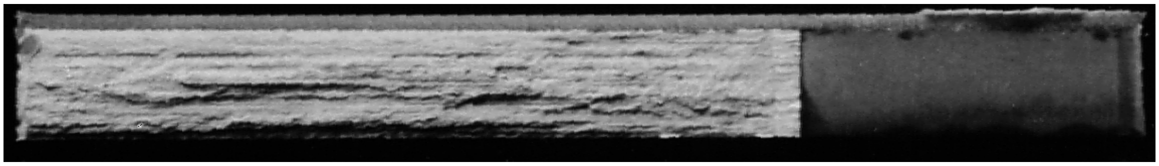

Figure 4.9: Fracture surface of side-grooved 6Al-4V Ti specimen loaded dynamically.

100% side-grooves. The specimen with side-grooves has slight curvature of the fracture surface. Both fracture surfaces appear finely granular and unlike those of the 6Al-4V Ti material. Fracture surfaces from quasistatically loaded specimens look macroscopically the same.

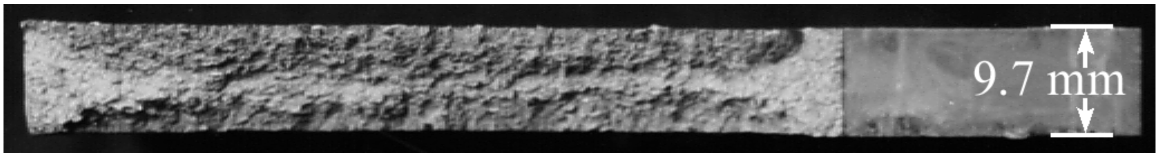

Figure 4.10: Fracture surface of 6Al-4V Ti ELI specimen loaded dynamically.

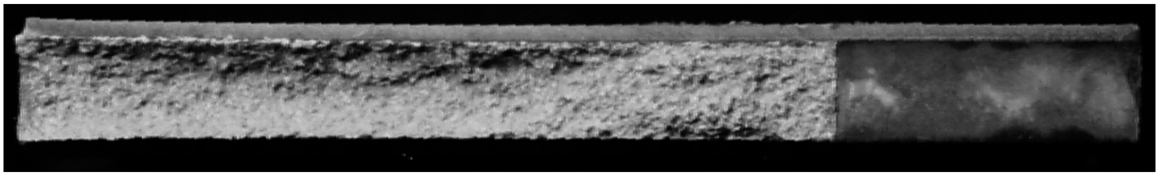

Figure 4.11: Fracture surface of side-grooved 6Al-4V Ti ELI specimen loaded dynamically.

Figures 4.12-4.14 show fracture surfaces of three Timetal 5111 specimens. The first two images are of quasistatically loaded specimens without and with side-grooves respectively. The specimen without side-grooves develops 100% side-grooves within a distance of a specimen thickness of the fatigue crack. The specimen with side-grooves exhibits curvature but no shear lips. The third figure is of a dynamically tested side-grooved specimen which has a fracture surface with slightly less curvature than its quasistatically tested counterpart. All fracture surfaces exhibit a granular appearance that is much coarser than those of the 6Al-4V Ti ELI material.

Figure 4.12: Fracture surface of Timetal 5111 specimen loaded quasistatically.

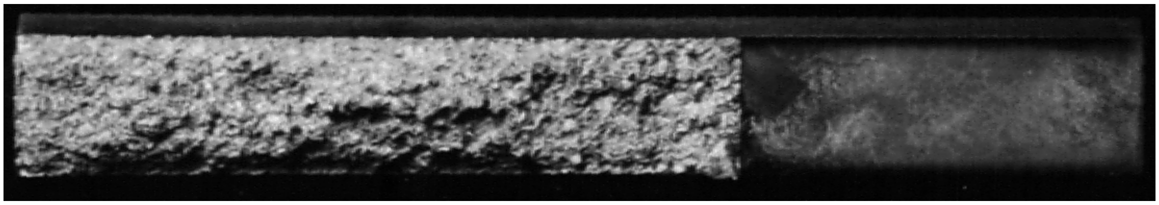

Figure 4.13: Fracture surface of side-grooved Timetal 5111 specimen loaded quasistatically.

4.3.5 Other Results for 6Al-4V Titanium

Figure 4.15 shows the dynamic stress intensity factor versus crack velocity for the 6Al-4V Ti for two tests with drop weight tup impact speeds of 3 and 9 m/s. This data is available only from the CGS measurement technique. Consequently a plot of this type could not be made for either of the other two materials though strain gage data from tests of these materials indicate that their crack velocities are at the lower end of the same 120-320 m/s range.

Throughout the velocity range observed, the fracture toughness remains essentially constant for the 9 m/s impact speed test. For the slower 3 m/s impact speed test the toughness decreases slightly as velocity increases, with an outlying point at 300 m/s. Overall the critical stress intensity for a

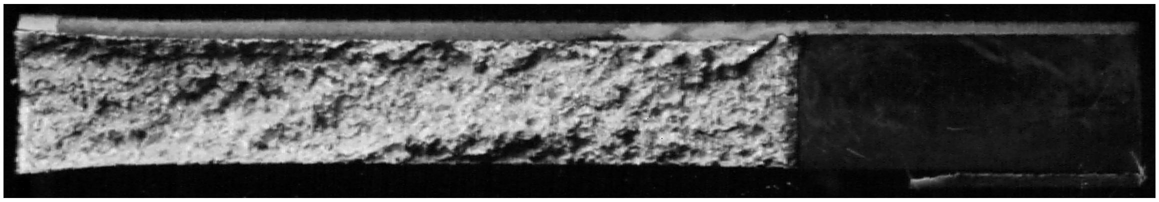

Figure 4.14: Fracture surface of side-grooved Timetal 5111 specimen loaded dynamically.

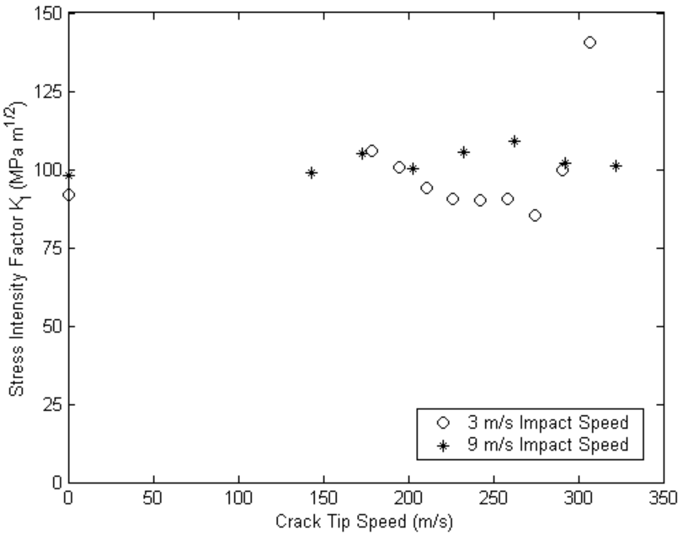

Figure 4.15: Stress intensity K_{ID} versus crack velocity for 6Al-4V Ti.

moving crack appears roughly the same as that for the dynamically loaded initiating (zero velocity) crack. Because the velocities observed are less than 11% of the material's shear wave speed, little variation of propagation toughness with velocity is expected.

4.3.6 Other Data for 6Al-4V Ti ELI

SEM microscopy was performed on fracture surfaces of ELI. Figures 4.16 and 4.17 show regions near the crack tip from specimens loaded quasistatically and dynamically, respectively. While both look similar, the feature sizes from the dynamically loaded material are smaller than the same for the quasistatically loaded material.

Figures 4.18 and 4.19 show regions near the crack tip under higher magnification from specimens loaded quasistatically and dynamically, respectively. Again the dynamic fracture surface has smaller length scales and more irregular pattern than that from the quasistatic fracture surface.

Figure 4.20 shows 6Al-4V Ti ELI yield and ultimate stress versus strain rate. The material exhibits strain rate hardening.

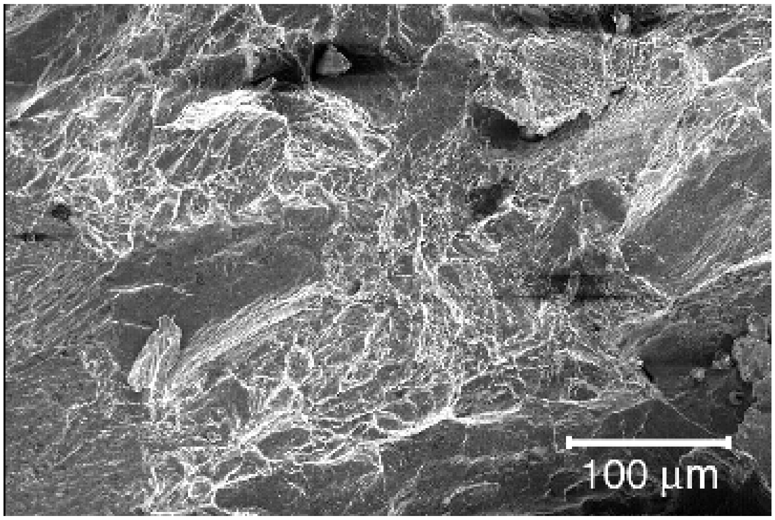

Figure 4.16: Fracture surface of quasistatically loaded for 6Al-4V Ti ELI.

Figure 4.21 shows two stress-strain curves at different loading rates. At both rates very little strain hardening is observed.

4.4 Conclusions

The application of quasistatic global measurement technique to determine quasistatic stress intensity factors and the optical methods of CGS and COD as well as strain gages to determine dynamic stress intensity factors have been successfully employed to measure the fracture properties of three titanium alloys. The more ductile 6Al-4V Ti ELI and Timetal 5111 alloys have significantly higher initiation toughnesses than the commercial grade 6Al-4V Ti alloy. None of the materials showed a significant dependence of plane strain initiation toughness on loading rate over the range generated by drop weight impact loading.

Furthermore the 6Al-4V Ti fracture toughness was not found to significantly depend on crack velocity for moving cracks over the velocity range generated by drop weight loading.

Both the 6Al-4V Ti ELI and Timetal 5111 fracture surfaces macroscopically had coarse granular structure unlike the 6Al-4V Ti which had a more smooth texture.

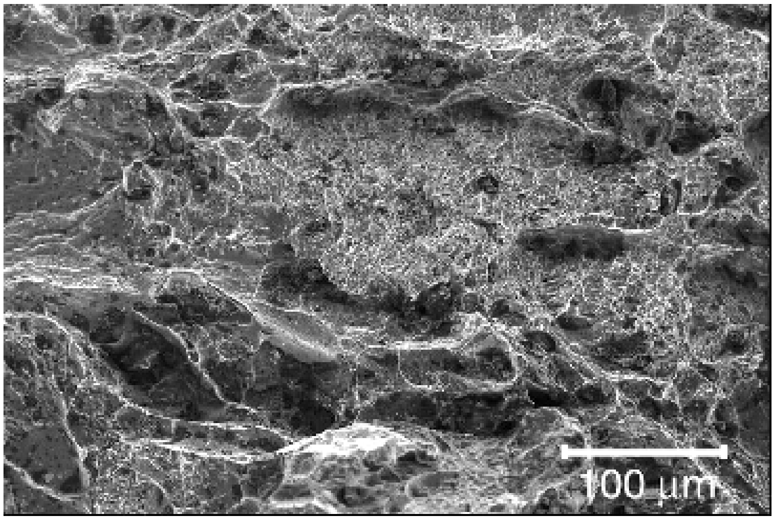

Figure 4.17: Fracture surface of dynamically loaded for 6Al-4V Ti ELI.

Further understanding of these materials' behavior could be obtained using different loading techniques to explore higher and lower dynamic loading rates than was possible in the drop weight tower system. Also repeating tests in the same loading range could be done to establish the variation in property values and measurement techniques values.

Regarding stress intensity measurements, the techniques employed were successful in determining values for these difficult engineering materials over a range of loading rates.

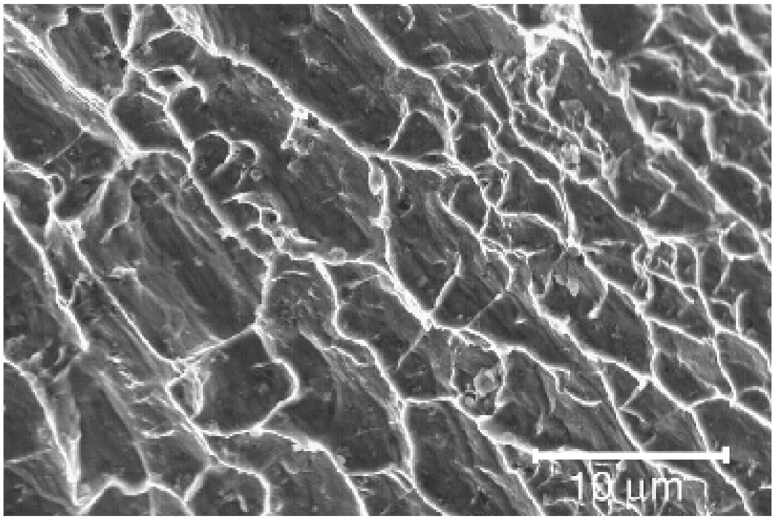

Figure 4.18: Fracture surface of quasistatically loaded for 6Al-4V Ti ELI.

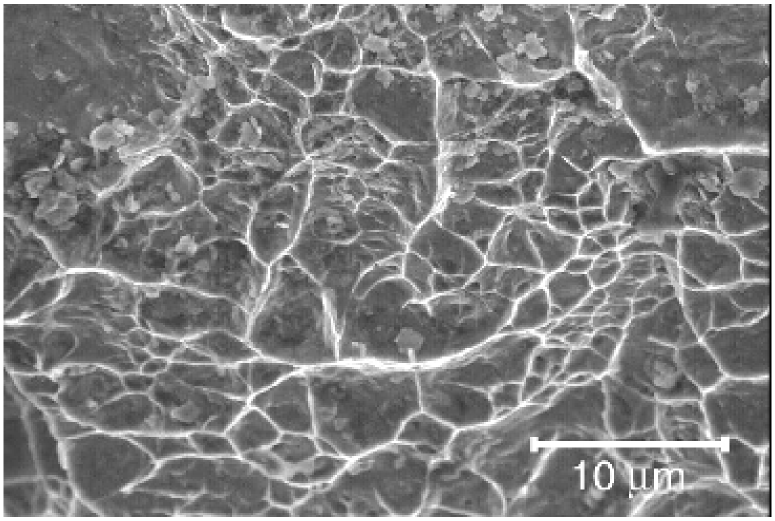

Figure 4.19: Fracture surface of dynamically loaded for 6Al-4V Ti ELI.

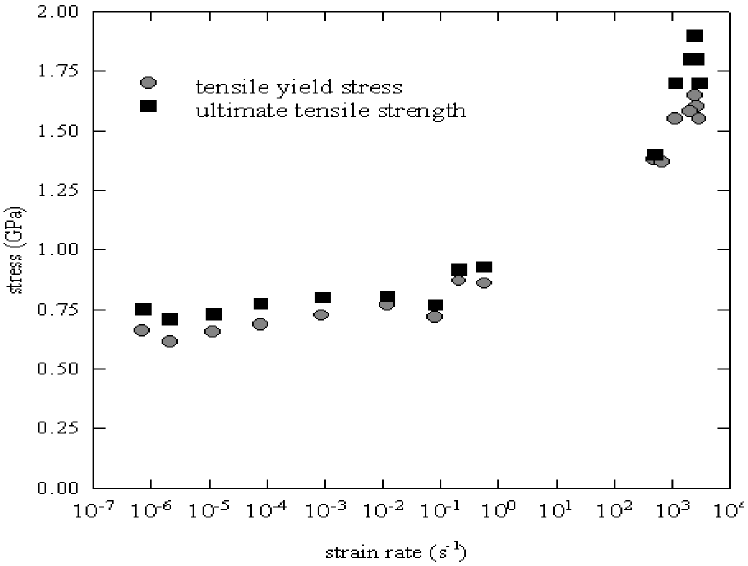

Figure 4.20: 6Al-4V Ti ELI yield and ultimate stress versus strain rate.

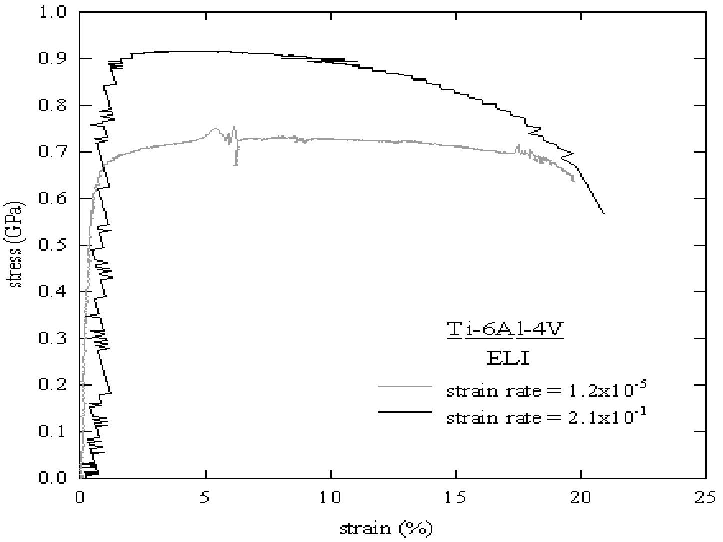

Figure 4.21: Stress-strain curves for 6Al-4V Ti ELI.

Appendix A

Comparison of Dynamic Stress Intensity Factor Measurement Techniques

A.1 Comparison of Techniques

Below is a comparison of three techniques for measuring dynamic stress intensity factors: Coherent Gradient Sensing (CGS), Crack Opening Displacement (COD) and strain gage measurement.

	CGS	COD	Strain Gage
Measurement Sensitivity:	Gradients of out-of-plane displacement (reflection CGS). Stress-induced geometric and optical property changes (transmission CGS).	Crack opening profile.	In-plane strains.
Model Used:	LEFM	EPFM	LEFM
Can Obtain:	K_I^d, K_{II}^d, Higher order terms, (insensitive to T stress), crack tip location, and fitting error.	K_I^d only. No indication of error.	Any terms and/or crack tip location. Number of items of data less than or equal to the number of strain gages.
Region Used:	Full field measurements outside plastic zone.	Measurements inside plastic zone.	“Point” measurements outside plastic zone.
Specimen Constraints:	Planar — No side-grooves.	Side-grooves acceptable. Allows testing of more ductile materials.	Planar — No side-grooves.
Specimen Preparation:	Must be optically flat with mirror finish prior unless transparent.	None required.	None necessary other than mounting the strain gages.
Equipment Required	Laser, high speed camera, diffraction gratings, and optics.	Laser, high speed camera, and some optics.	Strain gage electronics and high speed data acquisition system.
Data Analysis	Time consuming fringe digitizing and complex though somewhat automated analysis.	Easier and more intuitive analysis than CGS. Some techniques may be ad hoc.	May require linear algebra for multiple gages, but only a multiplicative constant for single gage.

Table A.1: Comparison of three different dynamic stress intensity factor measurement techniques.

Appendix B

CGS Data Fitting in the Three-Dimensional Zone

B.1 Overview

This appendix gives the methodology and results for calculating the function $f(r, \theta)$ which is used to convert fringe numbers m_{3d} digitized from reflection CGS fringe patterns to fringe numbers m_{2d} which are associated with a two-dimensional plane stress K_I field. Conversion must be from m_{3d} to m_{2d} inside the three-dimensional zone ($r/h < 0.5$) to allow the fitting of crack tip asymptotic term(s) to determine fracture toughness. The conversion factor $f(r, \theta)$ is given by

$$f(r, \theta) = \frac{m_{2D}(r, \theta)}{m_{3D}(r, \theta)} \tag{B.1}$$

While more complicated techniques might be developed to handle mixed mode crack tip fields (see referring section 3.6.3), this chapter describes the pure mode I case only. The denominator of equation (B.1) is obtained from experimental measurement of a stationary mode I crack. The numerator is obtained from a K_I field, the universal leading term of the analytical crack tip asymptotic solution.

B.2 Calculation of Conversion Factor

Experimental measurements of out-of-plane surface displacement near stationary crack tips in different elastic materials performed by Nakamura and Parks [31] were meticulously fitted by Pfaff [34] to within measurement error. His fit of the $u_3(r/h, \theta)$-field for a three-dimensional crack is given by

$$\begin{aligned}
\frac{-u_3\big|_{x_3=h/2}}{\frac{\nu}{E}K_I\sqrt{h}} &\approx f_a\left(\frac{r}{h},\theta\right)\left[1+f_b\left(\nu,\frac{r}{h},\theta\right)\right] && \text{(B.2)}\\
f_a\left(\frac{r}{h},\theta\right) &= \left[\left(1-e^{-c_1\sqrt{2\pi}\sqrt{r/h}[1+\pi r/h]}\right)\frac{1}{\sqrt{2\pi}\sqrt{r/h}}\right] f_0\left(\frac{r}{h}\right)\left[\cos\frac{\theta}{2}+f_1\left(\frac{r}{h},\theta\right)\right] && \text{(B.3)}\\
f_0\left(\frac{r}{h}\right) &\approx \left(1-c_2e^{-f_2(r/h)}\right)\left(1+c_4e^{-c_6(r/h-c_5)^2}\right) && \text{(B.4)}\\
-\hat{u}_0 &\equiv -\left[\left(u_3\Big|_{\substack{r=0\\x_3=h/2}}\right)\Big/\left(\frac{\nu}{E}K_I\sqrt{h}\right)\right]_{\nu=3/10}; \qquad c_2\equiv 1-\frac{1}{c_1}\left[-\hat{u}_0\right]; && \text{(B.5)}\\
\left[-\hat{u}_0\right] &\approx \frac{187}{200}; \qquad c_1\approx\frac{\pi-1}{2}; && \text{(B.6)}\\
c_4 &\approx \frac{33}{2000}; \qquad c_5\approx\frac{3}{5}; \qquad c_6\approx 10 && \text{(B.7)}\\
f_2\left(\frac{r}{h}\right) &= \left(\frac{1-c_2}{c_2}\right)\left[\frac{1}{2}c_1\sqrt{2\pi}\sqrt{r/h}+\left[-1+\left(\frac{1}{6}+\frac{1}{4}\left(\frac{1-c_2}{c_2}\right)\right)c_1^2\right]\pi\frac{r}{h}\right. && \text{(B.8)}\\
&\quad \left.+\,c_7\frac{r}{h}+f_3\left(\frac{r}{h}\right)\right]\\
c_7 &\approx 2 \qquad f_3\left(\frac{r}{h}\right)\approx\left[70\left(\frac{r}{h}\right)^2+\left(\frac{177}{8}\frac{r}{h}\right)^7\right] && \text{(B.9)}\\
f_1\left(\frac{r}{h},\theta\right) &= \left(1-\cos\frac{\theta}{2}\right)e^{-g_1(r/h)g_2(r/h,\theta)} && \text{(B.10)}\\
g_1\left(\frac{r}{h}\right) &= \frac{117}{25}\left(\frac{r}{h}\right)^{\frac{3}{5}}\left(1+\frac{9}{50}e^{-[4(r/h-1/2)]^4}\right) && \text{(B.11)}\\
g_2\left(\frac{r}{h},\theta\right) &\approx \left[1-\frac{2}{33}\left(|\theta|-\frac{2\pi}{9}\right)|\theta|\left(\frac{9}{10}-\frac{r}{h}\right)\right] && \text{(B.12)}\\
f_b\left(\nu,\frac{r}{h},\theta\right) &= \left\{\left[\frac{4}{159}\left(\frac{10}{3}\left(\frac{3}{10}-\nu\right)\right)-\frac{2}{55}\left(\frac{10}{3}\left(\frac{3}{10}-\nu\right)\right)^6\right]e^{-\frac{1}{2}r/h}\right\} && \text{(B.13)}\\
&\quad \left(1+f_c\left(\nu,\frac{r}{h},\theta\right)\right)
\end{aligned}$$

where h is specimen thickness, ν and E are the material's Poisson's ratio and Young's modulus respectively. f_a is the deformation field for $\nu = 3/10$ and f_b is the correction for different Poisson's ratio. f_c is "an as yet to be determined function."

To facilitate taking partial derivatives, u_3 was fit with polynomials. This was accomplished by fixing $\theta = \hat{\theta} = 0, 0.1, 0.2, ...3.1$ and for each $\hat{\theta}$ fitting u_3 sampled at $r/h = 0.01, 0.02, 0.03, ...0.55$ with a fourth order polynomial. Due to mode I symmetry ($u_3(r,\theta) = u_3(r,-\theta)$) performing calculations for $0 \leq \theta \leq \pi$ is sufficient. This gives

$$\frac{-\hat{u}_3(r/h,\theta)\big|_{\theta=\hat{\theta}}}{\frac{\nu}{E}K_I\sqrt{h}} = c_0(\hat{\theta}) + c_1(\hat{\theta})\left(\frac{r}{h}\right) + c_2(\hat{\theta})\left(\frac{r}{h}\right)^2 + c_3(\hat{\theta})\left(\frac{r}{h}\right)^3 + c_4(\hat{\theta})\left(\frac{r}{h}\right)^4 . \tag{B.14}$$

The $c_i(\hat{\theta})$ are in turn fit with third order polynomials over the domain $0 < \hat{\theta} < \pi$ to obtain the following:

$$c_0(\theta) = 0.939111 + 0.0114101\,\theta - 0.0486648\,\theta^2 + 0.00991056\,\theta^3 \tag{B.15}$$

$$c_1(\theta) = -1.02950 + 0.281207\,\theta - 1.10198\,\theta^2 + 0.178782\,\theta^3 \tag{B.16}$$

$$c_2(\theta) = 0.981826 - 1.69527\,\theta + 5.77848\,\theta^2 - 1.12167\,\theta^3 \tag{B.17}$$

$$c_3(\theta) = -1.60788 + 3.52212\,\theta - 11.5956\,\theta^2 + 2.39841\,\theta^3 \tag{B.18}$$

$$c_4(\theta) = 1.53774 - 2.51373\,\theta + 8.27263\,\theta^2 - 1.75178\,\theta^3 . \tag{B.19}$$

The end result is a representation of u_3 in the form

$$\frac{-\hat{u}_3(r/h,\theta)}{\frac{\nu}{E}K_I\sqrt{h}} \approx c_0(\theta) + c_1(\theta)\left(\frac{r}{h}\right) + c_2(\theta)\left(\frac{r}{h}\right)^2 + c_3(\theta)\left(\frac{r}{h}\right)^3 + c_4(\theta)\left(\frac{r}{h}\right)^4 . \tag{B.20}$$

This construction, performed with $\nu = 1/3$, was found to agree well (within 2%) with the Pfaff fit for $0 < \nu < 0.5$. As a further check the polynomial fit was also compared to finite element results by Krishnaswamy *et al.* [28]. The two agree well to a nearly constant offset (less than 10%), which is not worrisome because only partial derivatives of the function are used.

After substituting $r = \sqrt{x_1^2 + x_2^2}$ and $\theta = |\tan^{-1} x_2/x_1|$, partial derivatives of $\hat{u}_3$ are taken with respect to x_1/h and x_2/h:

$$
\begin{aligned}
\mathcal{M}_1(r/h,\theta) = \frac{-\sqrt{h}}{\frac{\nu}{E}K_I}\frac{\partial \hat{u}_3}{\partial x_1} \quad = \quad & \big[-0.0114101\sin\theta + 0.0973296\,\theta\sin\theta \\
& -0.0297317\,\theta^2\sin\theta\big]\left(\frac{r}{h}\right)^{-1} \\
& +\big[-1.02950\cos\theta - 0.281207\sin\theta + \theta(0.281207\cos\theta + 2.20396\sin\theta) \\
& -\theta^2(1.10198\cos\theta + 0.536345\sin\theta) + 0.178782\,\theta^3\cos\theta\big] \\
& +\big[1.96365\cos\theta + 1.69527\sin\theta - \theta(3.39055\cos\theta + 11.5570\sin\theta) \\
& +\theta^2(11.5570\cos\theta + 3.36502\sin\theta) - 2.24335\,\theta^3\cos\theta\big]\left(\frac{r}{h}\right) \\
& +\big[-4.82365\cos\theta - 3.52212\sin\theta + \theta(10.5664\cos\theta + 23.1912\sin\theta) \\
& -\theta^2(34.7869\cos\theta + 7.19522\sin\theta) + 7.19522\,\theta^3\cos\theta\big]\left(\frac{r}{h}\right)^2 \\
& +\big[6.15098\cos^3\theta + 2.51373\cos^2\theta\sin\theta + 6.15098\cos\theta\sin^2\theta \\
& +2.51373\sin^3\theta - \theta(10.0549\cos^3\theta + 16.5453\cos^2\theta\sin\theta \\
& +10.0549\cos\theta\sin^2\theta + 16.5453\sin^3\theta) + \theta^2(33.0905\cos^3\theta \\
& +5.25535\cos^2\theta\sin\theta + 33.0905\cos\theta\sin^2\theta + 5.25535\sin^3\theta) \\
& -7.00713\theta^3(\cos^3\theta + \cos\theta\sin^2\theta)\big]\left(\frac{r}{h}\right)^3
\end{aligned}
\tag{B.21}
$$

$$\begin{aligned}
\mathcal{M}_2(r/h,\theta) = \frac{-\sqrt{h}}{\frac{\nu}{E}K_I}\frac{\partial \hat{u}_3}{\partial x_2} &= [0.0114101\cos\theta - 0.0973296\,\theta\cos\theta \\
&\quad + 0.0297317\,\theta^2\cos\theta]\left(\frac{r}{h}\right)^{-1} \\
&\quad + [0.281207\cos\theta - 1.02950\sin\theta + \theta(-2.20396\cos\theta + 0.281207\sin\theta) \\
&\quad + \theta^2(0.536345\cos\theta - 1.10198\sin\theta) + 0.178782\theta^3\sin\theta] \\
&\quad + [-1.69527\cos\theta + 1.96365\sin\theta + \theta(11.557\cos\theta - 3.39055\sin\theta) \\
&\quad + \theta^2(-3.36502\cos\theta + 11.557\sin\theta) - 2.243335\theta^3\sin\theta]\left(\frac{r}{h}\right) \\
&\quad + [3.52212\cos\theta - 4.82365\sin\theta + \theta(-23.1912\cos\theta + 10.5664\sin\theta) \\
&\quad + \theta^2(7.19522\cos\theta - 34.7869\sin\theta) + 7.19522\,\theta^3\sin\theta]\left(\frac{r}{h}\right)^2 \\
&\quad + [-2.51373\cos\theta + 6.15098\sin\theta + \theta(16.5453\cos\theta - 10.0549\sin\theta) \\
&\quad + \theta^2(-5.25535\cos\theta + 33.0905\sin\theta) - 7.00713\,\theta^3\sin\theta]\left(\frac{r}{h}\right)^3 .
\end{aligned} \tag{B.22}$$

Using the CGS interference condition for reflection and chain rule gives

$$\begin{aligned}
\frac{\partial u_3}{\partial \hat{x}} &= \frac{\partial u_3}{\partial x_1}\frac{\partial x_1}{\partial \hat{x}} + \frac{\partial u_3}{\partial x_2}\frac{\partial x_2}{\partial \hat{x}} \\
&= \frac{\partial u_3}{\partial x_1}\cos\phi + \frac{\partial u_3}{\partial x_2}\sin\phi \\
&= \frac{mp}{2\Delta}
\end{aligned} \tag{B.23}$$

where ϕ is the angle of $\underset{\sim}{\hat{e}}$ with respect to $\underset{\sim}{e}_1$. Thus m_{3D} is given by

$$m_{3d} = -\frac{2\Delta}{p}\frac{\nu}{E}\frac{K_I}{\sqrt{h}}\left(\mathcal{M}_1(r/h,\theta)\cos\phi + \mathcal{M}_2(r/h,\theta)\sin\phi\right) \tag{B.24}$$

and m_{2d} is obtained by using the leading term of the asymptotic expansion for a stationary crack:

$$m_{2d} = \frac{\Delta h}{p}\frac{\nu}{E}\frac{K_I}{\sqrt{2\pi}r^{3/2}}\left(\cos\phi\cos\frac{3\theta}{2} + \sin\phi\sin\frac{3\theta}{2}\right) \tag{B.25}$$

so

$$f(r,\theta) = \frac{m_{2D}(r,\theta)}{m_{3D}(r,\theta)} = \left|\frac{-1}{2\sqrt{2\pi}\left(\frac{r}{h}\right)^{3/2}}\frac{\cos\left(\phi - \frac{3\theta}{2}\right)}{\left(\mathcal{M}_1(r/h,\theta)\cos\phi + \mathcal{M}_2(r/h,\theta)\sin\phi\right)}\right| = \hat{f}(r/h,\theta)\,. \tag{B.26}$$

The conversion factor is a function of r/h even though neither m_{2d} nor m_{3d} are. The function is limited to stationary cracks because m_{3d} is obtained from a stationary crack. The conversion factor can be assessed experimentally using any interferograms which has fringes inside and outside the three-dimensional zone. This is done by comparing the value of K_I obtained from data inside the three-dimensional zone using the conversion factor to K_I obtained using only data outside the three-dimensional zone in the usual manner.

A psuedocolor plot of $\hat{f}(r/h, \theta)$ for $\phi = 0$ is given in Figure B.1. The conversion function goes to infinity as radius goes to zero (m_{2d} goes to infinity) and for θ in the vicinity ±60° (where m_{3d} goes to zero). A third region of interest is along the crack face where m_{2d} tends to zero faster than m_{3d}. To minimize unduly large error contributions from few points, one filters out data inside some radius (typically $0.15\,h$) and does not use data near the fringe lobe boundaries (in this case $\theta = \pm 60°$ and 180° where the fitting equation's singular term has a $\cos 3\theta/2$ in the denominator). These precautions eliminate the troublesome regions.

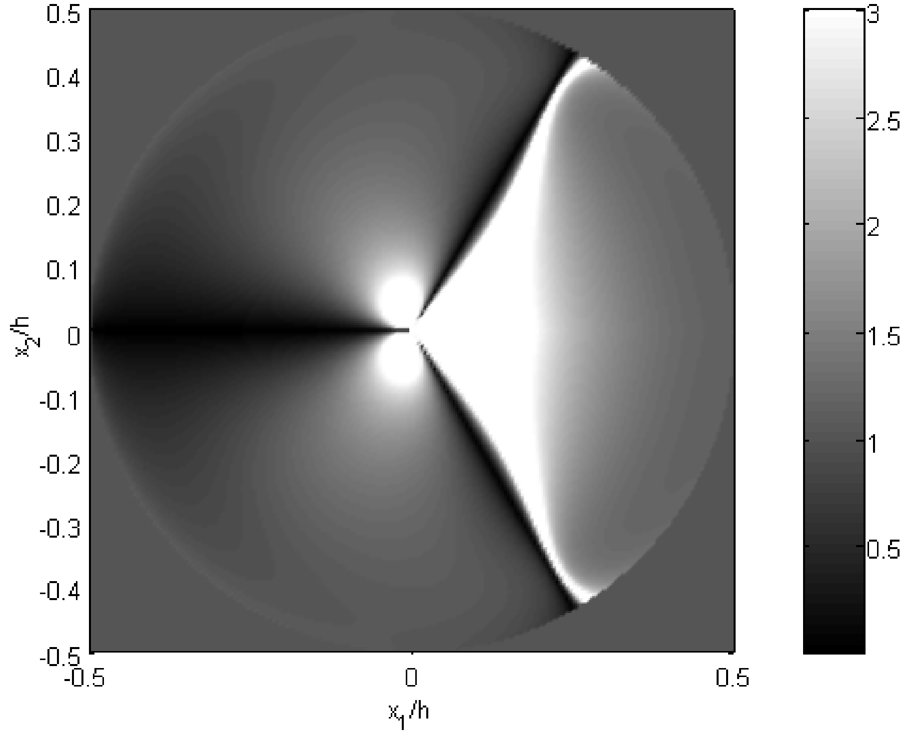

Figure B.1: Psuedocolor plot of $\hat{f}(r/h, \theta) = m_{2D}(r, \theta)/m_{3D}(r, \theta)$ for mode I with $\phi = 0$.

B.3 Comparison of K_I-Field and Three-Dimensional Crack Field Inside the 3-D Zone

Having equations for u_3 for both a three-dimensional crack tip zone and for the leading term of the asymptotic solution (K_I field), it is easy and useful to compare the two for $r/h < 0.5$. The asymptotic u_3-field is obviously singular and assumes plane stress conditions. While both of these assumptions are good outside the three-dimensional zone ($r > h/2$) and make field equations possible for stress, strain, and displacement, both assumptions break down completely at the crack tip where finite values and plane strain conditions are expected.

Figure B.2 shows contour plots of normalized out-of-plane displacement $u_3 E\sqrt{2\pi}/(K_I \nu \sqrt{h})$ inside the three-dimensional zone. The crack tip is located at the origin with the crack to the left. The contour nearest $(-.5, 0)$ is -0.1 with contours decreasing by 0.1 as the origin (crack tip) is approached. Both plots match well at the perimeter, or boundary, of the three-dimensional zone as expected. However, as the crack tip is approached, the contour density increases to infinity at the crack tip for the K_I-field (only contours to -3.0 are displayed), while the largest displacement contour for the three-dimensional crack is -2.2.

Because CGS is sensitive to gradients of u_3, it is useful to compare contour plots of these fields. Figure B.3 shows contour plots of normalized gradient of out-of-plane displacement in the x_1 direction $(\partial u_3/\partial x_1)(2E\sqrt{2\pi h})/(K_I \nu)$ inside the three-dimensional zone. The contour immediately right of the crack tip $(0, 0)$ is 4 with contours decreasing by 1 to -8 for the innermost contour of the rear lobe(s). Again both plots match well at the perimeter. Note that for the asymptotic field as one approaches the crack tip along $\theta = \pm 60^\circ$, the fringe density goes to infinity indicating infinite curvature. For the three-dimensional field the curvature in the same region is high but measurable. This curvature may be used to determine K_I as described in section B.4.

Figure B.4 shows contour plots of normalized gradient of out-of-plane displacement in the x_2 direction. For the K_I field, the magnitude of the innermost front contour is 4, with magnitude

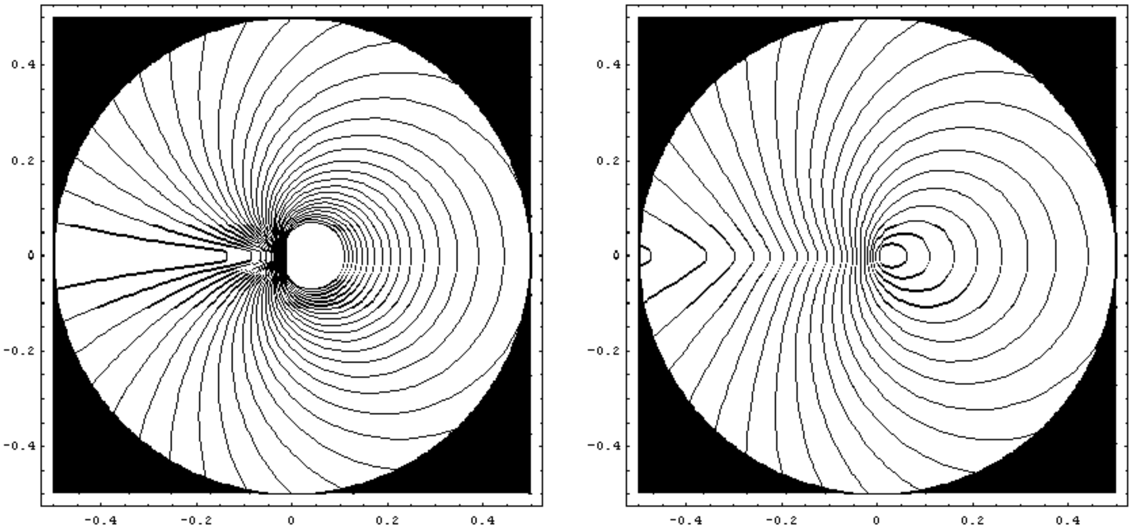

Figure B.2: Normalized u_3 displacement inside three-dimensional zone for K_I-field (left) and three-dimensional crack (right).

decreasing to 0 at $\theta = \pm 120^\circ$ and increasing to 8 for the innermost contour to the rear at of the crack tip. The sign[1] of the contours is positive for $0^\circ < \theta < 120^\circ$ and $-180^\circ < \theta < -120^\circ$, and negative elsewhere. The contours for the three-dimensional crack are similar, but the innermost rear lobe only has magnitude of 5. Again both plots match well at the perimeter.

B.4 Obtaining K_I from Curvature

As mentioned in the previous section, K_I can be determined from CGS fringe patterns by measuring curvature or $\partial^2 u_3/\partial x_1^2$. This technique is limited to stationary mode I cracks and only utilizes data around the boundary between the front and side lobes where sufficient fringe density exists. CGS shearing must also be in the x_1 direction. This technique's strength is that it can be used to obtain K_I in situations where it is impossible to obtain usable fringes away from the crack tip due to a material's low fracture toughness or loading wave interference.

This method is presented by way of analytical extension of three-dimensional zone conversion

---

[1] Recall that only $|\theta|$ was needed for previous calculations.

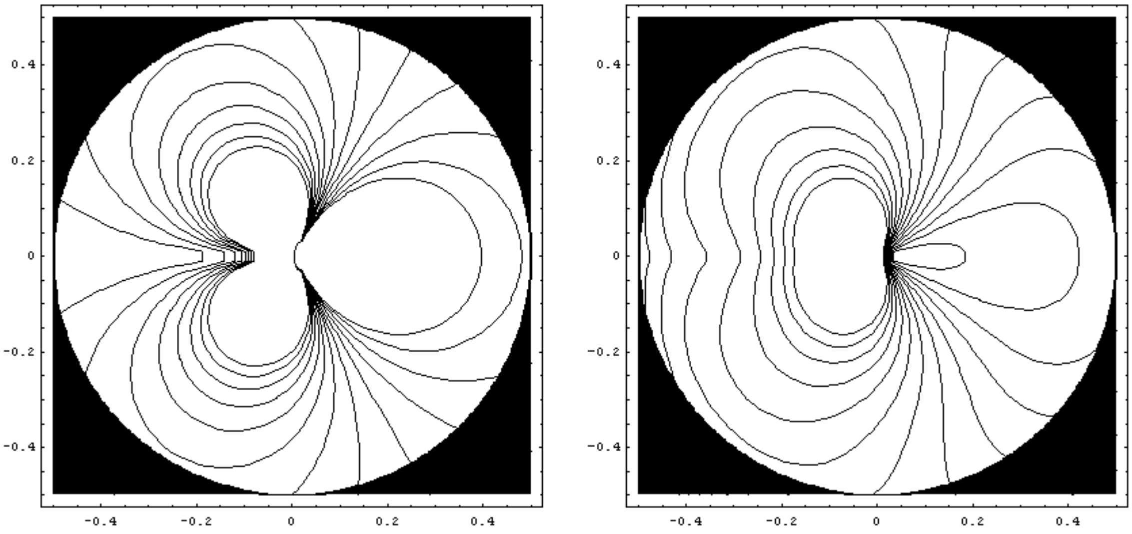

Figure B.3: Normalized gradient of u_3 in the x_1 direction inside three-dimensional zone for K_I-field (left) and three-dimensional crack (right).

factor calculations. While the three-dimensional zone conversion factor has been employed with success, this method has not yet been systematically tested. Since it derives from the same fields as the successfully used conversion factor, it is expected to work equally well.

The goal is to find normalized K_I as a function of curvature, or gradient of fringe number:

$$\hat{K}_I = \frac{K_I \nu \Delta}{pE\sqrt{t}} \propto h \frac{\partial^2 u_3}{\partial x_1^2} \propto h \frac{\partial m}{\partial x_1} \tag{B.27}$$

where Δ is the distance between the two diffraction gratings, p is grating pitch, and m is fringe number. Since CGS only measures slope and not curvature,

$$\frac{\partial m}{\partial x_1} \approx \frac{(\Delta m)}{(\Delta x_1)} \tag{B.28}$$

where here Δ indicates the finite difference of the following variable.

With the three-dimensional field contour plot in Figure B.4 in mind, the goal is to find the proportionality function $g(\Delta x_1/h, x_2/h)$ such that

$$\hat{K}_I = h \frac{\Delta m}{\Delta x_1} g(\Delta x_1/h, x_2/h) \, . \tag{B.29}$$

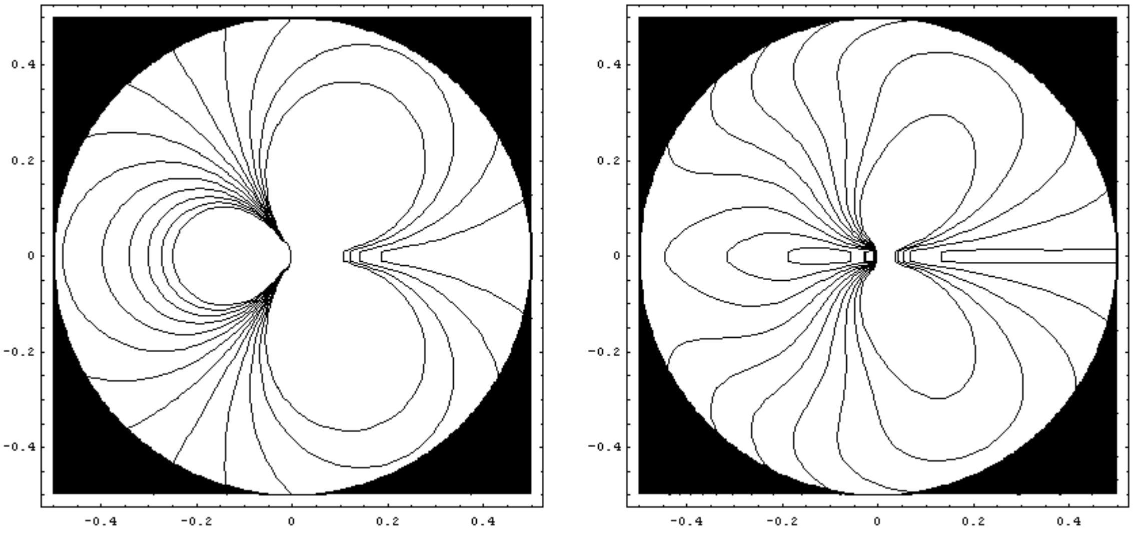

Figure B.4: Normalized gradient of u_3 in the x_2 direction inside three-dimensional zone for K_I-field (left) and three-dimensional crack (right).

Again the region of interest is limited to the fringe concentration between the front and rear lobes adjacent to the crack tip as this is where the fringe patterns can be best employed to obtain curvature.

Difficulties arise because the curvature isn't constant with respect to x_1 and only finite differences are available from the CGS interferograms. Figure B.5 shows normalized radius of curvature $(1/(2\partial\mathcal{M}_1/\partial(x_1/h)) = \hat{g}(x_1/h, x_2/h))$ versus x_1/h for fixed $x_2/h = 0.25$. Furthermore, the shape of the curvature versus x_1/h plot changes with x_2/h. Note that $\hat{g}(x_1/h, x_2/h)$ is the normalized radius of curvature at a point. The finite difference constraint requires $g(\Delta x_1/h, x_2/h)$ to be used, which is the average of $\hat{g}$ over some $\Delta x_1/h$.

To find $g(\Delta x_1/h, x_2/h)$ a numerical approach is employed to calculate many cases which are then fitted for generality. For each offset ($x_2/h = 0.05$ to 0.491 in increments of 0.049) the minimum radius of curvature was found. This minimum radius ρ was multiplied in turn by $\varphi = 1.1, 1.7, 2.3, 2.9$, and 3.5. Next $\Delta x_1/h$ is obtained for each φ by numerically finding the two roots (a, b) of $\hat{g} - \varphi\rho = 0$

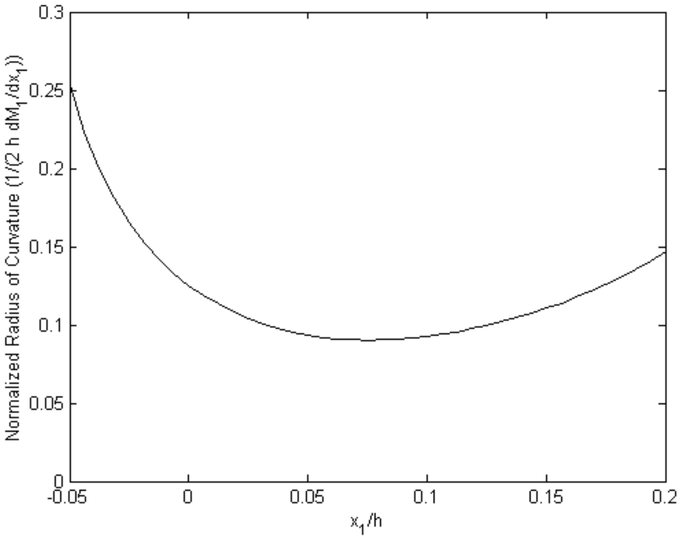

Figure B.5: Normalized radius of curvature from three-dimensional field along $x_2/h = 0.25$.

and taking their difference $|b - a|$. Finally g is given by

$$g(\Delta x_1/h, x_2/h) = \frac{1}{|b-a|}\int_a^b \hat{g}(x_1/h, x_2/h)d(x_1/h)\,. \tag{B.30}$$

Using the above procedure 50 values of $g(\Delta x_1/h, x_2/h)$ were obtained for cases given in Figure B.6.

For generality, the 50 cases were fitted by the following:

$$\begin{aligned} g(\Delta x_1/h, x_2/h) &= -0.0411106 - 0.0699268(\Delta\hat{x}_1) + 1.66892(\Delta\hat{x}_1)^2 \\ &\quad +1.89617(\Delta\hat{x}_1)^3 + 1.18274\hat{x}_2 - 2.37468(\Delta\hat{x}_1)\hat{x}_2 - 6.19913(\Delta\hat{x}_1)^2\hat{x}_2 \\ &\quad -4.10726\hat{x}_2^2 + 8.73440(\Delta\hat{x}_1)\hat{x}_2^2 + 6.29571\hat{x}_2^3 \end{aligned} \tag{B.31}$$

where $\hat{x}_\alpha = x_\alpha/h$. The fit quality is verified in Figure B.7. With a good fit of $g(\Delta x_1/h, x_2/h)$, K_I is found by choosing some offset x_2, choosing some distance (Δx_1) where the curvature (fringe density) is maximum, counting the number of fringes (Δm), and finally using equations (B.29) and (B.31).

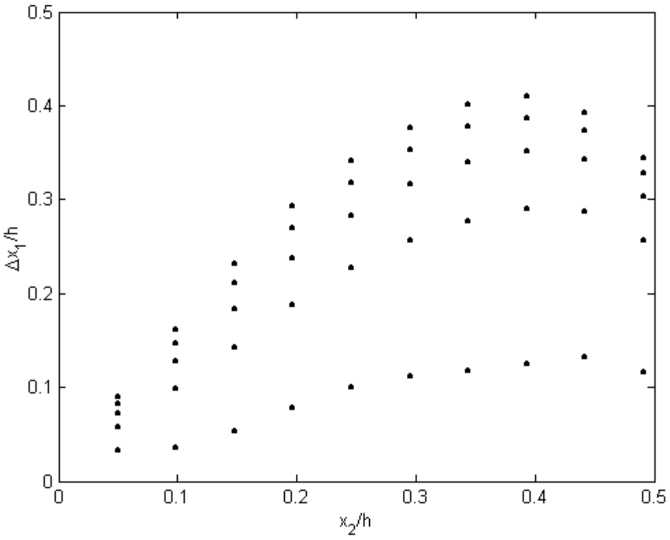

Figure B.6: Points for which $g(\Delta x_1/h, x_2/h)$ was calculated.

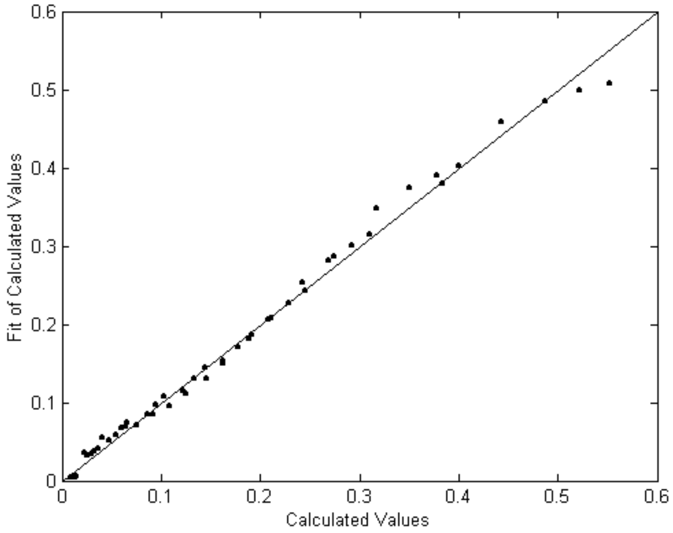

Figure B.7: Verification of fit equation for $g(\Delta x_1/h, x_2/h)$.

Bibliography

[1] J. D. Achenbach. Crack propagation generated by a horizontally polarized shear wave. *Journal of the Mechanics and Physics of Solids*, 18:245–259, 1970.

[2] J. D. Achenbach. Extension of a crack by a shear wave. *Zeitschrigt fur angewandte Mathematic und Physik*, 21:887–900, 1970.

[3] J. D. Achenbach. Dynamic effects in brittle fracture. In S. Nemat-Nasser, editor, *Mechanics Today*, chapter 1, pages 1–57. Pergamon, Elmsford, New York, 1974.

[4] American Society for Testing and Materials, West Conshohocken, PA 19428-2959. *Annual Book of ASTM Standards 2001 Sect. 3 Metals Test Methods and Analytic Procedures; Volume 03.01, Metals—Mechanical Testing; Elevated and Low Temperature Tests; Metallography.*

[5] T. L. Anderson. *Fracture Mechanics: Fundamentals and Applications.* Springer-Verlag, New York, New York, 1997.

[6] C. Atkinson and J. D. Eshelby. The flow of energy into the tip of a moving crack. *International Journal of Fracture*, 4:3–8, 1968.

[7] K. B. Broberg. The propagation of a brittle crack. *Archiv fur Fysik*, 18:159–192, 1960.

[8] L. S. Costin and J. Duffy. The effect of loading rate and temperature on the initiation of fracture in a mild, rate sensitive steel. *Journal of Engineering Materials and Technology*, 101:258–264, 1979.

[9] J. W. Dally. Dynamic photoelastic studies of fracture. *Experimental Mechanics*, 19:349–367, 1979.

[10] J. W. Dally and D. B. Barker. Dynamic measurement of initiation toughness at high loading rates. *Experimental Mechanics*, 28:298–303, 1988.

[11] J. W. Dally and J. R. Burger. The role of the electric resistance strain gage in fracture research. In Jonathan S. Epstein, editor, *Experimental Techniques in Fracture*, chapter 1, pages 1–39. VCH Publishers, Inc., 1993.

[12] J. W. Dally and W. F. Riley. *Experimental Stress Analysis.* McGraw Hill, Boston, Mass, 3rd edition, 1991.

[13] L. B. Freund. Crack propagation in an elastic solid subjected to general loading I. constant rate of extension. *Journal of the Mechanics and Physics of Solids*, 20:129–140, 1972.

[14] L. B. Freund. Crack propagation in an elastic solid subjected to general loading II. nonuniform rate of extension. *Journal of the Mechanics and Physics of Solids*, 20:141–152, 1972.

[15] L. B. Freund. Energy flux into the top of an extending crack in an elastic solid. *Journal of Elasticity*, 2:341–349, 1972.

[16] L. B. Freund. *Dynamic Fracture Mechanics.* Cambridge University Press, New York, New York 10011, 1998.

[17] L. B. Freund and Rosakis A. J. The structure of the near tip-field solution during transient elastodynamic crack growth. *Journal of the Mechanics and Physics of Solids*, 40:699–719, 1992.

[18] L. B. Freund and R. Clifton. On the uniqueness of plane elastodynamic solutions for running cracks. *Journal of Elasticity*, 4:293–299, 1974.

[19] L. B. Freund, J. Duffy, and A. J. Rosakis. Dynamic fracture initiation in metals and preliminary results on the method of caustics for crack propagation measurements. *ASME Paper No. 81-PVP-15*, 1981.

[20] J. W. Hutchinson. *Journal of the Mechanics and Physics of Solids*, 16(13):337, 1968.

[21] G. R. Irwin. Analysis of stresses and strains near the end of a crack traversing a plate. *Journal of Applied Mechanics*, 24:361–364, 1959.

[22] G. R. Irwin. Fracture mode transition for a crack traversing a plate. *Journal of Basic Engineering*, 82:417–425, 1960.

[23] G. R. Irwin. Crack extension force for a part-through crack in a plate. *Journal of Applied Mechanics*, 29:651–654, 1962.

[24] M. H. Jones and W. F. Brown Jr. The influence of crack length and thickness in plane straining fracture toughness testing. *ASTM STP 463*, pages 63–101, 1970.

[25] J. F. Kalthoff. Shadow optical methods of caustics. In A. S. Kobayashi, editor, *Handbook on Experimental Mechanics*, chapter 9, pages 430–498. McGraw Hill Publishers, New York, New York, 1987.

[26] M. F. Kanninen and C. H. Popelar. *Advanced Fracture Mechanics.* Oxford University Press, New York, New York, 1985.

[27] B. V. Kostrov and L. V. Nikitin. Some general problems of mechanics of brittle fracture. *Archiwum Mchaniki Stosowanej*, 22:749–775, 1970.

[28] S. Krishnaswamy, A. J. Rosakis, and G. Ravichandran. On the extent of dominance of asymptotic elastodynamic crack-tip fields: Part II — numerical investigation of three-dimensional and transient effects. *Journal of Applied Mechanics*, 58:95–103, 1991.

[29] C. Liu and A. J. Rosakis. On the higher order asymptotic analysis of a non-uniformly propagating crack along an arbitrary path. *Journal of Elasticity*, 35:27–60, 1994.

[30] H. Maigre and D. Rittel. Dynamic fracture detection using the force-displacement reciprocity: Application to the compact compression specimen. *International Journal of Fracture*, 73:67–79, 1995.

[31] T. Nakamura and D. M. Parks. Three-dimensional field near the crack front of a thin elastic plate. Presented at 24th Annual Meeting of the Society of Engineering Science, September 21-23, 1987, at Salt Lake City, Utah.

[32] T. Nakamura, C. F. Shih, and L. B. Freund. Elastic-plastic analysis of a dynamically loaded circumferentially notched round bar. *Engineering Fracture Mechanics*, 22:437–452, 1985.

[33] D. M. Owen, S. Zhuang, A. J. Rosakis, and G. Ravichandran. Experimental determination of dynamic crack initiation and propagation fracture toughness in thin film aluminum sheets. *International Journal of Fracture*, 90:153–174, 1998.

[34] R. D. Pfaff. *Three-Dimensional Effects in Nonlinear Fracture Explored with Interferometry.* PhD thesis, California Institute of Technology, Pasadena, California 90125, 1991. Pages 136-137.

[35] D. Post. *High Sensitivity Moire Experimental Analysis for Mechanics and Materials.* CRC Press, Boca Raton, Florida 33431, 2rd edition, 1995.

[36] S. Prabhu and J. Lambros. Effect of mode mixity on K-dominance and three-dimensionality in cracked plates. *International Journal of Fracture*, 104:51–69, 2000.

[37] K. Ravi-Chandar and W. G. Knauss. An experimental investigation into dynamic fracture: I. crack initiation and arrest. *International Journal of Fracture*, 25:247–262, 1984.

[38] J. R. Rice and G. F. Rosengren. *Journal of the Mechanics and Physics of Solids*, 16(1), 1968.

[39] D. Rittel and H. Maigre. An investigation of dynamic crack initiation in PMMA. *Mechanics of Materials*, 23:229–239, 1996.

[40] D. Rittel and H. Maigre. A study of mixed-mode dynamic crack initiation in PMMA. *Mechanics Research Communications*, 23:475–481, 1996.

[41] A. J. Rosakis. Two optical techniques sensitive to gradients of optical path difference: The method of caustics and the coherent gradient sensor (CGS). In Jonathan S. Epstein, editor, *Experimental Techniques in Fracture*, chapter 10, pages 327–425. VCH Publishers, Inc., 1993.

[42] A. J. Rosakis, J. Duffy, and L. B. Freund. The determination of the dynamic fracture toughness of AISI 4340 steel by the shadow spot method. *Journal of the Mechanics and Physics of Solids*, 34:443–460, 1984.

[43] A. J. Rosakis and K. Ravi-Chandar. On the crack tip stress state an experimental evaluation of three-dimensional effects. *International Journal of Solids and Structures*, 22(2):121–134, 1986.

[44] C. F. Shih. Relationships between the J-integral and the crack opening displacement for stationary and extending cracks. *Journal of the Mechanics and Physics of Solids*, 29(4):305–326, 1981.

[45] I. N. Sneddon. The distribution of stress in the neighbourhood of a crack in an elastic solid. *Proceedings, Royal Society of London*, A-187:229–260, 1946.

[46] S. Suresh, T. Nakamura, Y. Yeshurun, K. H. Yang, and J. Duffy. Tensile fracture-toughness of ceramic material—effects of dynamic loading and elevated-temperatures. *Journal of the American Ceramic Society*, 73:2457–2466, 1990.

[47] P. S. Theocaris. Elastic stress intensity factors evaluated by caustics. In G. C. Shih, editor, *Mechanics of Fracture*, volume VII. Sijthoff and Noordhoff, Roc Alphen aan den Rijn, The Netherlands, 1981.

[48] H. V. Tippur, S. Krishnaswamy, and A. J. Rosakis. A coherent gradient sensor for crack tip deformation measurements: Analysis and experimental results. *International Journal of Fracture*, 48(1):193–204, 1990.

[49] H. V. Tippur, S. Krishnaswamy, and A. J. Rosakis. Optical mapping of crack tip deformations using the methods of transmission and reflection coherent gradient sensing: A study of crack tip K-dominance. *International Journal of Fracture*, 52:91–117, 1991.

[50] H. M. Westergaard. On the stress distribution at the base of a stationary crack. *Journal of Applied Mechanics*, 24:109–114, 1959.

[51] M. L. Williams. Bearing pressures and cracks. *Journal of Applied Mechanics*, 6:49–53, 1939.

[52] J. R. Willis. Equations of motion for propagating cracks. The mechanics and physics of fracture. *The Metals Society*, 0:57–67, 1975.

[53] M. L. Wilson, R. H. Hawley, and J. Duffy. The effect of loading rate and temperature on fracture initiation in 1020 hot-rolled steel. *Engineering Fracture Mechanics*, 13:371–385, 1980.

[54] E. H. Yoffe. The moving griffith crack. *Philosophical Magazine*, 42:739–750, 1951.

[55] A. T. Zehnder and A. J. Rosakis. Dynamic fracture initiation and propagation in 4340 steel under impact loading. *International Journal of Fracture*, 43:271–285, 1990.